THREE-DIMENSIONAL TOPOLOGY OF SOLAR CORONAL MAGNETIC FIELDS

Daniel Stephen Brown

A Thesis Submitted for the Degree of PhD
at the
University of St Andrews

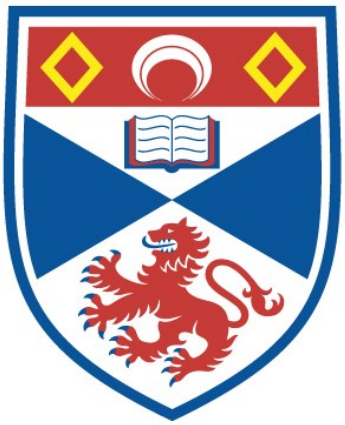

1999

Three-Dimensional Topology of Solar Coronal Magnetic Fields

Daniel Stephen Brown

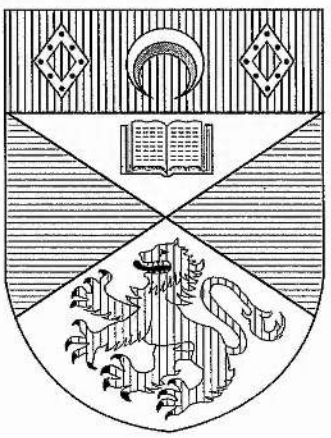

Thesis submitted for the degree of Doctor of Philosophy
of the University of St Andrews

December 7, 1999

Abstract

This thesis investigates the topology of the magnetic field in the solar corona. It is important have an understanding of how the highly complex coronal magnetic field behaves in order to study many fundamental coronal phenomena, such as coronal heating events, solar flares and polar plumes. The magnetic fields due to three or four discrete sources are investigated and the corresponding topological states are found. The locations of these states in parameter space is calculated and the bifurcations between states are analysed. A complete analysis has been undertaken for the three-source case and a selective one for the four-source case in order to identify new non-generic behaviour. The thesis goes on to study the topological behaviour of a coronal bright point. Different phases during the lifetime of the bright point are identified and the responsible topological behaviour due to the movement of the magnetic fragments in the photosphere is discussed.

Declaration

1. I, Daniel Stephen Brown, hereby certify that this thesis, which is approximately 25,000 words in length, has been written by me, that it is a record of work carried out by me and that it has not been submitted in any previous application for a higher degree.

   date 7/12/99 ..... signature of candidate

2. I was admitted as a research student in October 1996 and as a candidate for the degree of PhD in October 1997; the higher study for which this is a record was carried out in the University of St Andrews between 1996 and 1999.

   date 7/12/99 ..... signature of candidate

3. I hereby certify that the candidate has fulfilled the conditions of the Resolution and Regulations appropriate to the degree of PhD in the University of St Andrews and that the candidate is qualified to submit the thesis in application for that degree.

   date 7-12-99 ..... signature of supervisor ...

4. In submitting this thesis to the University of St Andrews I understand that I am giving permission for it to be made available for use in accordance with the regulations of the University Library for the time being in force, subject to any copyright vested in the work not being affected thereby. I also understand that the title and abstract will be published and that a copy of the work may be made and supplied to any bona fide library or research worker.

   date 7/12/99 ..... signature of candidat

Acknowledgements

I would primarily like to thank my mother, Susan Brown, who has encouraged me from an early age to explore my surroundings and to take an interest in everything. Without her I surely would not have achieved what I have.

There are many people who provided extremely useful assistance and discussion during my three years as a research student at St Andrews. Particular thanks must go to Eric Priest for his constant support and supervision without which this thesis would not be possible.

Thanks also go to Clare Parnell, Robert Walsh, Craig Deforest, Ed DeLuca, Leon Golub and Rebecca McMullen with whom I am collaborating on various projects and to the TRACE and SOHO/MDI teams for the observation sequences used in this thesis.

I must also acknowledge the invaluable support family and friends, whos inexhaustible supply of inspiration, patience and tea has kept me going when things have been tough.

I would finally like to thank the Engineering and Physical Science Research Council for financial support and the Smithsonian Astrophysical Observatory's Center for Astrophysics for travel support to visit the USA on a research trip.

Contents

Chapter 1

Introduction

The solar corona is a complex tangle of hot plasma structures which are dominated by the strong magnetic field in the Sun's atmosphere.

The coronal magnetic field comes from an intricate carpet of magnetic flux fragments which lie in the photosphere. These magnetic fragments are constantly moving, emerging, coalescing and deforming which causes the magnetic field to continually evolve.

It is extremely difficult to study the behaviour of the magnetic field globally, although global solar models have been attempted (Browning et al., 1998), so it is useful to break the large-scale field down into smaller regions and study the local topology of each region.

This thesis will study such a localised magnetic topology in order to understand the how the field can behave and change its structure.

1.1 Structure of the Solar Atmosphere

The Sun's atmosphere has traditionally been regarded as being made up of four levels, the photosphere, the chromosphere, the transition region and the corona (Priest, 1982). The photosphere is the surface layer of the Sun and has a thickness of the

order of 500 km and a temperature of about 6,000 K. The magnetic field in the solar atmosphere is rooted to flux concentrations in the photosphere (Schrijver et al., 1997). The distribution of such flux concentrations can be measured by instruments like the *Michelson-Doppler Imager* (MDI) on the *SOlar and Heliospheric Observatory* (SOHO).

The chromosphere and transition region are the next two layers and are around 2 Mm and 500 km thick, respectively. In the upper chromosphere and transition region the temperature rises rapidly to around 500,000 K (Wentzel, 1989).

The corona makes up the rest of the atmosphere and extends out to the Earth and beyond. The plasma in the lower corona can reach temperatures of millions of Kelvin. The magnetic field is dominant in the corona and is, in general, much more influential on the behaviour of the plasma normal to the field than either pressure or gravity.

The corona can be observed by instruments that image the Sun in wavelengths like *extreme ultraviolet light* (such as EIT on SOHO, or TRACE) and *X-rays* (such as Yohkoh). Different wavelength bands correspond to different temperature ranges.

The size of coronal loop structures in the corona can range from small-scale bright points which have a height of about 15 Mm to large-scale loops which can have heights of over 300 Mm (Smith, 1997). These scales are far larger than 2.5 Mm of the chromosphere and transition region and so in this thesis these regions will be thought of as a very thin surface layer that is treated as the lower boundary of the corona.

1.2 Magnetic Fields

1.2.1 Magneto-hydrostatics

The magnetic field in the solar corona is described by the magneto-hydrodynamic (MHD) equations (see appendix C). The particular equations that are used in this thesis are:

The equation of motion,

$$\rho\left(\frac{\partial \mathbf{v}}{\partial t} + (\mathbf{v}.\nabla)\,\mathbf{v}\right) = \mathbf{j} \times \mathbf{B} - \nabla p - \rho\nabla\psi \tag{1.1}$$

Ampère's law

$$\nabla \times \mathbf{B} = \mu_0 \mathbf{j} \tag{1.2}$$

and finally

$$\nabla.\mathbf{B} = 0 \tag{1.3}$$

Now suppose the plasma is in equilibrium, so that $\mathbf{v} = 0$ and $\frac{\partial}{\partial t} = 0$. Equation 1.1 becomes

$$\mathbf{j} \times \mathbf{B} - \nabla p - \rho\nabla\psi = \mathbf{0} \tag{1.4}$$

Equation 1.4 is the magneto-hydrostatic (MHS) equation (Priest, 1982).

It is this equation that is used together with equations 1.2 and 1.3 to calculate the magnetic fields studied in this thesis. So the assumption is made that the sources of the magnetic field in the photosphere are moving slowly enough that the system can relax to an equilibrium state. To be more specific, the magnetic field has time to relax if the plasma velocity is a lot smaller than the speed with which information is transmitted along field lines (the Alfvén speed).

1.2.2 Potential fields

Potential modelling makes the further assumptions that the current density vanishes everywhere. This makes $j = 0$ and so equation 1.2 becomes

$$\nabla \times \mathbf{B} = 0. \tag{1.5}$$

Taking the curl of this and coupling with equation 1.3 gives

$$\nabla^2\mathbf{B} = 0, \tag{1.6}$$

and so the magnetic field is potential. This means that there is a scalar function Φ, called the *scalar magnetic potential* defined by

$$\mathbf{B} = \nabla\Phi, \tag{1.7}$$

which satisfies Laplace's equation,

$$\nabla^2\Phi = 0. \tag{1.8}$$

Such a simple form for the field, along with the wealth of known potential theory, makes this a valuable tool for studying magnetic topology.

1.2.3 Force-free fields

The assumptions for potential fields will often not hold in the corona, particularly in active regions and coronal streamers (Priest, 1982).

A good alternative to potential fields are force-free fields. If the height of the region of interest is much less than the scale-height (the vertical distance in which the pressure falls by a factor e) and the ratio

$$\beta = \frac{2\mu_0 p_0}{B_0^2} \tag{1.9}$$

of the plasma, where p_0 and B_0 are the base pressure and magnetic field, is much less than unity then the magnetic field dominates and equation 1.4 becomes

$$\mathbf{j} \times \mathbf{B} = \mathbf{0}. \tag{1.10}$$

So the electric current flows along magnetic field lines. Force-free fields are then described by solutions to the equation

$$\nabla \times \mathbf{B} = \alpha\mathbf{B}, \tag{1.11}$$

subject to boundary conditions on the $z = 0$ plane (the photosphere) and where α is a function of position which is constant along field lines (see appendix A).

There are many ways to treat this problem both numerically and analytically. Such methods are described in texts such as Chiu and Hilton (1977); Lothian and Browning (1995); Amari et al. (1997); Gary (1989); Sakurai (1989).

The simplest family of functions to consider has $\alpha = constant$. For this case analytical solutions can be derived for which a topological analysis can be performed. The case where $\alpha = 0$ refers to the potential case which is discussed in chapters 2,3.

The solution for this analytical case is

$$\mathbf{B}(x,y,z) = \frac{1}{2\pi}\int_{-\infty}^{\infty}\int_{-\infty}^{\infty}\mathbf{G}(x,y,z,x',y')\mathbf{B}_z(x',y',0)dx'dy', \tag{1.12}$$

with

$$G_x = \frac{x-x'}{R}\frac{\partial\Gamma}{\partial z} + \alpha\Gamma\frac{y-y'}{R}, \tag{1.13}$$

$$G_y = \frac{y-y'}{R}\frac{\partial\Gamma}{\partial z} - \alpha\Gamma\frac{x-x'}{R}, \tag{1.14}$$

$$G_z = -\frac{\partial\Gamma}{\partial R} - \frac{\Gamma}{R}, \tag{1.15}$$

and

$$\Gamma = \frac{z\cos(\alpha\rho)}{R\rho} - \frac{\cos(\alpha z)}{R} \tag{1.16}$$

where $R^2 = x^2 + y^2$ and $\rho^2 = R^2 + z^2$, and the boundary conditions are given by $B_z(x',y',0)$. The derivation of these equations is given in appendix A.

There is a threshold, for this method, above which reasonable solutions no longer occur, given by the relation

$$|\alpha| = \frac{2\pi}{L}, \tag{1.17}$$

where L is the characteristic length-scale of the boundary conditions in the photosphere (Gary, 1989). What this also means is that as the magnitude of α increases, the large-scale magnetic features become more unrealistic, and the region containing 'physical' solutions becomes smaller in proportion to $1/\alpha$.

For the potential solutions, when $\alpha = 0$, the critical length-scale is infinite and the solution (in equations 1.12-1.16) reduces down to a potential one.

In this thesis, length-scales are typically of the order $L = 2$, that is to say that the maximum foot-point separation or magnetogram length is typically about 2 units. This is due to the boundary conditions being applied in a box where $-1 \leq x, y \leq 1$ in dimensionless units. This means that the local topology can be studied when α varies between approximately $\pm\pi$.

1.3 Bifurcation Theory

This section will give a introduction to some basic bifurcation behaviour. More detailed information about bifurcation theory can be found in texts such as Ruelle (1989); Thompson and Stewart (1986); Glendinning (1994); Guckenheimer and Holmes (1986).

Consider a system depending on a parameter λ that satisfies the equation

$$\dot{x} = f(x, \lambda). \tag{1.18}$$

The nature of the solution will normally change smoothly as λ is varied. However, there can be critical values of λ where the change is more significant. These values are called bifurcation points.

Bifurcation types can be put into one of two categories: local bifurcation, where there are changes in the null solutions; and global bifurcation, where there are changes in the dynamics of the system. Note that, this thesis deals with static fields, so equation 1.18 refers to differentiation with respect to a quantity other than time, normally field line arc-length. Dynamics, in this sense, then refers to field line behaviour and connectivity.

1.3.1 Local bifurcation

A null-solution to equation 1.18 satisfies $f(x_n, \lambda) = 0$. In general, this has a solution $x_n(\lambda)$, but, this can break down if $\frac{\partial f}{\partial x}$ is not invertible. If this occurs at a point λ^* then λ^* is a bifurcation point.

If the system is linearised about the null, then $\dot{x} = Ax$, where $A = \frac{\partial f}{\partial x}(x_n, \lambda)$. Thus, λ^* is a bifurcation point if A is not invertible, and this happens when A has a zero eigenvalue. The eigenvalues determine the stability of the null-solution. If the real part of the eigenvalue is negative then x_n is stable; if it is positive then x_n is unstable. Therefore, local bifurcations are points where the stability of the null-solution changes.

Some different types of local bifurcations are:

Turning-Point Bifurcation

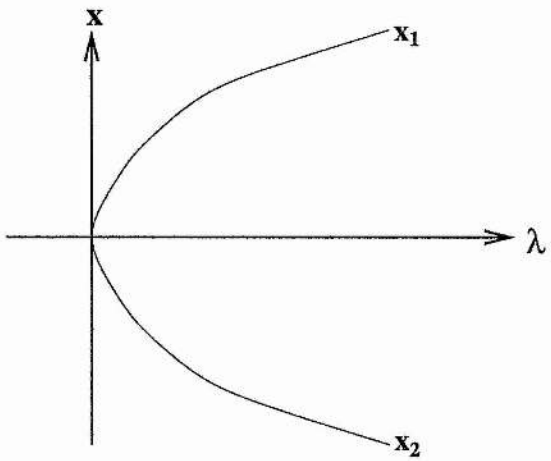

Figure 1.1: Bifurcation diagram for the turning-point bifurcation. The curve shows the null-solutions as a function of λ.

Consider, for example, the system

$$\dot{x} = \lambda - x^2. \tag{1.19}$$

This has a null point when $\lambda - x^2 = 0$ (i.e., $x_n = \pm\sqrt{\lambda}$) when $\lambda \geq 0$, and it has no solutions when $\lambda < 0$. Therefore, there are two null solution paths when $\lambda > 0$, namely, $x_1 = \sqrt{\lambda}$ and $x_2 = -\sqrt{\lambda}$ (figure 1.1).

The x_1-solution has an eigenvalue of $-2\sqrt{\lambda}$, so it is stable, whereas, the x_2-solution has an eigenvalue of $2\sqrt{\lambda}$, which makes it unstable. When $\lambda = 0$ the eigenvalue is zero and so this is the bifurcation point.

Transcritical Bifurcation

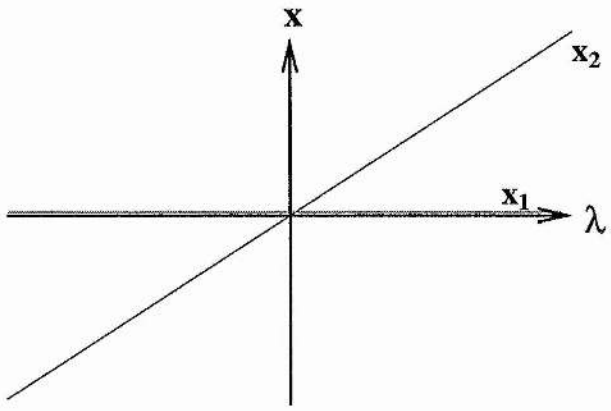

Figure 1.2: Bifurcation diagram for the transcritical bifurcation. The curve shows the null-solutions as a function of λ. Note that $x = 0$ is a solution.

Consider the system

$$\dot{x} = x(\lambda - x), \tag{1.20}$$

which has a null point when $x(\lambda - x) = 0$, i.e., when $x_1 = 0$ or $x_2 = \lambda$ (figure 1.2).

The x_1 solution has an eigenvalue of λ, so it is stable when $\lambda < 0$ and unstable when $\lambda > 0$. The x_2 solution has an eigenvalue of $-\lambda$, which makes it unstable when $\lambda < 0$ and stable when $\lambda > 0$. There is a change of stability when $\lambda = 0$ and so the eigenvalues of x_1 and x_2 are zero. This is the bifurcation point.

Pitchfork Bifurcation

Consider the system

$$\dot{x} = x(\lambda - x^2), \tag{1.21}$$

which has a null point when $x(\lambda - x^2) = 0$, i.e., when $x_1 = 0$ or, if $\lambda > 0$ when $x_2 = \sqrt{\lambda}$ or $x_3 = -\sqrt{\lambda}$ (figure 1.3).

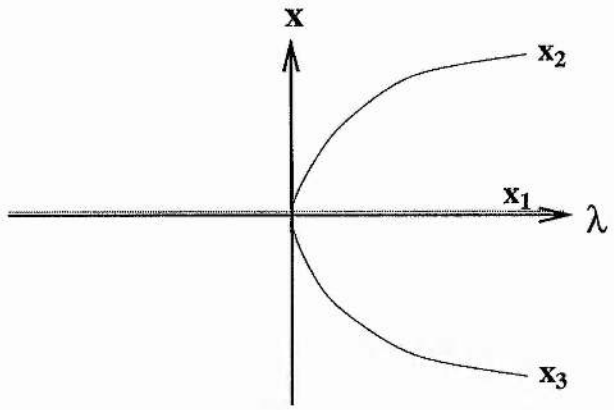

Figure 1.3: Bifurcation diagram for the pitchfork bifurcation. The curves show the null-solutions as a function of λ. Note that $x = 0$ is a solution.

The x_1 solution has an eigenvalue of λ, so it is stable when $\lambda < 0$ and unstable when $\lambda > 0$. The x_2 and x_3 solutions both have eigenvalues of -2λ, which make them stable as they only exist for $\lambda > 0$. There is a change of stability when $\lambda = 0$. The eigenvalue of the null-solution here is zero and so this is the bifurcation point.

Hopf Bifurcation

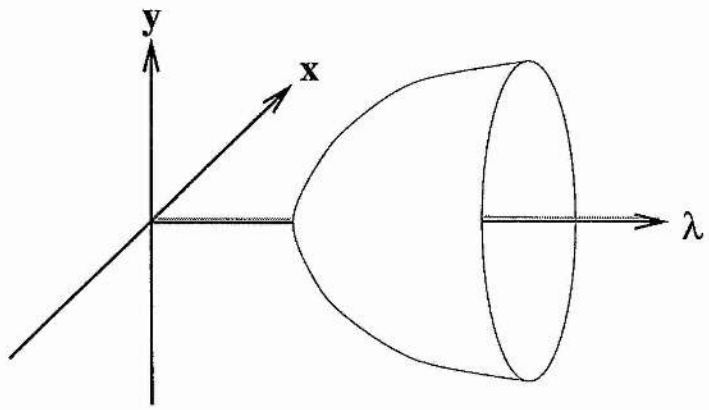

Figure 1.4: Bifurcation diagram for the Hopf bifurcation. The curves shows the null-solutions and the surface shows the periodic orbits as functions of λ. Note that $x = y = 0$ is a solution.

Consider the two-dimensional system

$$\dot{r} = r(\lambda - r^2), \tag{1.22}$$

$$\dot{\theta} = 1. \tag{1.23}$$

So $\theta = t$ and equation 1.22 has zeros when $r = 0$ and $r = \sqrt{\lambda}$ if $\lambda > 0$. From the pitchfork bifurcation, $r = 0$ is stable when $\lambda < 0$, but unstable when $\lambda > 0$, and $r = \sqrt{\lambda}$ is stable when $\lambda > 0$.

Writing this system in Cartesian co-ordinates gives

$$\begin{pmatrix} \dot{x} \\ \dot{y} \end{pmatrix} = \begin{pmatrix} \lambda & -1 \\ 1 & \lambda \end{pmatrix} \begin{pmatrix} x \\ y \end{pmatrix} - \begin{pmatrix} x(x^2+y^2) \\ y(x^2+y^2) \end{pmatrix}. \tag{1.24}$$

So $(0,0)$ is a null point with eigenvalues of $\lambda \pm i$, which is stable when $\lambda < 0$, but unstable when $\lambda > 0$.

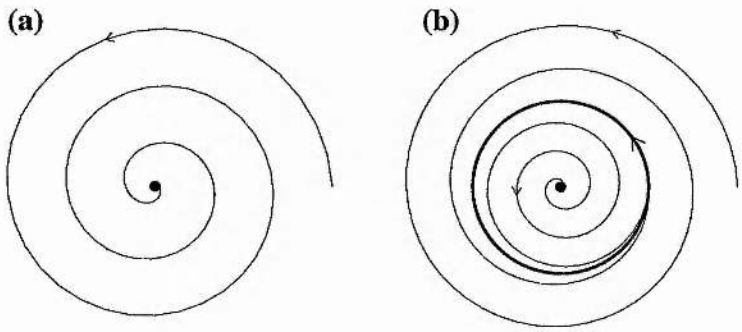

Figure 1.5: The behaviour of streamlines (a) spiraling into the null before Hopf bifurcation and (b) approaching the periodic orbit after bifurcation.

Before bifurcation, when $\lambda < 0$, the $(0,0)$ solution is stable and streamlines spiral towards it. At bifurcation, when $\lambda = 0$, the real part of the eigenvalues becomes zero. As λ increases, an attractive periodic orbit is created and the $(0,0)$ solution becomes unstable. This is shown in figure 1.5.

1.3.2 Global bifurcation

Local bifurcations deal with the local properties of null points and periodic orbits, that is to say, the dynamical behaviour can be deduced from local behaviour. Bifurcations are not always governed by these localised aspects, since there are situations which involve global behaviour of streamlines.

The global behaviour cannot be detected through local changes, such as the change in stability of a null point, but is found by analysing streamline connectivity.

Some different types of global bifurcation are;

Heteroclinic Bifurcation

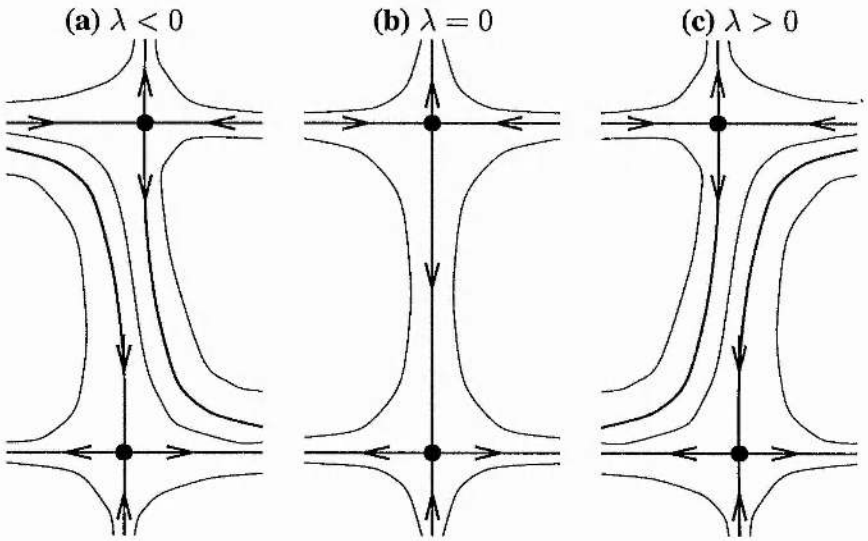

Figure 1.6: Streamline diagrams for heteroclinic bifurcation (a) before, (b) during, and (c) after bifurcation. The bold curves show the connectivity of streamlines emanating from the null points.

Consider the system governed by the equations

$$\dot{x} = \lambda + x^2 - xy, \tag{1.25}$$

$$\dot{y} = y^2 - x^2 - 1. \tag{1.26}$$

When $\lambda = 0$ (figure 1.6b) the system has null points at $(0, 1)$ and $(0, -1)$. These two nulls are saddle-points and are joined by what is known as a heteroclinic connection.

This is structurally unstable and when λ is perturbed the heteroclinic connection is broken and the two nulls are no longer joined. When $\lambda < 0$ there are streamlines that travel from $x = -\infty$ to $x = +\infty$ (see figure 1.6a). When $\lambda > 0$ the reverse is true and some streamlines travel from $x = +\infty$ to $x = -\infty$. The nature of the connectivity of the streamlines clearly changes as λ changes sign. Thus, $\lambda = 0$ is a bifurcation point.

Homoclinic Bifurcation

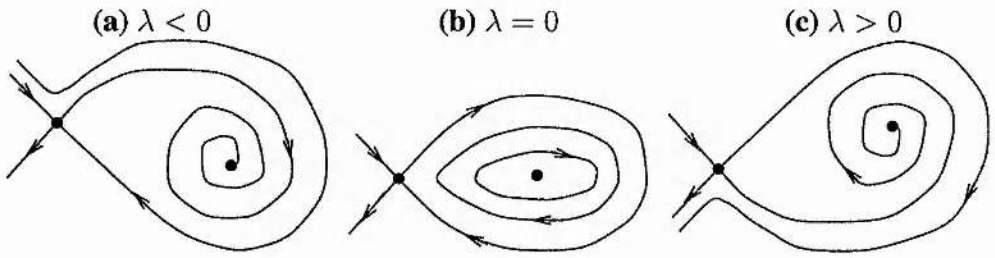

Figure 1.7: Streamline diagrams for homoclinic bifurcation (a) before, (b) during, and (c) after bifurcation. The bold curves show the connectivity of streamlines emanating from the null points, or periodic orbits in case (b).

Consider the system governed by the equations

$$\dot{x} = y, \tag{1.27}$$

$$\dot{y} = x - x^2 + \lambda y. \tag{1.28}$$

This has null points at $(0, 0)$ and $(1, 0)$. The null at $(0, 0)$ is a saddle-point and the null at $(1, 0)$ is a sink when $\lambda < 0$ (figure 1.7a), a centre when $\lambda = 0$ (figure 1.7b), and a

source when $\lambda > 0$ (figure 1.7c).

The centre when $\lambda = 0$ is unstable and perturbations of λ cause the centre to become either a source or a sink. The change of connectivity of the streamlines when λ changes sign indicates that $\lambda = 0$ is a bifurcation point.

1.3.3 Summary of bifurcations

There is a wealth of bifurcation behaviour which has only been touched upon here. The bifurcations illustrated in this section give a flavour of the basic bifurcations which will evolve into more complex three-dimensional bifurcations in chapters 2,3. The local and global bifurcation subgroups will still apply to this new bifurcation behaviour.

1.4 Outline of Thesis

This object of this thesis is to explore the topological behaviour of magnetic fields, specifically those that can arise in the solar atmosphere. Section 1.2 has discussed how the magnetic field can be modelled using the MHD equations (section 1.2.1) as a starting point. It discusses the assumptions that are made for potential fields (section 1.2.2) and force-free fields (section 1.2.3) with special reference to the constant-α force-free approximation. It is these field models that will be used in this thesis to explore the topological behaviour of coronal magnetic fields.

Section 1.3 discusses some basic bifurcation behaviour. This has been divided into two categories: local bifurcation (section 1.3.1), where changes in the behaviour of the system can be analysed in terms of local events such as the creation or annihilation of null points; and global bifurcation (section 1.3.2), where the changes of behaviour of the system results in changes in connectivity of streamlines without a significant change in local behaviour.

These bifurcations are the foundation for the complex bifurcation behaviour in three-

dimensional fields. When there is a topological change of the field, the system will have bifurcated between two topological states. So, as the topological behaviour of magnetic fields is explored, the bifurcations exhibited by the fields must be deduced.

Chapter 2 analyses the topological behaviour of a potential field due to three discrete sources. All of the stable topological states that are exhibited by this system are presented and their location in parameter space is discussed (there are four parameters that can be varied). From this the bifurcation behaviour can be explored, and four types of bifurcation (which are related to the cases in section 1.3) are deduced.

Chapter 3 then proceeds to explore the topological behaviour exhibited by potential fields due to four discrete sources. It concentrates on specific behaviour which involves magnetic separators (these are field lines which connect two nulls). Much of the behaviour involves compositions of the basic three-source building blocks, and the bifurcations deduced in chapter 2 are preserved in this higher-order case. There are new features to be discussed, however. Topological states which possess two separators can bifurcate in a new way, where the two separators approach one another and coalesce. Another feature specific to the four-source (and higher) case is that a null point can leave the $z = 0$ plane (to which it is normally confined) and rise up into the corona.

Chapter 4 relates the topological analysis to solar phenomena using a coronal bright point as a case study. Using sequences of observations taken by the TRACE and SOHO satellites, the properties of this bright point are discussed and its evolution is described. Temperature and emission measure diagnostics can be calculated and the variation of these quantities can be tied in to the different phases of the event.

The topology of the bright point has been calculated using the constant-α force-free method discussed in section 1.2.3. Topological changes and bifurcations relating to the different phases of the bright point are discussed. It must be noted that the variation of α will add another layer of complexity to the topological analysis and new topological behaviour which has not been discussed in chapters 2 and 3 may arise. However, much of the potential behaviour will carry through to the force-free case and the topology

can be analysed with reference to the potential case. This is in contradiction to Hudson and Wheatland (1999) who suggest that potential and force-free models using the same boundary conditions are not even qualitatively similar. However, they chose to use a highly symmetric case for their analysis, which is topologically unstable. This means that by varying α in their analysis the symmetry is broken and the topology, unsurprisingly, changes. They would also have found significantly different topological behaviour if they had broken the symmetry by perturbing the source positions or strengths, but keeping the field potential.

Chapter 2

Three-Source Topology

2.1 Introduction

Most of the dynamical processes which take place in the Sun's corona (its outer atmosphere) are dominated by the magnetic field. The sources of the coronal field are magnetic fragments scattered over the solar surface and mostly clustered around the edges of large convection cells called supergranules. These sources are not static but continually move about over the surface, coalescing, fragmenting and cancelling with one another. The resulting coronal magnetic field has an incredibly complex topology. In order to begin to understand this complexity it is important to consider, as building blocks, the field generated by a small number of discrete sources.

Priest et al. (1997) started this task by studying some of the different topological states of a three-source system together with some of the types of bifurcation between states. They considered the case where the sources are collinear and the special non-collinear case with a positive source at the origin and two negative sources of equal strength equidistant from the positive source.

This chapter extends their analysis by considering a general unbalanced three-source system and classifying the eight stable topological states that arise and their location in parameter space (Brown and Priest, 1998): six of the states occur when two of the

sources have polarity opposite to the third and the remaining two states occur when all three sources have the same polarity. In addition, the bifurcations from one topological state to another, both local and global, are analysed (Brown and Priest, 1999b).

Particular study is made of a *local separator bifurcation* (in which two linear nulls and a separator linking them are created or destroyed), a *global spine bifurcation* (at which the spine of one null lies in the field of the other) and a *global separator bifurcation* (at which a topologically stable separator is created or destroyed).

In this chapter, examination of the different topological states that are possible in a magnetic configuration due to three sources is made. The chapter then proceeds to discuss how the system bifurcates between these topological states. Section 2.2 describes what constitutes a topological skeleton. Section 2.3 formulates the model and shows that eight different states are possible. Section 2.4 examines the bifurcations from one state to another when there is one strong positive and two weak negative sources, while section 2.5 deals with the case when the negative sources are together stronger than the positive source. Section 2.6 focuses on the state when all three sources have the same polarity. Section 2.7 describes the unique behaviour when the sources are co-linear, while section 2.8 discusses the general case where no two sources have the same strength.

2.2 The Topological Skeleton

The *topological skeleton* of a magnetic field $\mathbf{B}(\mathbf{r})$ is defined by the configuration of the sources, the set of null points and a network of spine field lines and separatrix surfaces (Priest et al, 1997). The null points of the system satisfy the equation

$$\mathbf{B}(\mathbf{r}) = \mathbf{0}, \tag{2.1}$$

and in the generic case the linearized field near the null possesses three distinct eigenvalues which sum to zero in view of the equation $\nabla.\mathbf{B} = 0$ (Fukao et al, 1975; Greene

1988). Field lines are given by the equation

$$\frac{\mathbf{dr}}{ds} = \frac{\mathbf{B(r)}}{|\mathbf{B(r)}|}. \tag{2.2}$$

Field line plots in this text are obtained by numerical integration of the equation (Rheinboldt, 1986; Keller, 1976).

Priest and Titov (1996) have classified the nature of the different kinds of null and proposed the terms spine and fan (see also Cowley, 1973; Lau and Finn, 1990; Parnell et al., 1996). When two eigenvalues are positive, the plane of the corresponding eigenvectors consists of a separatrix surface of field lines radiating out from the null, known as a 'fan surface'. The eigenvector of the negative eigenvalue is an isolated field line, known as the 'spine field line', which approaches the null. When two eigenvalues are negative and one positive, then the fan field lines in the separatrix surface converge into the null and the spine field line is directed away from it (figure 2.1). Magnetic flux surfaces which touch a boundary may also form separatrices (Hide, 1979; Titov et al., 1993).

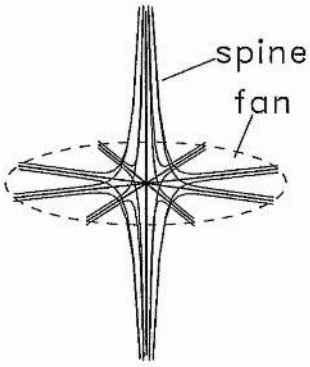

Figure 2.1: The structure of the field lines near a linear proper radial null.

The separatrix surfaces divide the space into several distinct regions, in each of which all the field lines have the same limit sets, i.e., sources and sinks. The states may be topologically stable or unstable. Topologically unstable states occur at critical values of a parameter between two stable states (Moffatt, 1985; Berger, 1989; Hornig and Schindler, 1996).

2.3 Formulation of the Model

2.3.1 Equations

Consider the potential coronal magnetic field produced by a series of flux sources on the solar surface (photosphere), which is treated locally as a plane. The coronal magnetic field depends on the positions and strengths of the sources. Take the photosphere to be the plane where $z = 0$, and the corona to be the region $z > 0$. Without loss of generality, the first source can be placed at the origin and given a source strength of 1. The next source can be placed a distance 1 along the x-axis, in the $z = 0$ plane, and the position of the third is scaled relative to the first two. The second and third source strengths are scaled relative to that of the first source, as demonstrated in figure 2.2.

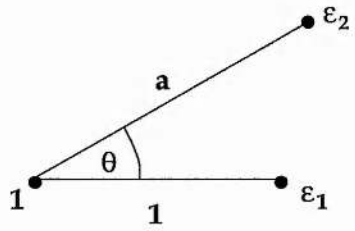

Figure 2.2: Illustration showing how the three sources of strengths 1, ϵ_1, ϵ_2 are configured parametrically.

As the magnetic field due to each source obeys an inverse square law, the rescaled field is given by

$$\mathbf{B}(\mathbf{r}) = \frac{\mathbf{r}}{|\mathbf{r}|^3} + \epsilon_1 \frac{\mathbf{r} - \hat{\mathbf{x}}}{|\mathbf{r} - \hat{\mathbf{x}}|^3} + \epsilon_2 \frac{\mathbf{r} - a\mathbf{r}_2}{|\mathbf{r} - a\mathbf{r}_2|^3}, \tag{2.3}$$

where $\mathbf{r} = x\hat{\mathbf{x}} + y\hat{\mathbf{y}} + z\hat{\mathbf{z}}$ and $\mathbf{r}_2 = \hat{\mathbf{x}}\cos\theta + \hat{\mathbf{y}}\sin\theta$.

For this model, $\nabla.\mathbf{B} = 0$ holds except at the three sources themselves. However, for a solar model only the photosphere and the corona are considered, i.e., where $z \geq 0$. As the sources lie in the $z = 0$ plane they are not true monopoles but representations of points where flux passes through the $z = 0$ plane. In this sense, $\nabla.\mathbf{B} = 0$ can be said to be preserved.

Since there are only three null points which are confined to the $z = 0$ plane the topological structure can be described in terms of the magnetic field configuration in the $z = 0$ plane.

2.3.2 Topological States

It transpires that the three-source system has eight distinct stable topological states associated with it. Two of these refer to the case where all sources have the same polarity, while the other six refer to the case where one source (say the source at the origin) has polarity opposite to the other two.

The six states with mixed polarity can be further subdivided into two groups of three states, namely when the source at the origin is stronger than the sum of the other two, and when it is weaker. The fan and spine field line configurations in the plane $z = 0$ of these six states are shown in figure 2.3. The two states when all sources have the same polarity are shown in figure 2.4.

In general, the separatrix surfaces of these topologies form either a separatrix dome (a closed surface) or a separatrix wall (an open surface extending to infinity). The topological states then vary according to how the domes or walls are configured. The structures of the eight topological states are as follows:

(i) Separate State, $-1 < \epsilon_1 + \epsilon_2 < 0$

When the two negative sources have a large enough angular separation and the central source is strong enough, then the separatrices form two separate domes which meet only at the origin.

(ii) Touching State, $-1 < \epsilon_1 + \epsilon_2 < 0$

When the angular separation of the two sources is neither too large nor too small and a is close to 1, then there is an intermediate state that is related to the enclosed and separate states. The two domes touch at a shared surface which contains two new null points and whose upper boundary is a spine curve that arches from the origin to one of

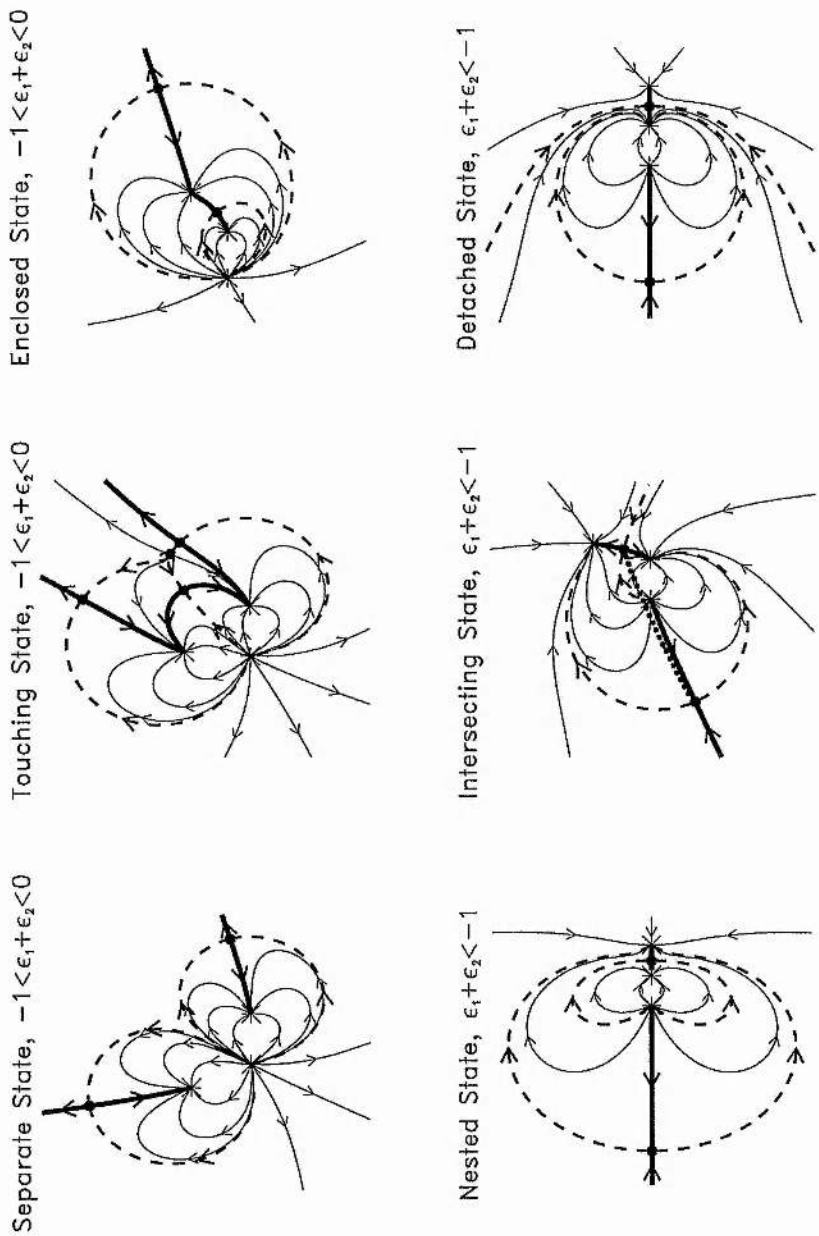

Figure 2.3: Skeletons of the topological states for a three-source system with strengths 1, $\epsilon_1 < 0$ and $\epsilon_2 < 0$ in the plane $z = 0$. The stars represent sources, the dots are null points where the field vanishes, the thick curves are spine field lines, the dashed lines are fan field lines (representing the intersection of a separatrix surface with the plane $z = 0$) and the thin lines are general field lines within each topological region.

the new null points.

(iii) Enclosed State, $-1 < \epsilon_1 + \epsilon_2 < 0$

When the angular separation of the two sources is small enough, the separatrices form two domes, one enclosed inside the other. The two domes touch at the origin source which provides the field lines for both domes.

(iv) Nested State, $\epsilon_1 + \epsilon_2 < -1$

In this state the source at the origin provides all the flux for one of the sinks and provides some of the flux for the other sink, the rest coming from infinity. It has two separatrix domes, one of which is contained inside the other, except that this time the domes do not meet at the source at the origin, but are completely detached from one another.

(v) Intersecting State, $\epsilon_1 + \epsilon_2 < -1$

The source at the origin provides part of the flux for both sinks, the remainder coming from infinity. There is only one dome in this state, the field lines for which are provided by two sources rather than one. The dome is intersected by a separatrix wall, which separates the field lines that go to the two sinks. The dome separates field lines which come to a sink from the source at the origin and field lines which come from infinity.

(vi) Detached State, $\epsilon_1 + \epsilon_2 < -1$

Now all the flux from the source at the origin goes to one sink which is also supplied with flux from infinity, while the other sink is completely supplied from infinity. A separatrix wall divides the volume into two regions, one of which contains one sink, the other contains the other sink and the source. In the latter region the field lines from the source to the sink are bounded by a separatrix dome.

(vii) Divided State, $\epsilon_1, \epsilon_2 > 0$

Here two unconnected separatrix walls divide the space into three separate regions, each containing a source of field lines which spread to infinity. Both walls are composed of field lines which fan out from a null point to infinity.

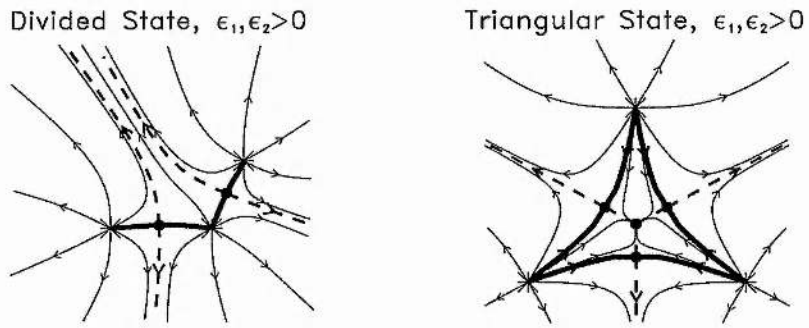

Figure 2.4: Skeletons of the topological states for a three-source system with strengths 1, $\epsilon_1 > 0$ and $\epsilon_2 > 0$ in the plane $z = 0$. The stars represent sources, the dots are null points where the field vanishes, the thick curves are spine field lines, the dashed lines are fan field lines and the thin lines are general field lines within each topological region.

(viii) Triangular State, $\epsilon_1, \epsilon_2 > 0$

A sheaf of three separatrix walls meet at a spine field line that goes up into the region $z > 0$ from a null located in the $z = 0$ plane between the three sources. These three walls again divide the space into three regions which each contain a source. Each wall contains another null point whose spine field lines connect to two different sources. The spines of all three of these nulls are configured in a triangular shape in the $z = 0$ plane.

2.3.3 General Behaviour

The system has eight stable topological states and four parameters. By varying the parameters, the system can bifurcate from one stable state to another.

To begin to comprehend the nature of the bifurcations of the system, it is useful to consider two special cases with $\epsilon_1 = \epsilon_2 = \epsilon$ so that the two sinks are of equal strength: in one case fix a close, but not equal, to 1; in the other case take $a \gg 1$. Note that the additional case when $a = 1$ is a topologically unstable case which exhibits unique

behaviour due to its balanced nature (Priest et al., 1997).

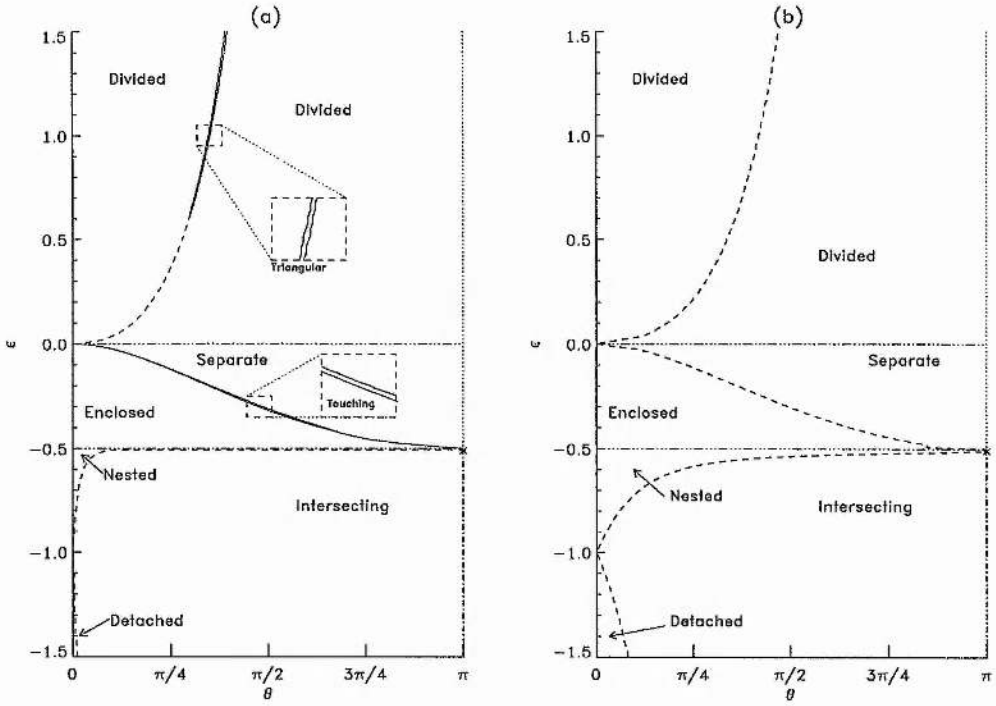

Figure 2.5: The regions in parameter space where the stable topological states exist when $\epsilon_1 = \epsilon_2 = \epsilon$ for two cases: (a) a is close to 1 (figure is plotted for $a = 1.05$) and (b) $a \gg 1$ (figure is plotted for $a = 2$). The bold curves are local bifurcation lines and the dashed curves are global bifurcation lines. The dot-dashed line shows where null rings exist, while the dot-dot-dot-dashed lines indicate where other global changes occur, and the dotted line is a line of reflection. The star indicates a saddle-node Hopf bifurcation point.

The diagrams of parameter space for these cases are shown in figure 2.5(a) and figure 2.5(b). The region where $\pi < \theta \leq 2\pi$ is a reflection of the region $0 \leq \theta < \pi$ in the line $\theta = \pi$. In both cases the space is divided into three sets of regions by the lines $\epsilon = 0$ and $\epsilon = -0.5$. When $\epsilon = 0$ the system degenerates to the one-source system, and when $\epsilon = -0.5$ the total strength of the system is balanced and one of the null points goes to infinity, causing the field at a large distance to look bipolar.

2.4 One Positive and Two Negative Sources

$(-0.5 < \epsilon < 0)$

2.4.1 Topological change during local bifurcation ($a \approx 1$)

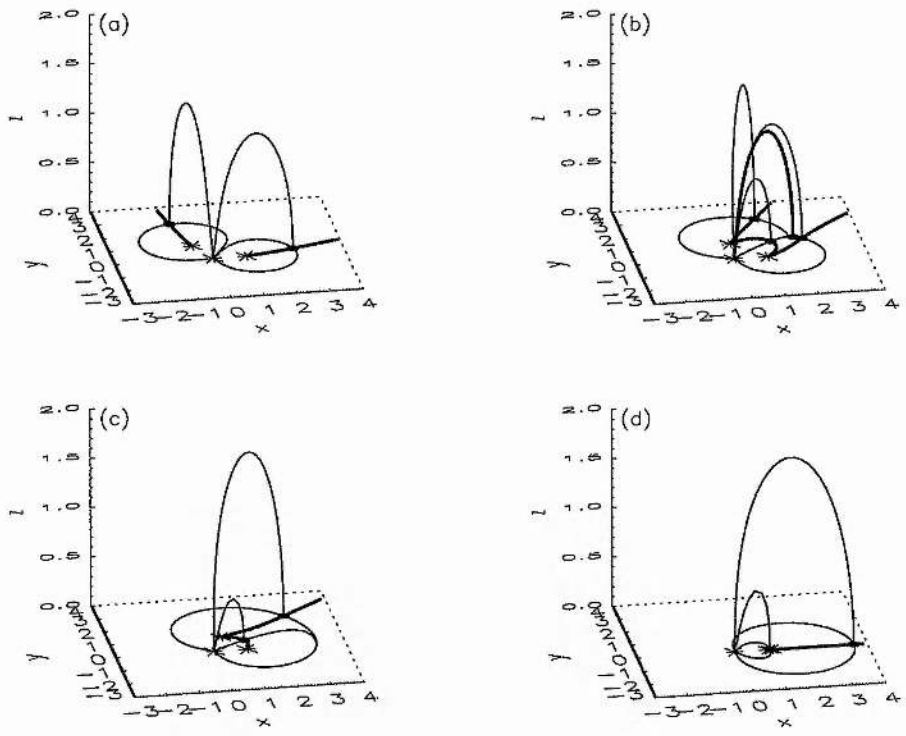

Figure 2.6: Changes in the skeleton produced by local bifurcations, showing (a) the separate state, (b) the touching state, (c) the enclosed state just after bifurcation, and (d) the enclosed state when the angular separation of the sources vanishes ($\theta = 0$).

Consider, first of all, the region of parameter space where $-0.5 < \epsilon < 0$, the middle region of figure 2.5(a). As the parameters a, ϵ and θ vary, the system can bifurcate locally. Suppose the system begins in the separate state (figure 2.6a) and the angular separation (θ) of the nulls is reduced, so that the separatrix domes begin to come together. After a bifurcation the two domes touch along a shared separatrix wall (figure 2.6b). As the angular separation continues to decrease, one of the domes starts to

protrude into the other until, at another bifurcation, it separates from the outer dome and is completely enclosed (figure 2.6c). This pair of bifurcations is illustrated in figure 2.6, which shows how the spine curves and the fan field lines, which form the separatrix surface, behave under bifurcation. In each case one field line (either a fan or spine field line) is drawn arching out of the xy-plane from the central source to each of the nulls that is present.

2.4.2 Nature of local bifurcation ($a \approx 1$)

As a local bifurcation curve in figure 2.5(a) is crossed, either a new null point is formed and splits into two separate nulls, or two nulls coalesce to form a single null point which is then annihilated. It is the combination of these processes which takes the system from the separate state through the touching state and into the enclosed state. Figure 2.7(a) shows the two separate domes which come together to form a new null point (figure 2.7b). This state is topologically unstable, however, since it represents a point on the bifurcation curve in figure 2.5, and so the new null splits into two separate nulls and gives rise to the touching state (figure 2.7c). As the angular separation decreases further (figure 2.7d) one of the new nulls approaches one of the old null points. These two nulls then coalesce to form a second-order null point (figure 2.7e), which is topologically unstable and is annihilated at a second bifurcation into the enclosed state (figure 2.7f).

2.4.3 Analytical model for local separator bifurcations ($a \approx 1$)

It is possible to construct a simple analytical model to illustrate the behaviour of the above bifurcations which, in the context of this work, is referred to as a 'separator' bifurcation, since a separator joining two nulls is either created or destroyed during the bifurcation. It is a three-dimensional generalization of a two-dimensional saddle-node

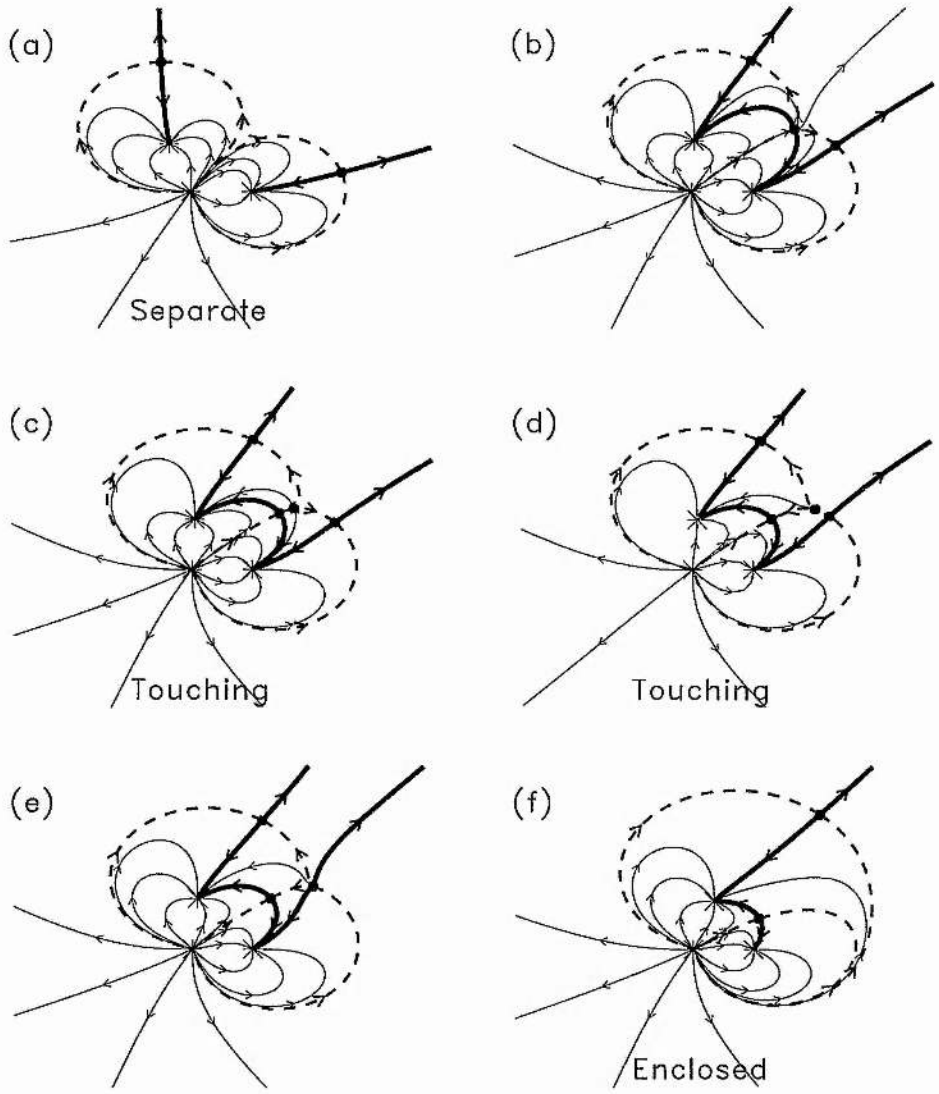

Figure 2.7: Changes of the skeleton in the plane $z = 0$ due to a local bifurcation (b) from the separate state (a) to the touching state (c,d) and another local bifurcation (e) to the enclosed state (f). At bifurcation (b) a new second-order null is created, which then splits into two first-order nulls. At bifurcation (e) two nulls coalesce to form a second-order null which then disappears.

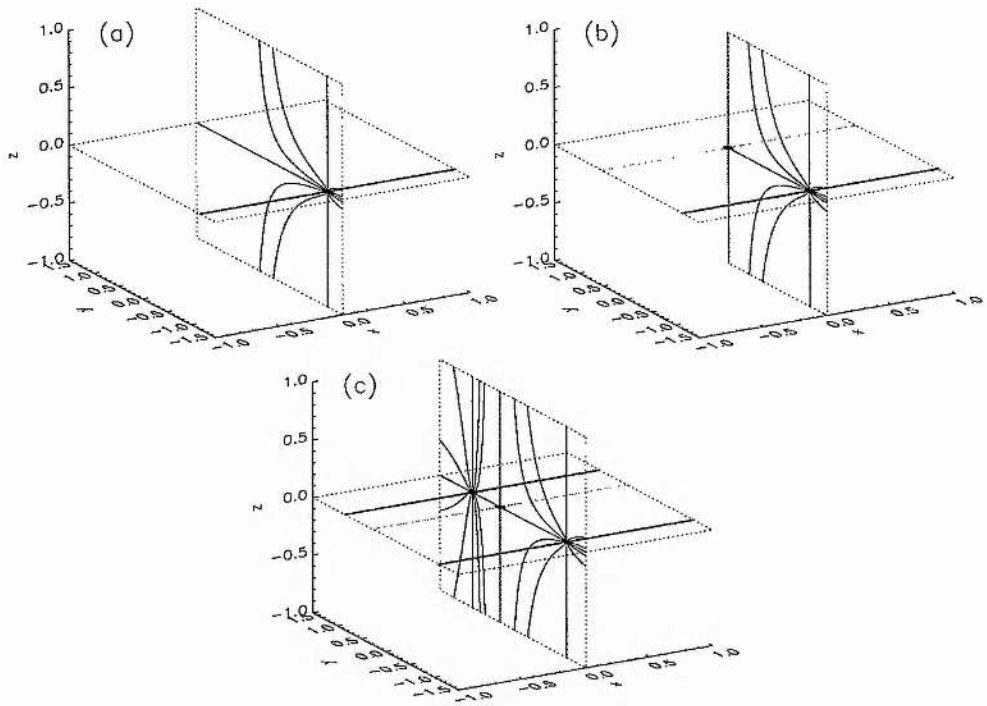

Figure 2.8: Skeletons for an analytical model of the local separator bifurcation, showing (a) a single null before bifurcation, $\lambda = -0.5 < \frac{-2}{3\sqrt{3}}$, (b) the appearance of the second-order null at bifurcation, $\lambda = \frac{-2}{3\sqrt{3}}$ and (c) the two linear nulls after bifurcation, $\lambda = -0.3 > \frac{-2}{3\sqrt{3}}$. Although this thesis is only concentrating on the space where $z > 0$, the region where $z < 0$ is also plotted to illustrate the null point behaviour.

bifurcation (Guckenheimer and Holmes, 1986). Consider magnetic fields of the form

$$\mathbf{B}(\mathbf{r}) = \begin{pmatrix} x(1+3y^2) \\ \lambda - y(y^2-1) \\ -2z \end{pmatrix}, \tag{2.4}$$

which pass through a sequence of states as the parameter λ varies and possess two bifurcations, when $\lambda = \pm\frac{2}{3\sqrt{3}}$.

When $\lambda < -\frac{2}{3\sqrt{3}}$ there is a single null at $(0, y, 0)$ where y satisfies $y(y^2-1) - \lambda = 0$. The fan of the null lies in the $x = 0$ plane, and the spine is perpendicular to the fan.

When $\lambda = -\frac{2}{3\sqrt{3}}$, the y-component of the magnetic field vanishes when

$$(y + \frac{2}{\sqrt{3}})(y - \frac{1}{\sqrt{3}})^2 = 0, \tag{2.5}$$

so that a new second-order null is created at $(0, \frac{1}{\sqrt{3}}, 0)$. This is topologically unstable and as λ increases the new null splits into two linear nulls, the three nulls lying on the line $x = z = 0$. The fans of the two outer nulls lie in the $x = 0$ plane and meet at the spine of the middle null. The fan of the middle null lies in the $z = 0$ plane between the spines of the outer two nulls, as demonstrated in figure 2.8.

As λ increases further, the original null and the middle null approach each other. They coalesce when $\lambda = \frac{2}{3\sqrt{3}}$ and form a second-order null, which is then annihilated when $\lambda > \frac{2}{3\sqrt{3}}$ in a process opposite to that of the first bifurcation.

2.4.4 Local bifurcation when $a = 1$

When $a = 1$ the bifurcation between the separate state and the touching state is the same, but the bifurcation between the touching state and a topologically unstable variant of the enclosed state is different. Because of the symmetry, rather than just two null points coalescing, all three null points coalesce and leave behind a single null, in a pitchfork bifurcation from the touching to the enclosed state (see figure 12 of Priest et al., 1997).

2.4.5 Global bifurcation when $a \gg 1$

As a increases, the bifurcation line between the separate and touching states in figure 2.5(a) approaches the bifurcation line between the touching and enclosed states. These two bifurcation lines merge to form a single global bifurcation line, as shown in figure 2.5(b), when one of the domes is a lot larger than the other.

During bifurcation the two separatrix domes now approach each other, but instead of meeting and forming a new null, they meet at the null point of the smaller dome and an

unstable field line connecting the two null points is formed, this is known as a saddle connection. This then splits and bifurcates straight from the separate state into the enclosed state (see figure 10 of Priest et al., 1997).

2.4.6 Analytical model for global spine-fan bifurcation ($a \gg 1$)

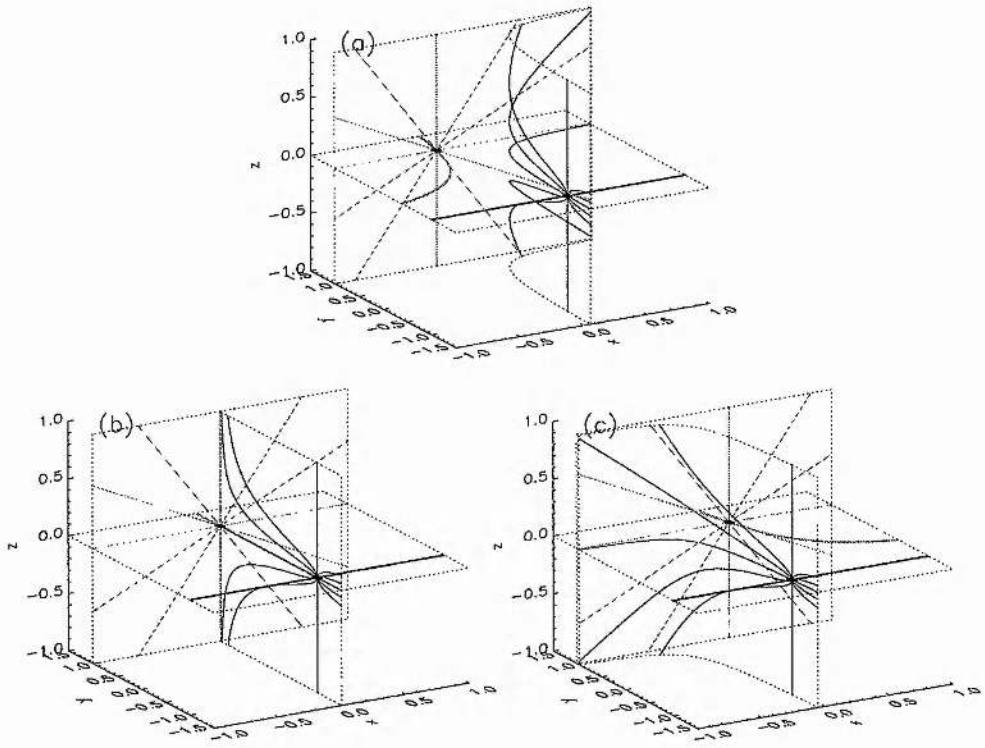

Figure 2.9: Skeletons of the analytical model for global spine-fan bifurcation, showing the field structure (a) before ($\lambda = -0.1$), (b) during ($\lambda = 0.0$) and (c) after ($\lambda = 0.1$) bifurcation. The region where $z < 0$ is also plotted to illustrate the null point behaviour.

An analytical model that describes this bifurcation is given by a parameterized field of

the form

$$\mathbf{B}(\mathbf{r}) = \begin{pmatrix} \lambda - x(y - \frac{1}{2}) \\ \frac{1}{2}(y^2 - 1) \\ -\frac{z}{2} \end{pmatrix}. \tag{2.6}$$

In the context of this work, the bifurcation is referred to as a 'spine-fan' bifurcation, since the spine of one null lies in the fan of another null at the moment of bifurcation. The nulls are located at $(2\lambda, 1, 0)$ and $(-\frac{2}{3}\lambda, -1, 0)$. This three-dimensional bifurcation is a natural extension of the two-dimensional saddle bifurcation (Glendinning, 1994; Guckenheimer and Holmes, 1986), since the separatrix surfaces are everywhere perpendicular to the $z = 0$ plane.

Figure 2.9 demonstrates the bifurcation process. Before bifurcation ($\lambda < 0$), the fan of the front null can be seen curving to the right while the spine of the back null curves to the left, so that the field lines between the planes $y = \pm 1$ can travel from right to left (i.e., $B_x < 0$ at $x = 0$). At bifurcation ($\lambda = 0$) the spine of the front null connects to the other null so that the two nulls are joined by a saddle connection. After bifurcation ($\lambda > 0$) the direction of the field lines between $y = \pm 1$ has changed so that the fan of the front null now curves to the left and the spine of the other null curves to the right.

2.5 One positive and two negative sources ($\epsilon < -0.5$)

2.5.1 Topological change during global bifurcation

The bifurcations in figure 2.5 between the nested state and the intersecting state, or that between the detached state and the intersecting state, are both global bifurcations. The type of bifurcation in both cases is the same and the behaviour is very similar, so it suffices to look at just one of the cases, for example where $\epsilon < -1$.

Starting with no angular separation ($\theta = 0$), such a system is in the detached state (figure 2.10a). As θ increases, the separatrix wall curls around on to half of the separatrix dome. The two separatrices then touch at a field line, known as a separator, in

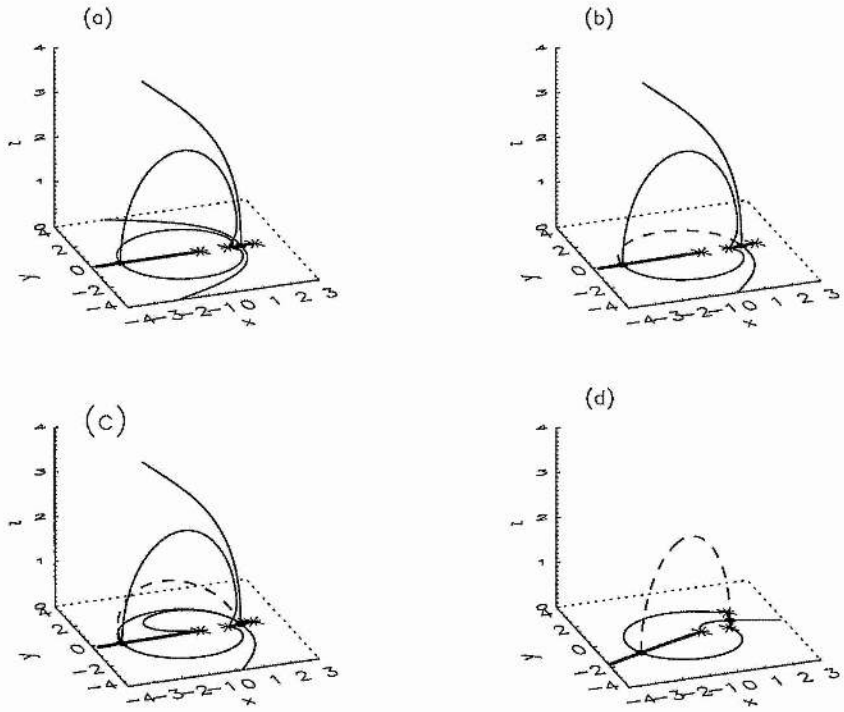

Figure 2.10: Changes in the skeleton from (a) the detached state to (c) the intersecting state due to (b) a global bifurcation as the angular separation increases. The dashed curve is a separator joining one null to the other. (d) As the angular separation increases further, the separator progresses towards the top of the dome.

the $z = 0$ plane which connects the two null points. This is the moment of bifurcation. As the angular separation is increased further, the separatrix wall intersects the dome, although the separator survives as the intersection of the dome and the wall.

2.5.2 Analytical Model for Global Separator Bifurcation

The global bifurcation considered here is different from the one considered in section 2.4.5 and section 2.4.6. It is referred to as a 'global separator bifurcation' and is another three-dimensional extension of a two-dimensional heteroclinic saddle bifurcation. Instead of a spine field line and a fan field line coinciding to form a separator,

two fan surfaces touch at the moment of bifurcation to form a separator.

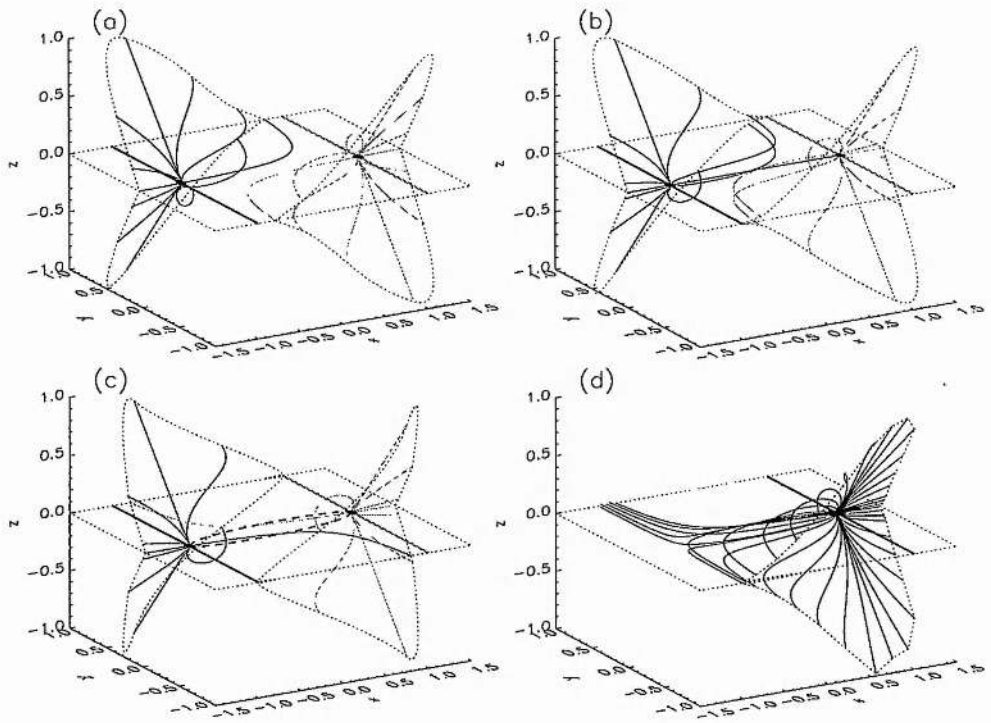

Figure 2.11: Skeletons of the analytical model for the global separator bifurcation showing the nulls, spines and the fan field lines. The field structure is indicated (a) before ($\lambda = -0.1$), (b) during ($\lambda = 0$) and (c) after ($\lambda = 0.1$) bifurcation, the dashed lines indicating the separators connecting the two nulls. (d) shows the structure of one of the separatrix surfaces after bifurcation ($\lambda = 0.1$) by plotting additional field lines. The region where $z < 0$ is also plotted to illustrate the null point behaviour.

A model for this process has magnetic field described by the equation

$$\mathbf{B}(\mathbf{r}) = \begin{pmatrix} 1 - x^2 \\ 3(z + xy - \lambda) \\ -xz \end{pmatrix} \tag{2.7}$$

with null points at $(1, \lambda, 0)$ and $(-1, -\lambda, 0)$. The bifurcation is demonstrated in figure 2.11. When $\lambda < 0$ there are two separate curved separatrix surfaces which do not intersect. When $\lambda = 0$ the two surfaces intersect in the $z = 0$ plane along the newly

formed separator connecting the two nulls. When $\lambda > 0$ the two surfaces intersect (cf Lau and Finn, 1990) along a separator lying out of the $z = 0$ plane between the two nulls (note that if the region $z < 0$ is also considered, then there is actually a pair of separators, the second being the mirror of the first in the $z = 0$ plane). As λ increases above 0, the separator moves along the surfaces by continual reconfiguration of field lines as the null points are displaced. The structure of one of the separatrix surfaces after bifurcation can be seen in detail in figure 2.11(d). The two surfaces have the same structure, and are symmetrical under a rotation of π about the z-axis.

2.6 Three positive sources

2.6.1 Topological changes during global bifurcation

Consider the case where the three sources have the same polarity. Suppose first that the system is in the divided state with a small angular separation (θ) as shown in figure 2.12(a). As θ is increased, the two separatrix surfaces will deform, with one separatrix approaching the other and the spine curve approaching the other null point (figure 2.12b). At bifurcation (figure 2.12c) the system is in a topologically unstable state and the two null points are joined by a separator, which represents the merger of the spine of one null with a fan line of the other null. If the angular separation is increased further, then the system returns to a divided state (figure 2.12d) except that the separator splits into a fan line and a spine line on the opposite side from which they merged. This is another example of the global spine-fan bifurcation discussed in section 2.4.6.

In the initial divided state (figure 2.12a) one of the separatrix walls separates the flux of the origin source from the flux of source ϵ_1, and the other separatrix wall separates the flux from the source ϵ_1 from the flux of source ϵ_2. In the final divided state (figure 2.12d) the difference is that the second separatrix wall now separates flux from source ϵ_2 with flux from the source at the origin instead of flux from source ϵ_1.

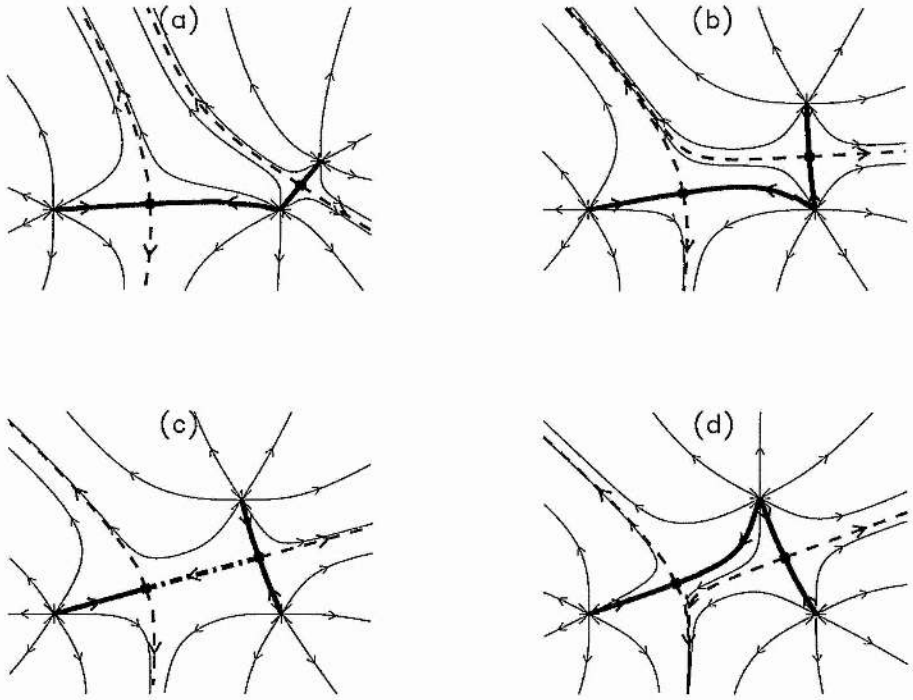

Figure 2.12: Changes of the skeleton in the plane $z = 0$ due to a global spine-fan bifurcation from one divided state (a) to another (d). (b) represents the state just before bifurcation and (c) at bifurcation. The dot-dash line is a topologically unstable spine-fan separator that joins the two nulls and represents the spine of one null and a fan line of the other.

2.6.2 Local bifurcation

Another type of bifurcation is possible when all the sources have the same polarity. If the system is more balanced, i.e., the sources are all roughly the same strength and are roughly equidistant from one another, it is possible to obtain a local bifurcation.

Again, suppose the system begins in the divided state (figure 2.13a) and the angular separation is increased so that the separatrix walls approach one another. Instead of meeting at an existing null point, the separatrix walls now coalesce along part of their length and form a new null in the plane $z = 0$ (figure 2.13b). This is a topo-

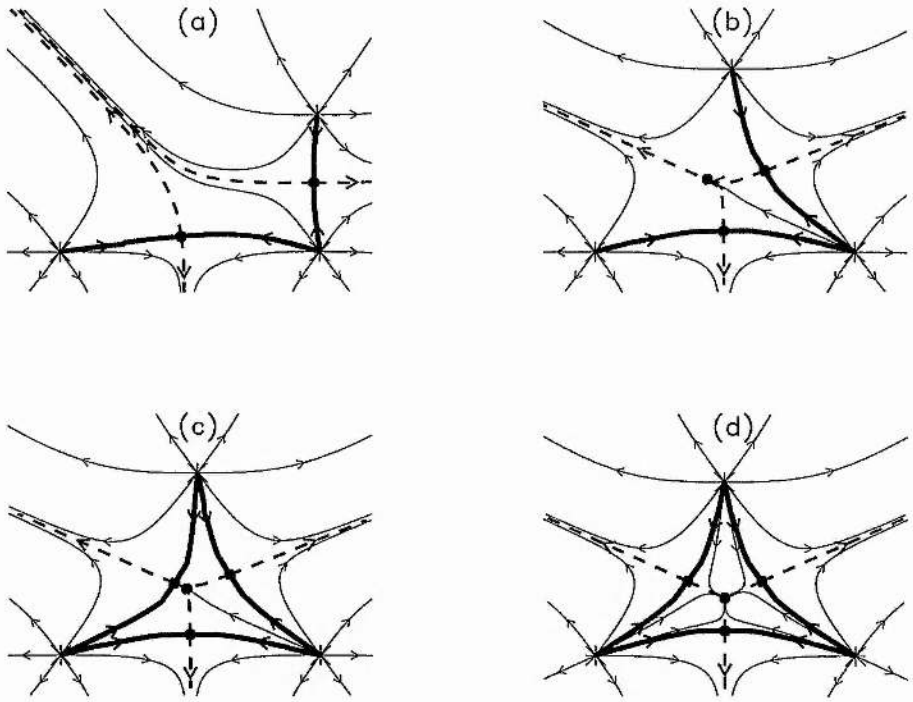

Figure 2.13: Changes of the skeleton in the plane $z = 0$ due to a local bifurcation from (a) a divided state to (d) a triangular state. (b) represents the bifurcation state with a new second-order null and (c) the state just after bifurcation with two new linear nulls.

logically unstable second-order null and splits into two linear nulls, thus forming the triangular state (figure 2.13c,d). Such a bifurcation, which is of local separator type (section 2.4.3), only occurs when the system is roughly balanced and does not exist when $a \gg 1$.

2.6.3 Case $a = 1$

When $a = 1$ there is another non-generic situation in which the topological behaviour is slightly different. The parameter space for $\epsilon > 0$ is split into three regions, as shown in figure 2.14. The connected state, which is the topologically unstable state

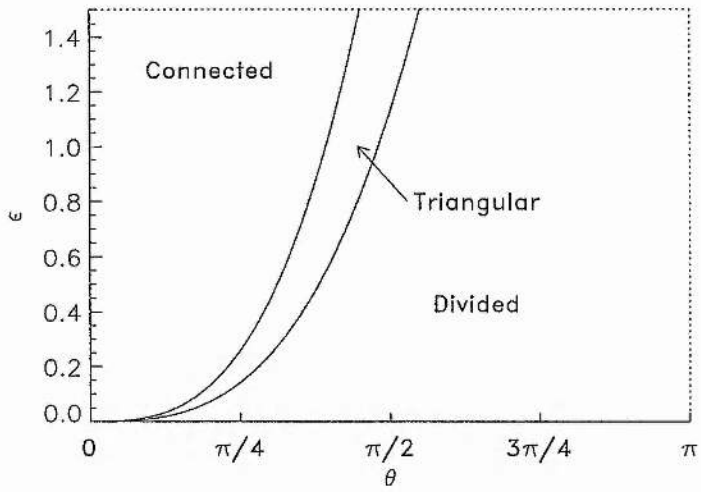

Figure 2.14: Sketch of parameter space for $a = 1$ and $\epsilon > 0$, showing local bifurcation lines from connected to triangular to divided states.

in figure 2.13(c), becomes topologically stable with respect to the parameters ϵ and θ. Thus, if θ is initially small and increases, then the connected state (figure 2.15a) bifurcates into the triangular state (figure 2.15b) and then on into the divided state.

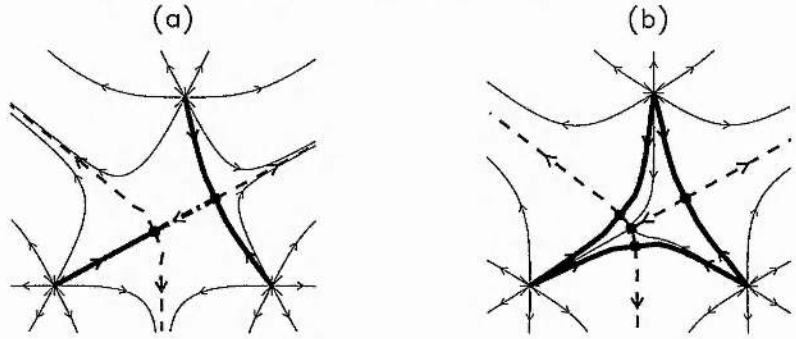

Figure 2.15: The skeleton in the plane $z = 0$ when $a = 1$, showing first of all one of the nulls in the connected state (a). It then splits into three separate nulls under a pitchfork bifurcation into the triangular state (b).

The bifurcation from the connected state to the triangular state (figure 2.15) is a pitchfork bifurcation. As the angular separation is increased, the null that is located where the two separatrix walls meet splits into three separate null points, which form the

basis for the triangular state.

2.7 Null ring and the Hopf bifurcation

2.7.1 Null ring

In figure 2.5, the parameter sketch for $\pi < \theta \leq 2\pi$ is a reflection in the line $\theta = \pi$, indicated by a dotted line. However, on this line where it borders the intersecting state there is a bifurcation line which separates the intersecting state from itself!

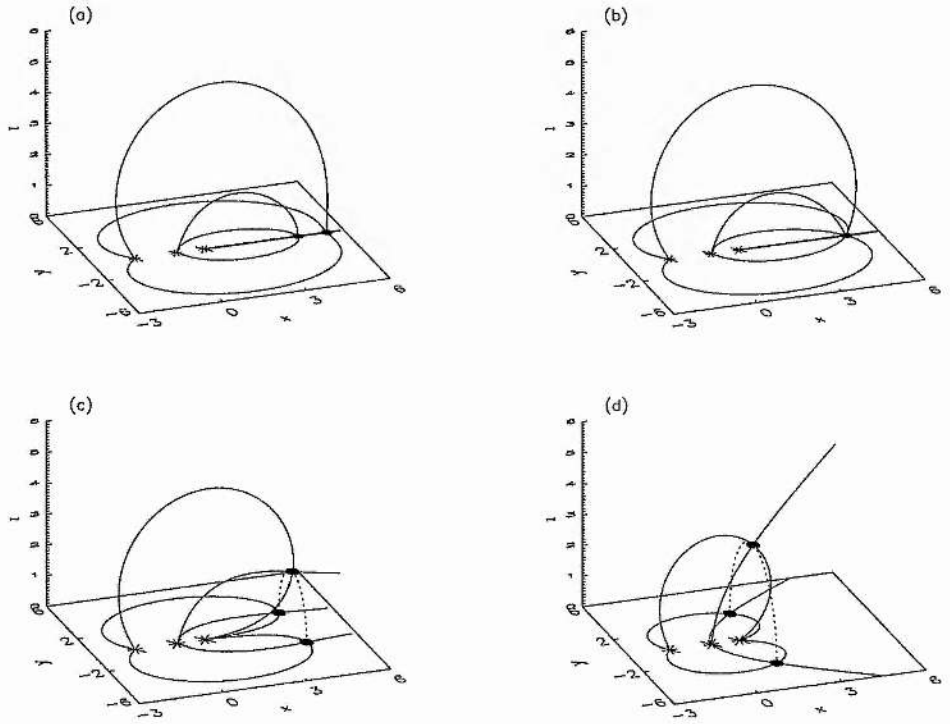

Figure 2.16: Skeleton of the system when $\theta = \pi$. (a) The two linear nulls on the x-axis coalesce into (b) a single second-order null point, which expands away from the x-axis to form (c) and (d) a null ring (shown dotted).

What happens is that, as the bifurcation line is approached, the magnitude of the field strength reduces along the separator in the intersecting state. When the bifurcation

line is reached, this field strength vanishes and the separator becomes a null ring, figure 2.16(d). In other words, when $\theta = \pi$ the three sources lie in a line along the x-axis, so the system has rotational symmetry about the x-axis. The rotational symmetry implies that any null point not on the x-axis and lying in a plane through the x-axis must become a null ring in three dimensions. This state is topologically unstable since a perturbation in the angular separation will destroy the rotational symmetry and the system will revert to the standard intersecting state.

2.7.2 Saddle-node-Hopf bifurcation

As ϵ increases in value, the null ring decreases in size until it becomes a single point on the x-axis. This is a saddle-node-Hopf bifurcation point and occurs where the bifurcation line $\theta = \pi$ crosses the bifurcation line separating the nested state and the intersecting state in figure 2.5. As ϵ increases further, the null point splits into two separate null points which lie on the x-axis, a topologically unstable variant of the nested state, as can be seen in figure 2.16.

2.8 Case when $\epsilon_1 \neq \epsilon_2$

It transpires that the general case $\epsilon_1 \neq \epsilon_2$ produces no new topological behaviour so that the case when $\epsilon_1 = \epsilon_2$ contains all the types of bifurcation of a general three-source system.

Figure 2.17 shows diagrams of parameter space for the cases where there is one positive and two negative sources. Comparison with figure 2.5 shows that the bifurcation lines bound the same types of topological region as before, and so there are no new kinds of bifurcation.

Again as a increases, the touching state region in figure 2.17(a) shrinks and disappears to form a global bifurcation curve in figure 2.17(b) between the separate and enclosed states. As θ tends to 0 the touching and separate state regions shrink towards the $\epsilon_1\epsilon_2$-

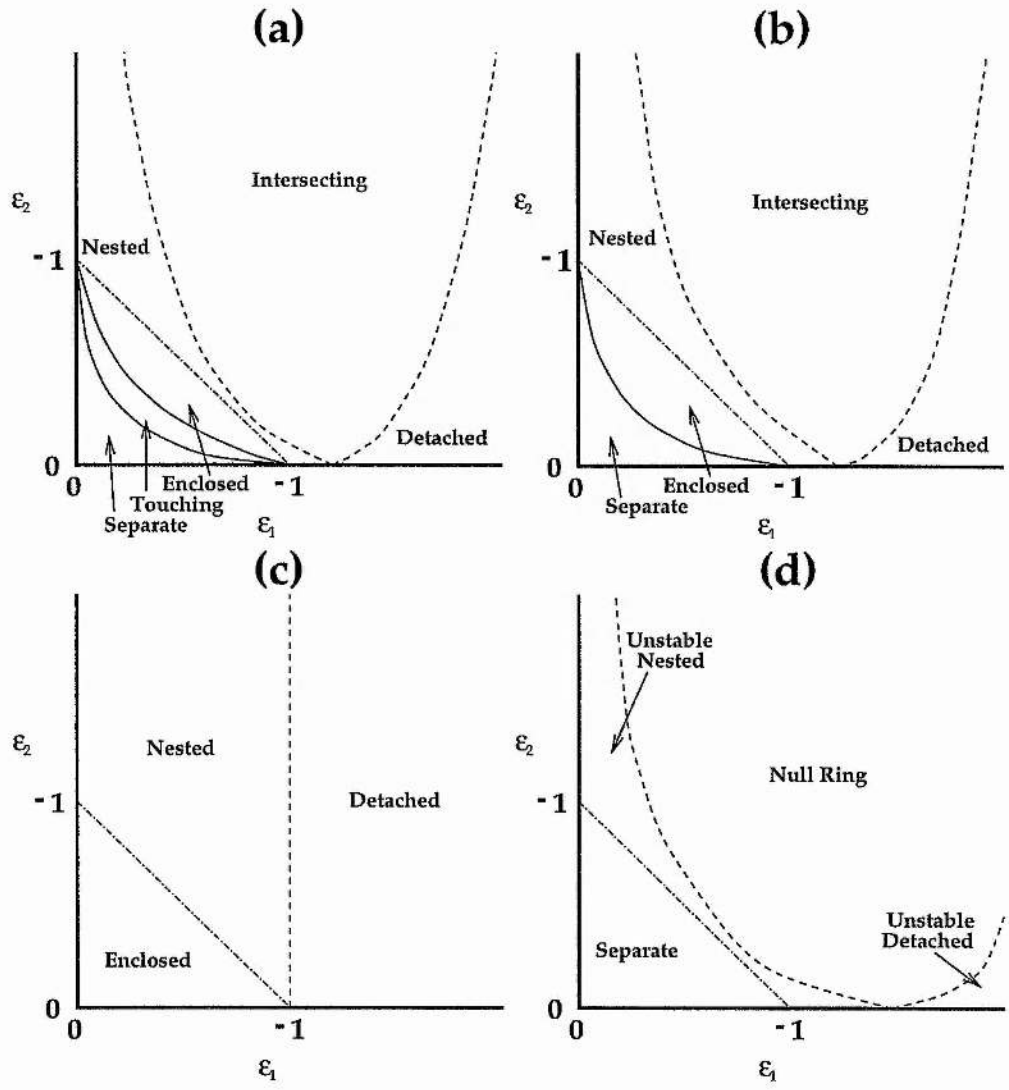

Figure 2.17: Bifurcation diagrams showing schematically the effect on the different topological states of varying the source strengths ϵ_1 and ϵ_2 with (a) $a \approx 1$ and $0 < \theta < \pi$, (b) $a >> 1$ and $0 < \theta < \pi$, (c) $\theta = 0$ and (d) $\theta = \pi$. The bold lines represent local bifurcations, the dashed lines are global bifurcations, and the dot-dashed lines indicate the bifurcation where the sources are balanced and a null point has gone to infinity.

axes and disappear when $\theta = 0$ (figure 2.17c). In the other direction, as θ tends to π, the touching and enclosed state regions shrink towards the line $\epsilon_1 + \epsilon_2 = -1$ and disappear when $\theta = \pi$ (figure 2.17d).

The bifurcation point where the nested state, the detached state and the ϵ_1-axis meet varies with θ. When $\theta = 0$ the bifurcation point is located at $\epsilon_1 = -1$ (figure 2.17c), and it moves further along the ϵ_1-axis as θ increases.

When $\theta = \pi$ the regions of the unstable nested and detached states are separated from the null ring state by a saddle-node-Hopf bifurcation curve, dashed in figure 2.17(d). The case when all the sources have the same polarity displays the similar bifurcation behaviour in the $\epsilon_1 \neq \epsilon_2$ case as it does in the $\epsilon_1 = \epsilon_2$ case.

2.9 Summary

This chapter has shown that three-source systems display a rich variety of interesting topological behaviour. There is a wide range of stable and unstable topological states which can bifurcate, either locally or globally, between one another in a complex manner. This type of behaviour of the magnetic field could act as a trigger for solar coronal events such as the formation of prominences or the eruption of coronal mass ejections. Some of the topologically stable states correspond to the more stable and longer lasting loop structures. For instance, Longcope and Cowley (1996) use a magnetic field configuration which is topologically equivalent to the intersecting state as a basis for the construction of a current ribbon in three dimensions.

Active regions on the Sun may be extraordinarily complex with many different magnetic sources in the photosphere (Inverarity and Priest, 1999). However, the main building blocks of these complex magnetic fields are likely to be the three-source elements that have been considered here. For example, consider a topological state that contains three separate clusters of sources. Locally, the magnetic field of individual clusters may form topological states from lower-order cases, but globally the three

clusters would often display the same properties as a three-source system.

Thus, a knowledge of three-source topological behaviour allows development of a better understanding of such complex magnetic fields.

Chapter 3

Four-Source Topology

3.1 Introduction

Consider the addition of a fourth source to the three-source system described in chapter 2. Even by making the assumption that all the sources are confined to the $z = 0$ plane, the source can still move in the x- and y- directions, and the source strength may vary. So the extra source adds three new parameters to the system, giving a total of seven parameters. The increased number of parameters in the equation describing the magnetic field due to four sources makes a fully comprehensive analysis prohibitive, but a focus on specific behaviour which is both new and generic for four sources would be informative. This is why the four-source case has only been touched upon briefly in the literature (Molodenskii and Syrovatskii, 1977; Gorbachev et al., 1988; Gorbachev and Somov, 1988; Bungey et al., 1996).

Four-source, and higher-order multi-source cases, will often exhibit much of the behaviour found in the three-source case. Consider, for example, a five-source case with the topological state consisting of four separate separatrix domes, an extension of the three-source separate case. Any two neighbouring domes could bifurcate into a touching or enclosed state in exactly the same manner as the three-source case does.

This chapter will consider certain cases designed to highlight behaviour which is not

manifested by the three-source case. The general tactic for doing this is to fix the positions and strengths of three of the sources and vary the position of a fourth source of fixed strength. This will generate two-dimensional bifurcation diagrams which will be used to investigate the topological behaviour of the system.

Section 3.2 describes how these bifurcation diagrams are generated. Section 3.3 investigates the behaviour of separators when a new null is introduced. Section 3.4 considers the possibility of null points leaving the $z = 0$ plane.

3.2 Generating Bifurcation Diagrams

3.2.1 The method of generation

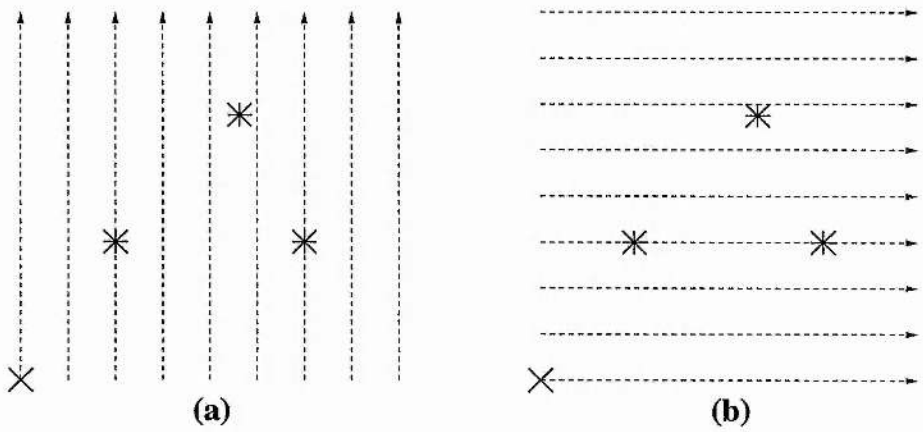

Figure 3.1: Bifurcation points are found for motion of a fourth source along (a) a sequence of vertical lines and (b) a sequence of horizontal lines.

The most general way of finding the changes in topology between two states, is to search for changes in connectivity of the spine field lines and the fan field lines. The two-dimensional problem can be reduced to a series of one-dimensional problems by fixing one of the parameters and scanning along the lines where the second parameter varies (figure 3.1). This is done for both parameters, so there are lines scanned in the direction of variation of the x-parameter (figure 3.1a) and in the direction of variation

of the y-parameter (figure 3.1b). In this thesis, bifurcation diagrams will be plotted with a resolution of 200 lines in each direction.

Along each line, five equally spaced points are selected and the field line connectivity for the parameter values of each point calculated. If there is a change of connectivity between two consecutive points, then the line segment between the two points is split into five points and the process is repeated (as demonstrated in figure 3.2). This is taken to a maximum of five levels of depth, so the resolution of the bifurcation diagrams along the scanned lines is $\frac{1}{4^5}(S_{max} - S_{min})$.

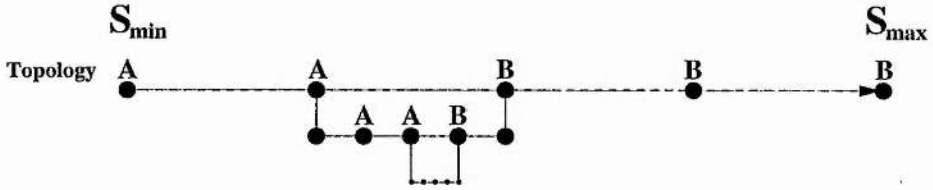

Figure 3.2: Each line scanned is split into five points. If there is a change from topology A to topology B between two points, then that section is split into a further five points, and the analysis is repeated.

3.2.2 Problems with this method

There are two distinct problems with this method of generating bifurcation diagrams. The first is noise. For each bifurcation diagram generated with this method, there will be a scattering of apparent bifurcation points which do not actually exist, this is due to mis-tracking of null points. The positions of the null points for each position must be known in order to calculate the connectivity of the spine and fan field lines. This is done using a repeated Newton-Raphson iterated null-finding method starting from an initial known configuration. Due to the small radius of convergence of some nulls, this method can occasionally lose the null point that was being tracked and settle on another null point, which inevitably has different connectivity than the null being tracked, so an apparent bifurcation is registered. Checks are made to reduce the presence of this type of 'noise'.

The second problem is that, near to any of the fixed sources, an echo of the bifurcation line can appear or the line can disappear. This is because at these points the varied source is very close to one of the fixed sources, which often has an associated null point very close by as well. The close proximity of these three features makes the bifurcation lines in these regions difficult to track. The problem is that each of the sources or the null points is actually considered with a tiny sphere of attraction: that is, if a field line comes within a certain radius of source or null point, it is assumed that the field line is connected to that source or null point. When the sources are close, these spheres can overlap, or a field line can pass through the sphere of a source to which it is not connected. To reduce this effect, the sphere size is varied to a certain degree, but this has to be balanced against speed of computation.

3.3 Separator Behaviour due to Four Sources

3.3.1 Setting up the model

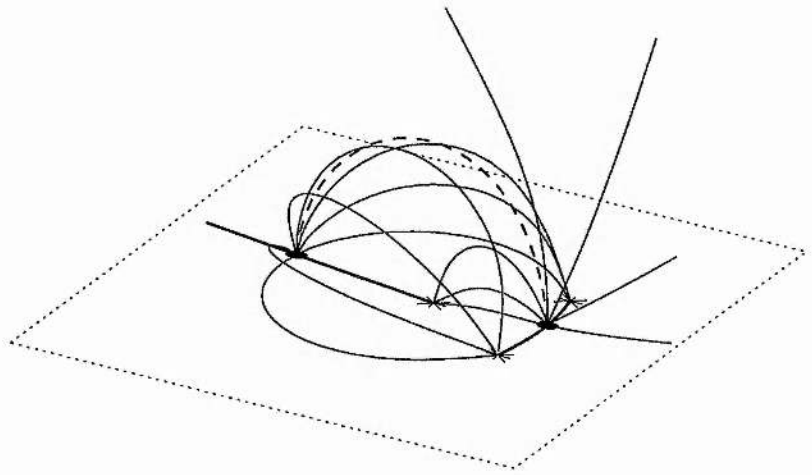

Figure 3.3: The three-source intersecting state, produced by sources located on the $z = 0$ plane at $(0, 0)$, $(1, 0)$ and $(0.5, 0.8)$ with strengths 1, 0.5 and -0.5, respectively. This is used as a starting point to investigate separator behaviour.

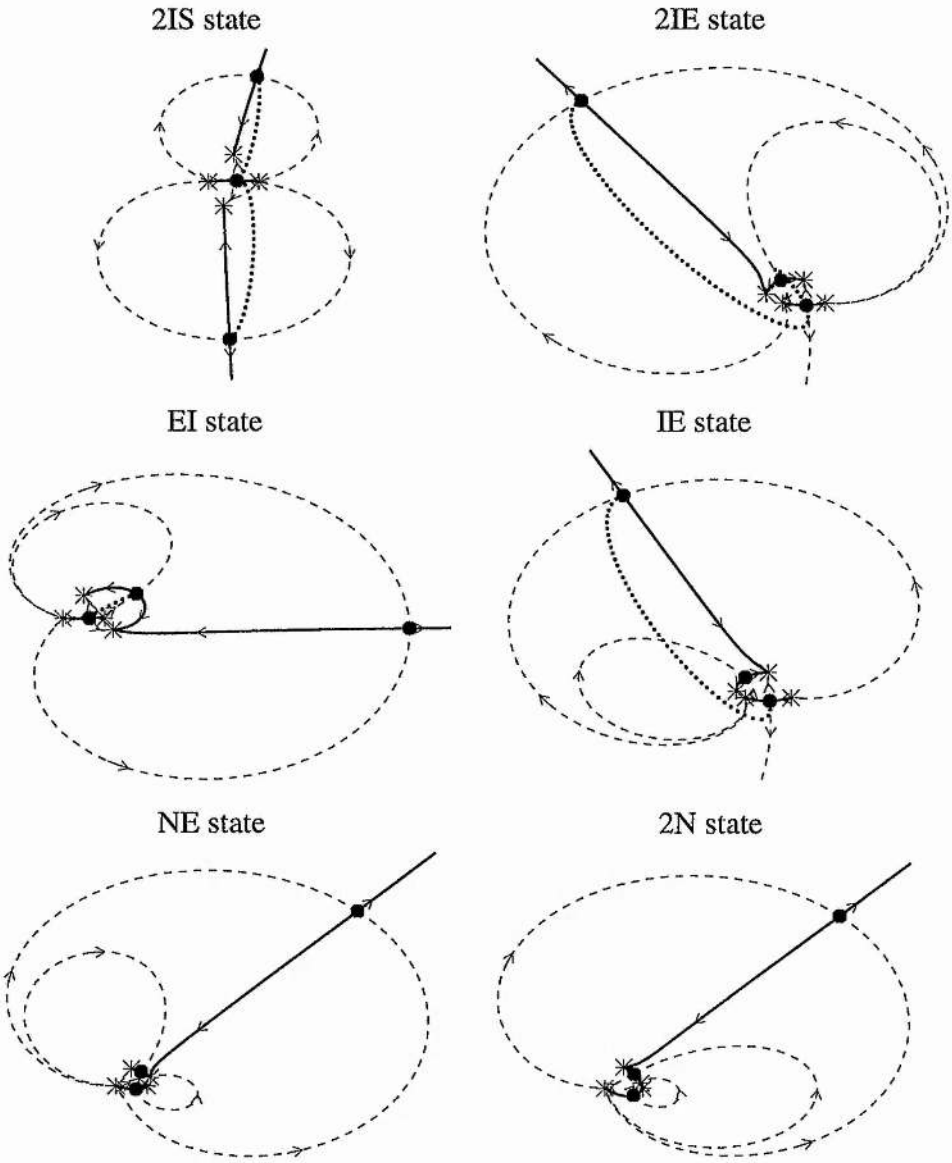

Figure 3.4: Some topological states possible with two positive and two negative sources, plotted in the $z = 0$ plane. The asterisks represent the sources and the dots are null points. The bold lines represent spine field lines and the dashed curves are fan field lines. Dotted lines are the projection of separators on the $z = 0$ plane. The topological states are: (2IS) Double-Intersecting-Separate state, (2IE) Double-Intersecting-Enclosed state (the right-handed variant is plotted), (IE) Intersecting-Enclosed state, (EI) Enclosed-Intersecting state, (NE) Nested-Enclosed state, (2N) Double-Nested state.

Consider the intersecting state produced by three sources which are located on the $z = 0$ plane at $(0, 0)$, $(1, 0)$ and $(0.5, 0.8)$ with strengths 1, 0.5 and -0.5, respectively (as plotted in figure 3.3). These values are chosen since they make the intersecting state very stable. It is not desirable that the parameters of the system be close to a bifurcation line since the introduction of a fourth source may act to push the system across the bifurcation line, and this section aims to investigate the effect of the fourth source on the separator in the intersecting state.

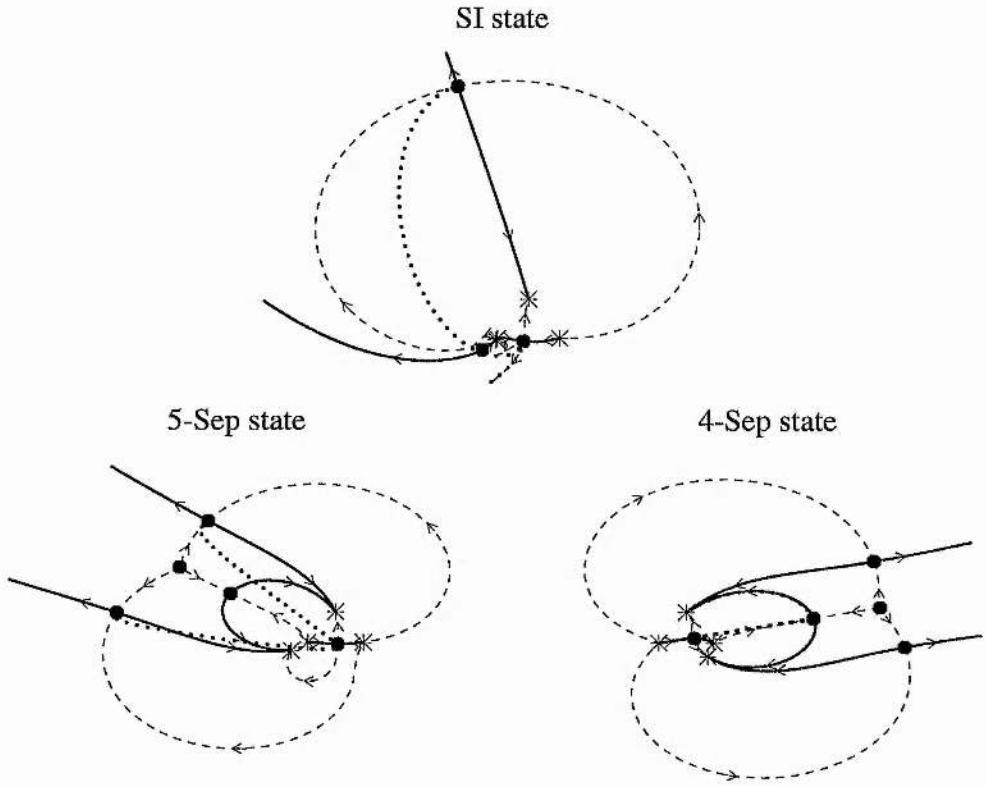

Figure 3.5: Some topological states possible with two positive and two negative sources, plotted in the $z = 0$ plane. The asterisks represent the sources and the dots are null points. The bold lines represent the spine field lines and the dashed curves are fan field lines. Dotted lines are the projection of separators on the $z = 0$ plane. The topological states are: (SI) Separate-Intersecting state, (5-Sep) Quintuple-Separator state and (4-Sep) Quadruple-Separator state.

There are three cases to be investigated: the introduction of a negative source which

makes the total flux negative (the sum of the sources strength is negative); the introduction of a negative source which leaves the total flux positive; and the introduction of a positive source.

The topological states found by doing this will fall into one of two categories, namely, composed states or new states. Composed states are compositions of two three-source states. New states exhibit topological behaviour which is not seen in lower-order cases.

3.3.2 Two positive and two negative sources with negative total flux

Topological states

Now consider the three-source system outlined above and add a fourth source of strength -1.2, this forces the total flux of the system to be negative. There are nine possible topological states that this system can attain, as plotted in figures 3.43.5. Seven of these states are composed states, the remaining two are new states. The composed states have been named to reflect the three source states they are composed of. The states are;

Double-Intersecting-Separate (2IS) state
This state is two intersecting states with the separatrix domes of each intersecting state being separate from each other. They meet along a line which contains two sources of the same polarity and a null point.

Double-Intersecting-Enclosed (2IE) state
This state is two intersecting states with the separatrix dome of one of the intersecting states being enclosed inside the separatrix dome of the other. This state has two variants, a right-handed and a left-handed state, this indicates on which side of the separatrix wall of the enclosing dome, the enclosed dome lies with respect to the source cluster. They meet along a line which contains two sources of the same polarity and a null point.

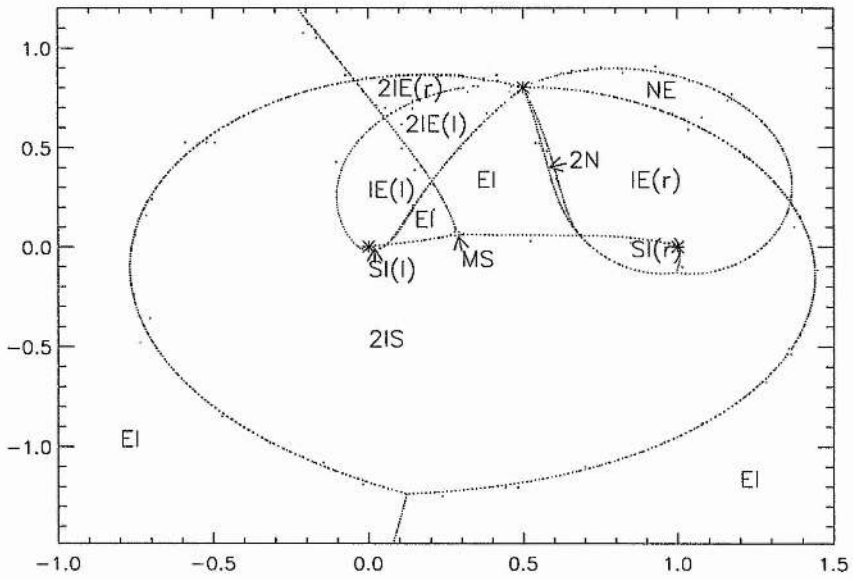

Figure 3.6: Bifurcation diagram showing the regions where a fourth source of strength -1.2 can be placed, with respect to three sources of strengths 1, 0.5 and -0.5 located at (0,0), (1,0) and (0.5,0.8), to obtain the various topological states. (2IS) Double-Intersecting-Separate state, (2IE) Double-Intersecting-Enclosed state, (IE) Intersecting-Enclosed state, (EI) Enclosed-Intersecting state, (NE) Nested-Enclosed state, (2N) Double-Nested state, (SI) Separate-Intersecting state and (MS) Multi-Separator states. l or r indicate whether it is a left- or right-handed version of the topological state.

Enclosed-Intersecting (EI) state

This state is an intersecting state enclosed by a separatrix dome. As the separatrix wall for the intersecting part is completely contained by the enclosing dome, the wall forms another dome.

Intersecting-Enclosed (IE) state

This state is an intersecting state with a separatrix dome enclosed inside the separatrix dome of the intersecting state. The enclosed dome can lie on either side of the separatrix wall of the intersecting part of the state, giving rise to both right-handed or left

handed variants of the state.

Nested-Enclosed (NE) state

This state is a nested state where the outer separatrix dome encloses an additional separatrix dome.

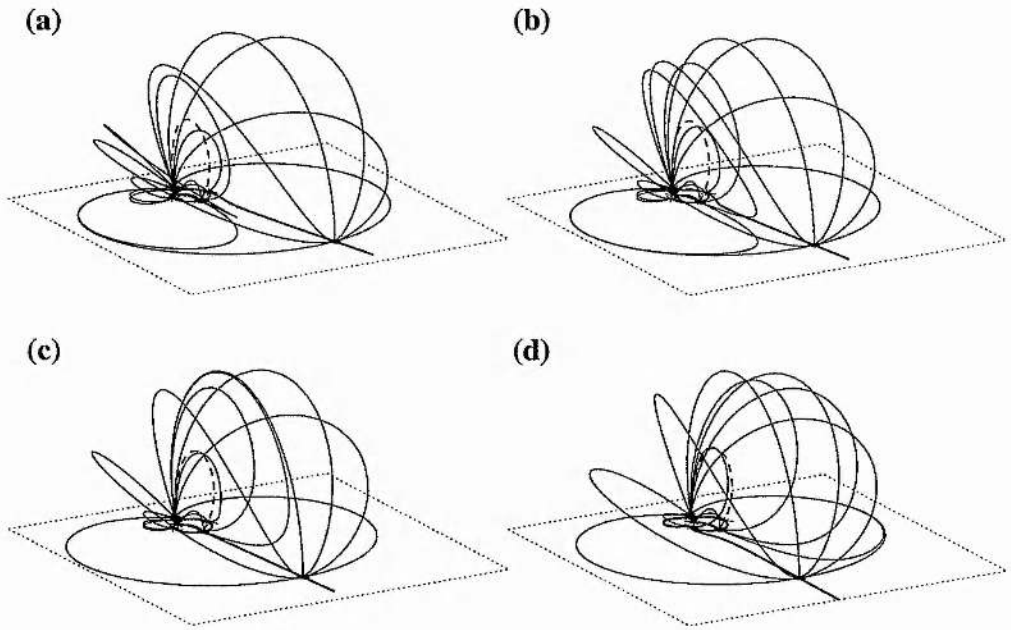

Figure 3.7: Three-dimensional field line plots of the enclosed-intersecting state bifurcating to a reconfiguration of the enclosed-intersecting state. In (a) and (b), the system approaches bifurcation, (c) shows the system at bifurcation and (d) shows the system after bifurcation.

Double-Nested (2N) state

This state has one nested state nested inside another, so there is one separatrix dome which is nested inside another which is nested inside the third outermost separatrix dome. In other words, if the outer separatrix dome was removed, the remaining domes would form a nested state. Similarly, if the innermost separatrix dome where removed, the remaining domes would form a nested state.

Separate-Intersecting (SI) state

This state has an intersecting state with an additional separatrix dome outside that of

the intersecting section. This dome is attached to one of the external sources, and can be thought of as having right-handed and left-handed variants depending on which of the external sources the additional separatrix dome is attached to.

quintuple-separator (5-Sep) state

This state is a new four-source topology. It has five null points and two separators out of the $z = 0$ plane. The separators have one null point in common. Also, one of the nulls has its fan in the $z = 0$ plane, so there are three separators in the $z = 0$ plane. This is one of the multi-separator states.

quadruple-separator (4-Sep) state

This state is also a new four-source topology. It has five null points and a single separator out of the $z = 0$ plane. Also, one of the nulls has its fan in the $z = 0$ plane, so there are three separators in the $z = 0$ plane. This is the other multi-separator state.

Bifurcation behaviour

Most of the topological states produced by this system are compositions of three-source topological states, which means that bifurcation between two composed states is due to the three-source bifurcations discussed in chapter 2.

For example, the bifurcation diagram for this case (figure 3.6) shows that the double-nested state has two bifurcation boundaries, one with the intersecting-enclosed state and one with the enclosed-intersecting state. All of these states are composed states. Now the double-nested state has an inner three-source nested state and and outer three-source nested state. The three-source nested state can bifurcate to the three-source intersecting state (as described in chapter 2.5), so if the inner nested part of the double-nested state bifurcates to an intersecting state, then the double-nested state becomes an enclosed-intersecting state.

Similarly, if the outer nested part of the double-nested state bifurcates to an intersecting state, then the double-nested state becomes an intersecting-enclosed state.

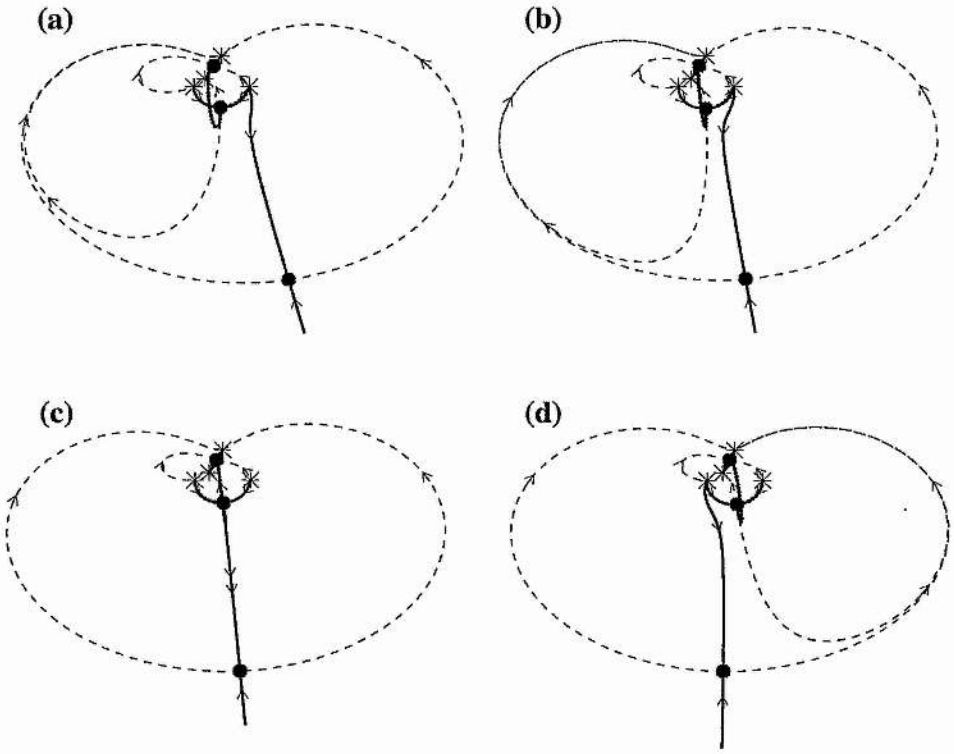

Figure 3.8: Field Line plots in the $z = 0$ plane showing the bifurcation from the enclosed-intersecting state to a reconfigured version of itself. In (a) and (b), the system approaches bifurcation, (c) shows the system at bifurcation and (d) shows the system after bifurcation.

However, there are still some bifurcation lines of interest to study. There are four regions which denote the enclosed-intersecting state. These regions can be split into two pairs of bordering regions, so the enclosed-intersecting state borders itself. This state does not have separate left and right variants, but it bifurcates into a reconfigured version of itself.

Figure 3.7 shows how the separatrix domes behave during bifurcation. In figure 3.7a and figure 3.7b, there is an inner separatrix dome which is formed by the 'separatrix wall' from the intersecting part of the state. This wall encloses one of the two sources which lie on the boundary of the intersecting part of the state. As the state is perturbed towards the bifurcation line, the inner separatrix dome expands to fill half of the outer

separatrix dome until at bifurcation (figure 3.7c) the inner dome coincides with half of the outer dome, and forms a separatrix wall dividing the outer dome into two halves.

After bifurcation (figure 3.7d), the inner separatrix dome reduces its size in the opposite half of the separatrix dome, now enclosing the other source which lies on the boundary of the intersecting part of the state.

Figure 3.8 shows this bifurcation in the $z = 0$ plane, figure 3.8a and figure 3.8b show the system as it approaches bifurcation and the inner separatrix dome expands until bifurcation (figure 3.8c) occurs and the inner separatrix dome then starts to shrink in the opposite half of the outer dome about the other source. This is a global spine-fan bifurcation which was studied for three sources in chapter 2.4.6.

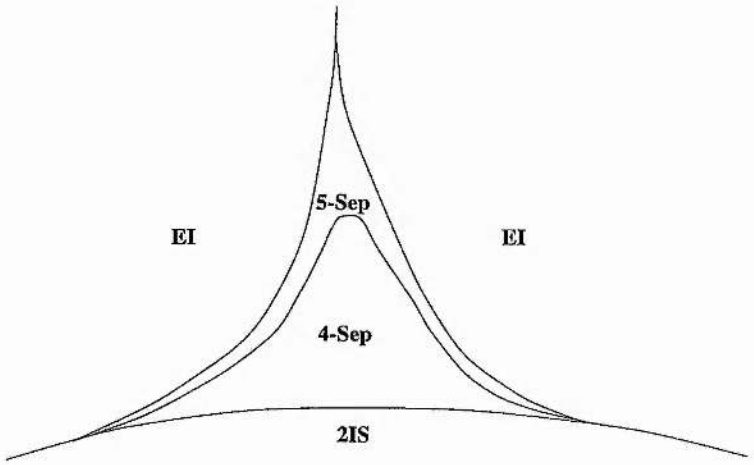

Figure 3.9: A sketch showing how the two topological regions are positioned in the multiple separator states.

In fact the global spine-fan bifurcation (chapter 2.4.6) and the global separator bifurcation (chapter 2.5.2) describe all of the bifurcation behaviour for this case except for one bifurcation line, separating the quintuple-separator state and the quadruple-separator state. These two topological regions are not resolved in figure 3.6 and are labelled the multi-separator (MS) states. A sketch showing how these two multi-separator state are positioned in the bifurcation diagram (figure 3.6) can be seen in figure 3.9.

Bifurcation into either of the multiple separator states from either the double-intersecting-

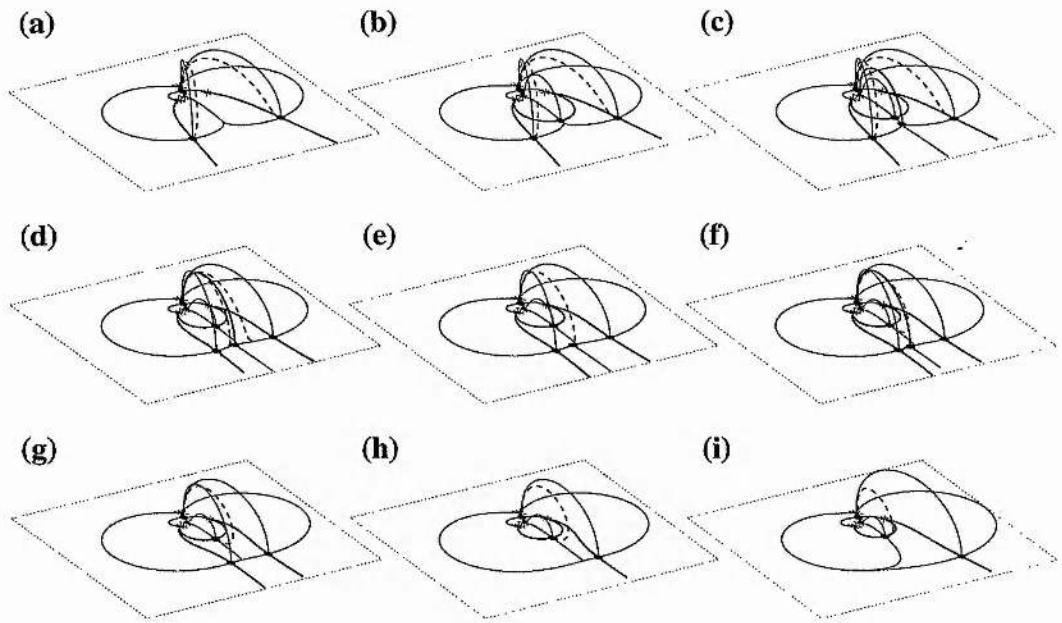

Figure 3.10: Three-dimensional field line plots which show that the double-intersecting-separate state (a) bifurcates with the appearance of a second-order null (b) which splits into two first-order nulls for the quintuple-separator state (c and d). The two separators coalesce (e) forming a single separator in a global separator-coalescence bifurcation for the quadruple-separator state (f). Two of the nulls then coalesce forming a second-order null (g) which is annihilated leaving the enclosed-intersecting state (h and i).

separate state or the enclosed-intersecting state is described by the local-separator bifurcation outlined in chapter 2.4.2. That is, when two separatrix domes (either separate domes or one dome enclosed within the other) approach one another and merge, a new second-order null point appears and splits into two first-order null points.

It is the bifurcation between the two multiple separator states that is interesting as the system must change from a state with two separators to a state with a single separator. This bifurcation process is shown in figure 3.10 and figure 3.11.

The system starts in the double-intersecting-separate state and evolves through the multiple separator states, ending up in the enclosed-intersecting state. The two separatrix domes of the double-intersecting-enclosed state approach one another (fig-

ure 3.10a) until they touch along a common separatrix surface, where a new second-order null appears (figure 3.10b). This new null then splits into two first-order nulls (figure 3.10c) in a local-separator bifurcation (chapter 2.4.2) and forms the quintuple-separator state.

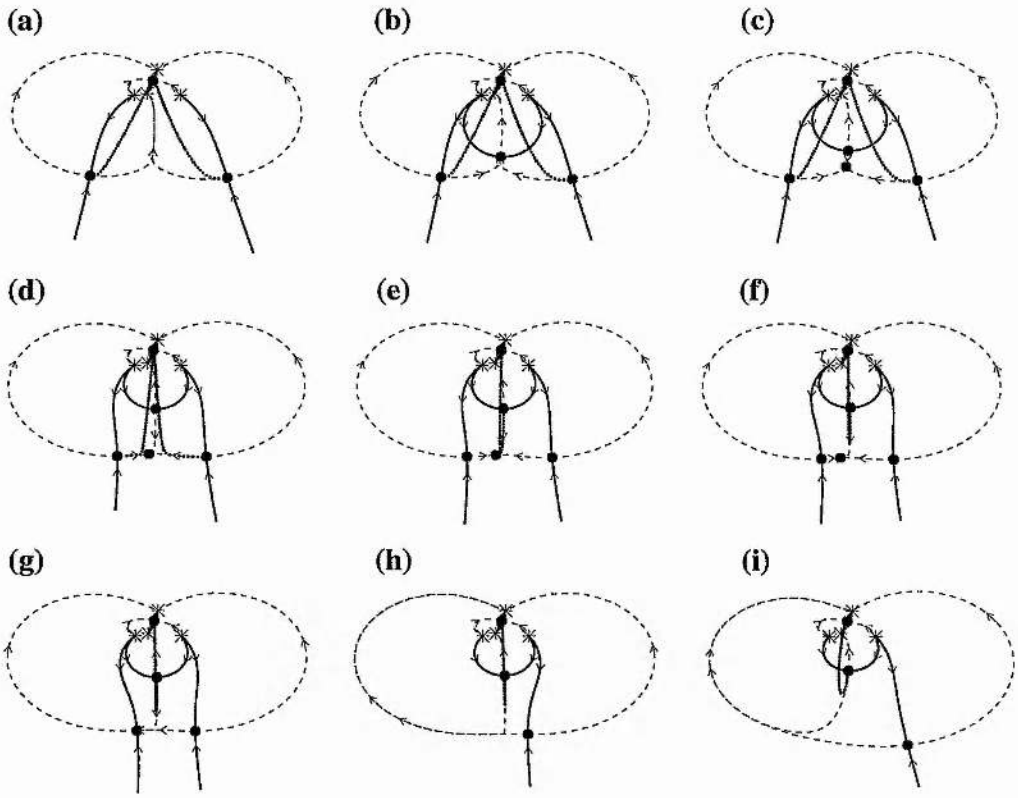

Figure 3.11: Field line plots in the $z = 0$ plane, which show how the double-intersecting-separate state (a) bifurcates with the appearance of a second-order null (b) which splits into two first-order nulls for the quintuple-separator state (c and d). The two separators coalesce (e) forming a single separator for the quadruple-separator state (f) in a global separator-coalescence bifurcation. Two of the nulls then coalesce forming a second-order null (g) which is annihilated leaving the enclosed-intersecting state (h and i).

As the system progresses, the two separators approach one another (figures 3.10c,d) and coalesce to a single separator which ends at one of the new first-order nulls (figure 3.10e). This separator then lifts away from this null and ends at the other new first-order null (figure 3.10f) forming the quadruple-separator state. This type of bifur-

cation is called *global separator-coalescence bifurcation* (Brown and Priest, 1999a).

The new first-order null which is not connected to the separator approaches one of the original nulls and they coalesce (figure 3.10g) and are annihilated in a local-separator bifurcation (chapter 2.4.2) leaving the system in the enclosed-intersecting state (figures 3.10h,i).

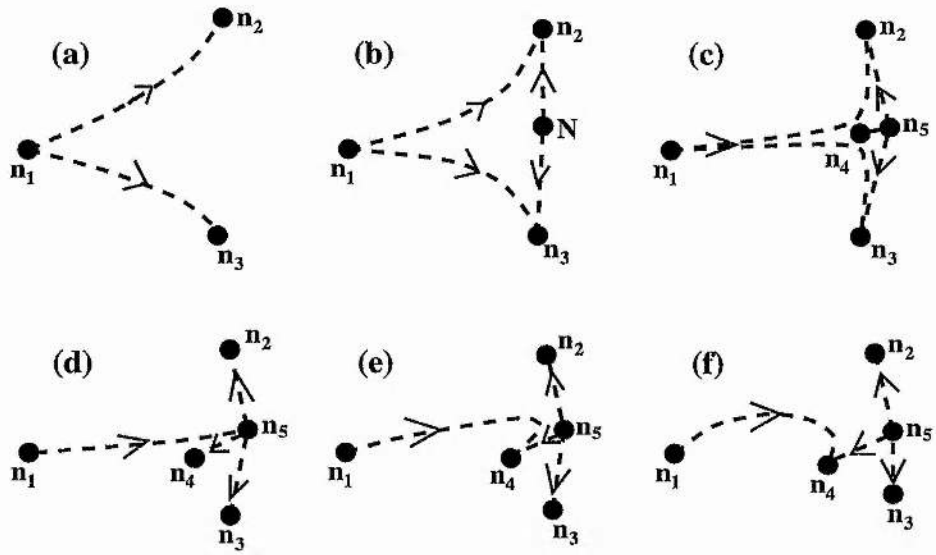

Figure 3.12: Representation of the merging of two separators. As the two separators joining **n1** with **n2** and **n1** with **n3** (a) close together a new second order null, **N**, appears (b), which splits into two first-order nulls **n4** and **n5** (c), the null **n5** has three separators which join **n5** with **n2**, **n3** and **n4**. The two separators merge joining **n1** with **n5**, with the end segments of the two separators merging with the separators joining **n5** with **n2** and **n5** with **n3**, respectively (d). This is unstable and the separator joining **n1** with **n5** moves away from **n5** with the end segment separating from the separator joining **n4** with **n5** (e and f), producing a separator which connects **n1** with **n4**.

An important consideration for separator-coalescence bifurcation is the null at which they meet. This null has its fan in the $z = 0$ plane. Figures 3.11c,d,e and f show that three of the fan field lines emanating from this null start at other nulls, so strictly speaking these three field lines are separators as they each connect to null points. So, as the two separators merge (figures 3.11d,e) and meet at the central null with its fan in

the $z = 0$ plane, the sections of the two separators that lead on to the outer nulls merge with the separators in the $z = 0$ plane which join the central null with the outer nulls. Similarly, when the single separator lifts away from the central null, it also splits from the separator connecting the central null to the remaining first-order null. This process is shown in terms of the separator behaviour in figure 3.12.

3.3.3 Two positive and two negative sources with positive total flux

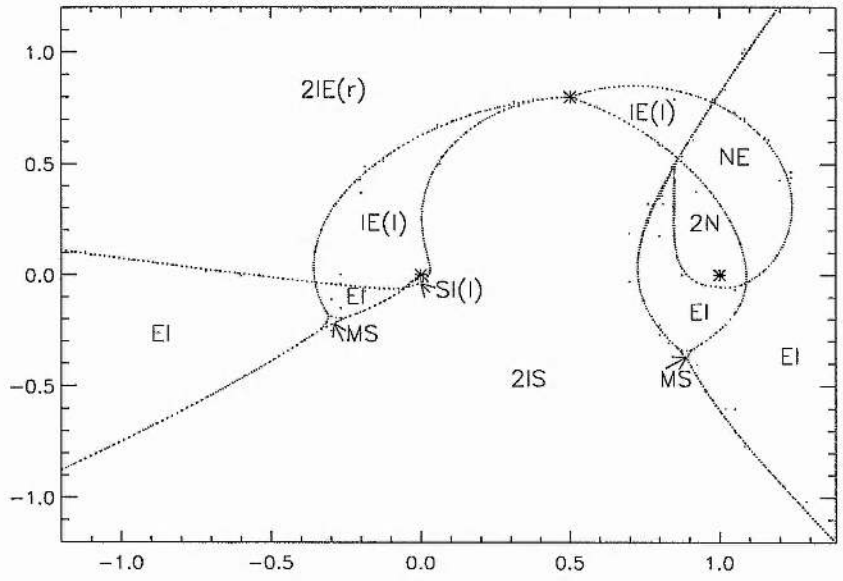

Figure 3.13: Bifurcation diagram showing the regions where a fourth source of strength -0.8 can be placed, with respect to three sources of strengths 1, 0.5 and -0.5 located at (0,0), (1,0) and (0.5,0.8), to obtain the various topological states. (2IS) Double-Intersecting-Separate state, (2IE) Double-Intersecting-Enclosed state (l or r indicate left or right handed version), (IE) Intersecting-Enclosed state, (EI) Enclosed-Intersecting state, (NE) Nested-Enclosed state, (2N) Double-Nested state, (SI) Separate-Intersecting state and (MS) Multi-Separator states.

Consider the case outlined in chapter 3.3.1 when a fourth sources of strength -0.8 is added. This makes the total flux positive and displays much the same bifurcation

behaviour (figure3.13) as the case when the total flux is negative. That is to say, the same topological states occur and most of the bifurcation lines seen in figure 4bif2 have equivalent bifurcation lines in the previous case (see figure 3.6).

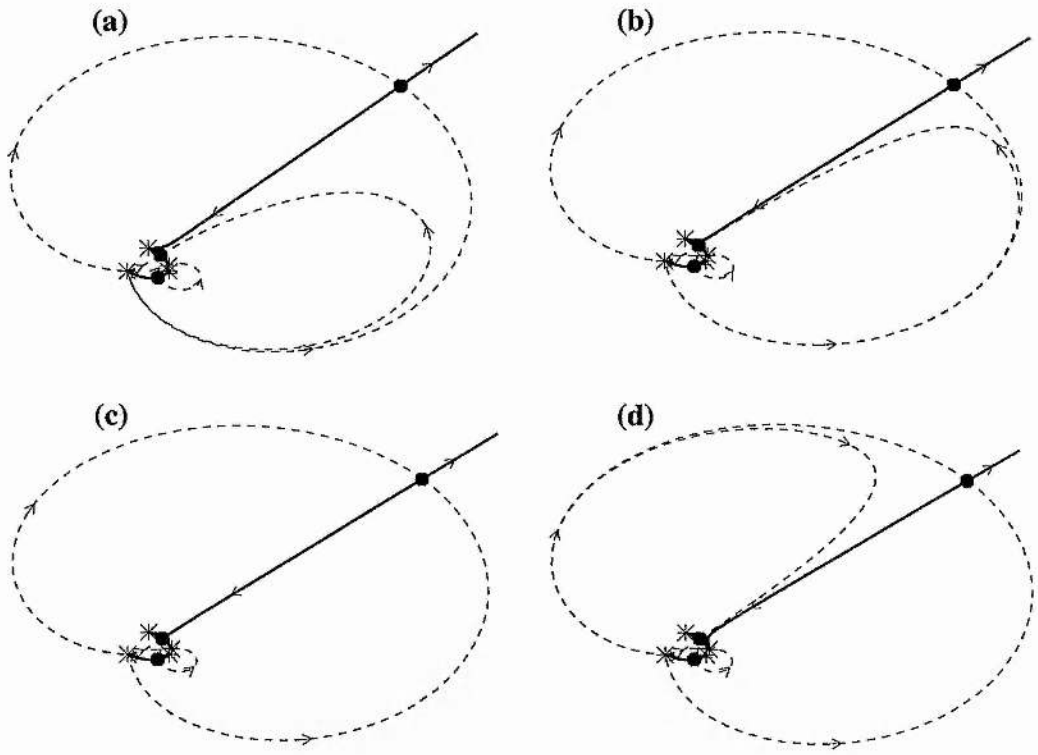

Figure 3.14: Field line plots in the plane $z = 0$ showing the bifurcation from the double-nested state (a,b) through bifurcation (c) to the nested-enclosed state (d).

In fact there is only one new type of bifurcation line that was not seen in the previous case, and that is the one which separates the double-nested state and the nested-enclosed state. This bifurcation is a global spine-fan bifurcation (chapter 2.4.6) and is much the same as the bifurcation from the enclosed-intersecting state to a reconfigured version of itself (see figures 3.7, 3.8).

Starting off in the double-nested state (figure 3.14a), as the system approaches bifurcation the middle separatrix dome expands (figure 3.14b) until it fills half of the outer separatrix dome and portions of the two separatrix domes merge (figure 3.14c). This is the bifurcation point and the spine of the outer separatrix dome intersects with the

fan of the middle separatrix dome. After bifurcation, the 'middle' separatrix dome splits from the other half of the outer separatrix dome, except that now the middle dome does not contain the inner separatrix dome of the double-nested state. This is the nested-enclosed state (figure 3.14d).

3.3.4 Three positive and one negative sources

The final case to consider when adding a fourth source to the system is the case when the fourth source is positive. So consider the effect of adding a fourth source of strength 0.3 to the system with sources located on the $z = 0$ plane at $(0, 0)$, $(1, 0)$ and $(0.5, 0.8)$ with strengths 1, 0.5 and -0.5, respectively.

This regime generates six new topological states, which are plotted in figure 3.15. These states are;

Divided-Intersecting (DI) state

This state is a composition of the three-source divided state and intersecting state. It is essentially an intersecting state with a separatrix wall nearby. The null point in the separatrix wall is connected to one of the sources of the intersecting state by a spine field line. There is a single separator. As there are two possible sources that the spine of the separatrix wall could connect to, this state has both left and right handed variants.

Double-Intersecting-Divided (2ID) state

This state comprises a separatrix dome intersected by two separatrix walls, causing there to be two separators. The two separatrix walls meet at a null point at the edge of the separatrix dome and intersect along its spine field line, dividing the three regions of connectivity, in the separatrix dome, like segments of an orange.

Triangular-Intersecting (TI) state

This state is a composition of the three-source triangular and intersecting states, with each 'state' sharing two common sources and one common null, and the two three-source state lying 'back to back'. The state has five nulls rather than the usual three,

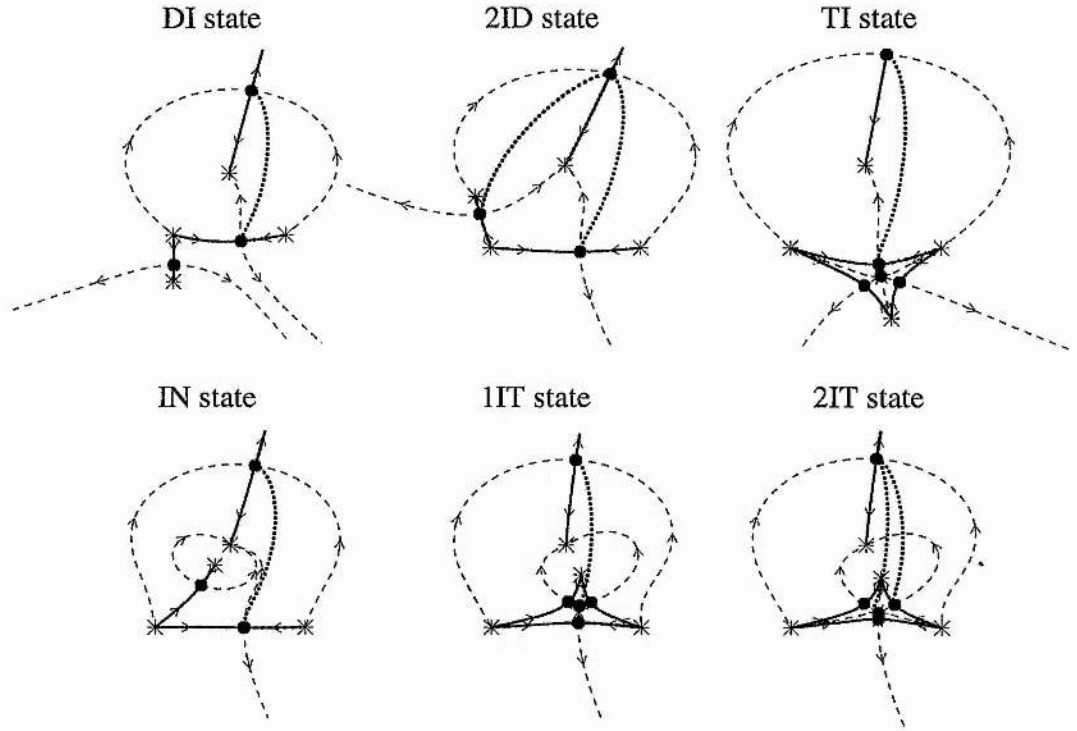

Figure 3.15: Some topological states possible with three positive sources and one negative source, plotted in the $z = 0$ plane. The asterisks represent the sources and the dots are null points. The bold lines represent the spine field lines and the dashed curves are fan field lines. Dotted lines are the projections of the separators in the $z = 0$ plane. The topological states are; (DI) Divided-Intersecting State, (2ID) Double-intersecting-Divided State, (TI) Triangular-Intersecting State, (IN) Intersecting-Nested State, (1IT) Single-Intersecting-Triangular state and (2IT) Double-Intersecting-Triangular state.

One of these has three separators in the $z = 0$ plane which connect to three separate nearby nulls. One of these nulls also has a separator, not in the $z = 0$ plane, which connects to the remaining null point.

Intersecting-Nested (IN) state

This state is a three-source intersecting state with a separatrix dome nested inside, with a single separator in the nested part of the state. As the intersecting part has its separatrix dome divided by a separatrix wall, the nested dome can be on either side of the wall, thus giving rise to both a left-handed and right-handed variant of this state.

Single-Intersecting-Triangular (1IT) state

This state comprises a three-source triangular part and a three-source intersecting part like the triangular-intersecting state, except that the triangular part of the state lies inside the separatrix dome of the intersecting part. The centre null of the triangular part of the state has three separators in the $z = 0$ plane which connect to the other three nulls in the triangular part. The outermost null of the triangular part is shared with the intersecting part of the state, and has a separator connecting it to the remaining null.

Double-Intersecting-Triangular (2IT) state

This state is very similar to the single-intersecting-triangular state except that instead of a single separator, there are two separators. The central null of the triangular part is still connected by three separators in the $z = 0$ plane to the other three nulls in the triangular part, but now, instead of the innermost null, the two nulls that did not have other separators are connected to the remaining null in the intersecting part.

Bifurcation behaviour

Much of the bifurcation behaviour displayed by this system has already been analysed in either the three-source case or in the previous four-source cases. For example, bifurcation from the left-handed divided-intersecting state to the right-handed divided-intersecting state is the same as bifurcation between the two variants of the three-source divided state (chapter 2.6). The intersecting-nested state bifurcates to the double-intersecting-divided state when the nested portion of the intersecting-nested state interacts with the outer dome of the state and a global separator bifurcation (chapter 2.5.2) occurs in the same way as when the three-source nested state bifurcates to the three-source intersecting state.

Bifurcation from the double-intersecting-divided state through the double-intersecting-triangular state to the single-intersecting-triangular state and finishing as one of the intersecting-nested states, is much the same as the bifurcation through the multiple separator states in the case with two positive and two negative sources (chapter 3.3.2).

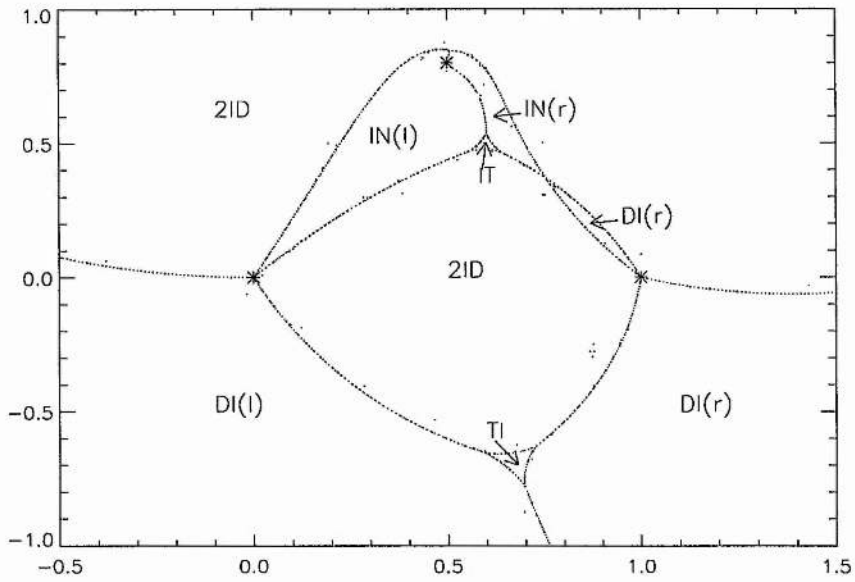

Figure 3.16: Bifurcation diagram showing the regions where a fourth source of strength 0.3 can be placed, with respect to three sources of strengths 1, 0.5 and -0.5 located at (0,0), (1,0) and (0.5,0.8), to obtain the various topological states. (DI) Divided-Intersecting State, (2ID) Double-intersecting-Divided State, (TI) Triangular-Intersecting State, (IN) Intersecting-Nested State, (IT) Intersecting-Triangular States (this last state is actually two states, the Single-Intersecting-Triangular state and the Double-Intersecting-Triangular state). Where l or r indicates left or right handed versions.

However, there is some behaviour to investigate. For example, bifurcation from the double-intersecting-divided state into the triangular-intersecting state is slightly similar to bifurcation between the multiple separator states (chapter 3.3.2), but has a subtle difference.

The two separators in the double-intersecting-divided state (figures 3.17a,b) approach one another and at bifurcation they coalesce (figure 3.17c) at a newly formed second-order null which splits into two first-order nulls forming the triangular-intersecting state (figure 3.17d).

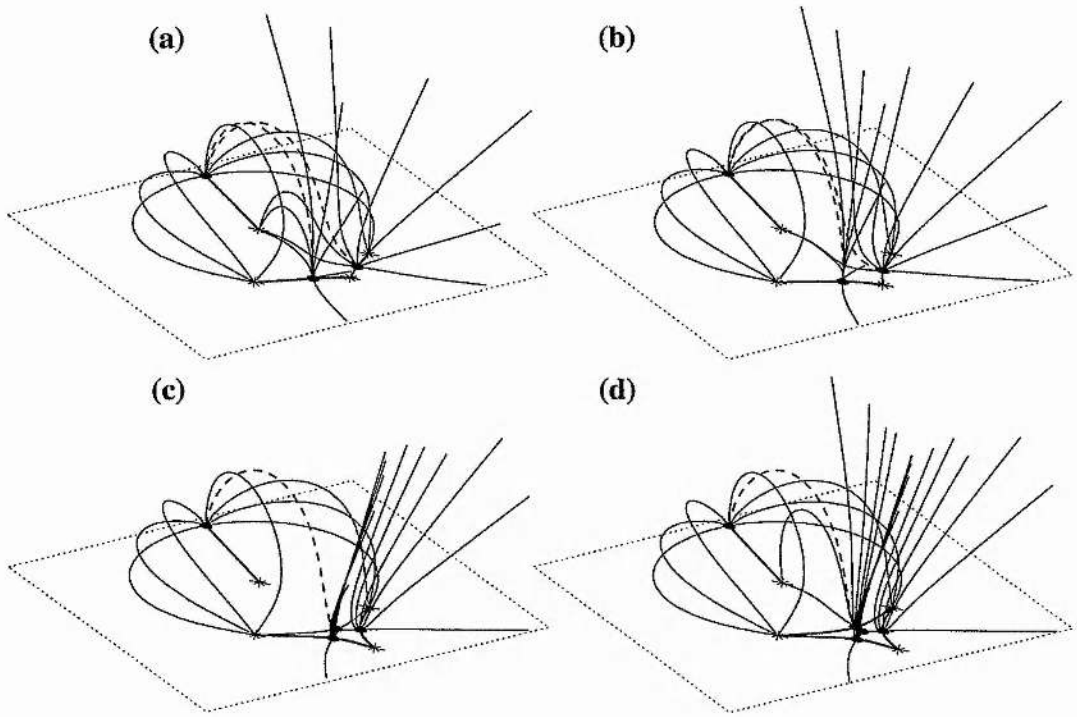

Figure 3.17: Three-dimensional field line plots showing the bifurcation from the double-intersecting-divided state (a,b) through bifurcation (c) where the separators merge and a new second-order null appears, which splits into two first-order nulls forming the triangular-intersecting state (d).

These separators only coalesce along a portion of their length. When the two separators merge the second-order null appears at the end of this portion, leaving the ends of the two separators to connect this new null with the two nulls to which the separators were originally connected (figure 3.18c). These two separator connections lie in the $z = 0$ plane, and, when the second-order null splits, a third separator will join the two new nulls (figure 3.18d), so that one of the new nulls will have three separators in the $z = 0$ plane which connect to the three nearby nulls (which includes the second new null). The other new null will be connected to the remaining null by the separator out of the plane. This is the triangular part of the state. So in this case, the moment when the separators coalesce coincides with the moment that the second-order null appears. This is called a *local separator-coalescence bifurcation.*

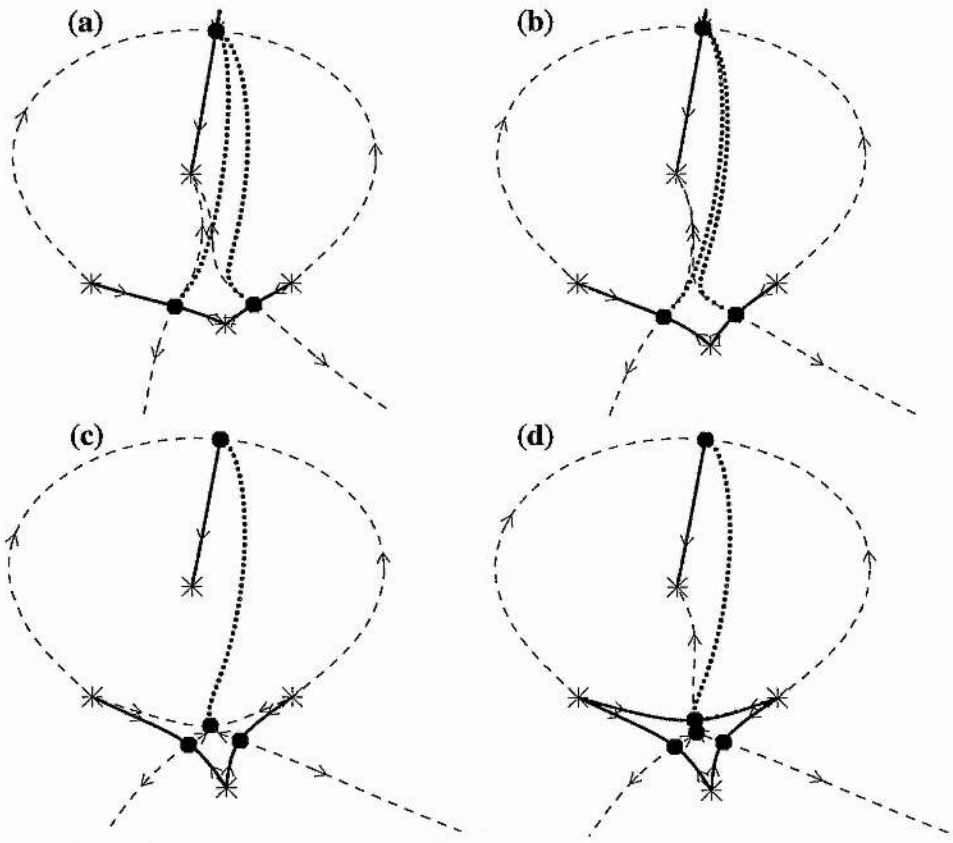

Figure 3.18: Field Line plots in the plane $z = 0$ showing the bifurcation from the double-intersecting-divided state (a,b) through bifurcation (c) where the separators merge and a new second-order null appears. This then splits into two first-order nulls forming the triangular-intersecting state (d).

3.3.5 Summary of separators

This section has focussed on separators and has shown that they are interesting and rich in topological behaviour. They occur in many different topological situations and can be involved in a variety of bifurcations. In particular, it has been demonstrated how two neighbouring separators can interact and merge into a single separator.

Separators have an important role in magnetic reconnection (Priest and Titov, 1996), current sheets can form along them (Longcope and Cowley, 1996) and reconnection is likely to be concentrated near them. Thus, it is important to have a good understanding

of their topological behaviour, such as when they occur and how they interact with other magnetic structures.

3.4 Null Points out of the z = 0 Plane

3.4.1 Analytical example

So far in chapter 2 and chapter 3 all of the stable topological states have had their null points lying in the $z = 0$ plane. This is not always the case, however, and it is possible for null points to lift off from the $z = 0$ plane.

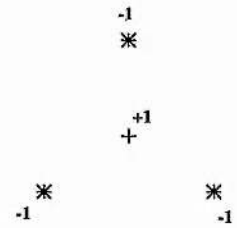

Figure 3.19: Diagram showing a possible configuration of sources to produce a null point out of the plane.

Consider the case where there are three sources of equal strength, $\epsilon_s = -1$, positioned equidistant from each other in an triangular formation. Now place a positive source of unit strength in the centre of the triangular formation. This configuration is shown in figure 3.19. The magnetic field is given by

$$\mathbf{B}_x(x,y,z) = \frac{x}{(x^2+y^2+z^2)^{3/2}} - \frac{x-\cos\pi/6}{((x-\cos\pi/6)^2+(y+\sin\pi/6)^2+z^2)^{3/2}} - \frac{x+\cos\pi/6}{((x+\cos\pi/6)^2+(y+\sin\pi/6)^2+z^2)^{3/2}} - \frac{x}{(x^2+(y-1)^2+z^2)^{3/2}} \tag{3.1}$$

$$\mathbf{B}_y(x,y,z) = \frac{y}{(x^2+y^2+z^2)^{3/2}} - \frac{y+\sin\pi/6}{((x-\cos\pi/6)^2+(y+\sin\pi/6)^2+z^2)^{3/2}} - \frac{y+\sin\pi/6}{((x+\cos\pi/6)^2+(y+\sin\pi/6)^2+z^2)^{3/2}} - \frac{y-1}{(x^2+(y-1)^2+z^2)^{3/2}} \tag{3.2}$$

$$\mathbf{B}_z(x,y,z) = \frac{z}{(x^2+y^2+z^2)^{3/2}} - \frac{z}{((x-\cos\pi/6)^2+(y+\sin\pi/6)^2+z^2)^{3/2}} - \frac{z}{((x+\cos\pi/6)^2+(y+\sin\pi/6)^2+z^2)^{3/2}} - \frac{z}{(x^2+(y-1)^2+z^2)^{3/2}} \tag{3.3}$$

Where $\mathbf{B}_x$, $\mathbf{B}_y$ and $\mathbf{B}_z$ are the components of the magnetic field in Cartesian geometry. By symmetry, it is clear that there is a null point lying on the y-axis (ie $x = 0$ and $z = 0$). Along this line $\mathbf{B}_x = \mathbf{B}_z = 0$ and equation 3.2 becomes

$$\mathbf{B}_y(0,y,0) = \frac{y}{|y|^3} - \frac{2y+1}{(y^2+y+1)^{3/2}} - \frac{y-1}{|y-1|^3}, \tag{3.4}$$

which has a solution of $y \approx -0.91$. By rotational symmetry there are two further nulls at a distance ≈ -0.91 from the origin, along the lines $y = x\cos\pi/6$ and $y = x\cos 5\pi/6$.

But this does not account for all of the nulls. When $x = y = 0$ and only $z \geq 0$ is considered then $\mathbf{B}_x = \mathbf{B}_y = 0$, and equation 3.3 becomes

$$\mathbf{B}_z(0,0,z) = \frac{1}{z^2} - \frac{3z}{(1+z^2)^{3/2}}, \tag{3.5}$$

which has a null point satisfying

$$8z^6 - 3z^4 - 3z^2 - 1 = 0. \tag{3.6}$$

This gives $z \approx 0.962$.

This topology can be seen in figure 3.20. There are three separatrix walls which meet at the spine of the null out of the plane. This spine is connected to the central positive source. Each of the separatrix walls includes one of the null points which lie in the $z = 0$ plane. Around the central positive source there is a separatrix dome which

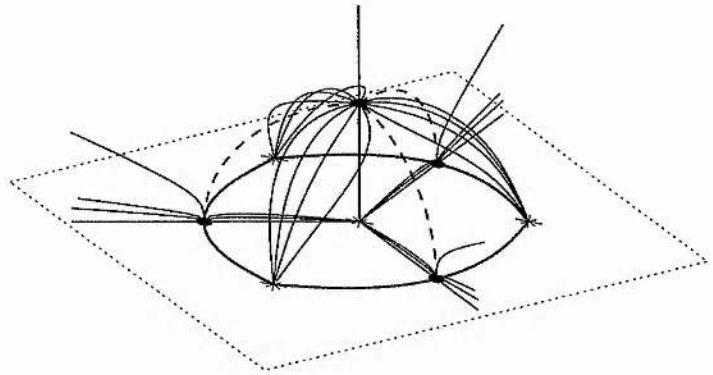

Figure 3.20: Three-dimensional field line plot showing the topological state which has a null out of the $z = 0$ plane. The solid lines show the fan field lines, the thick lines show the spine field lines, the dashed lines represent separators, the asterisks are sources and the dots are null points.

includes the remaining three sources and all of the nulls. Where the three separatrix walls intersect the separatrix dome there are separators. These separators meet at the null out of the plane and connect it to each of the three nulls in the $z = 0$ plane. The null point which lies out of the plane marks the point where all three of the separatrix walls and the separatrix dome meet.

3.4.2 Varying the source strengths

Suppose now that the central positive source has a strength of ϵ. The position of the null point out of the plane is then given by;

$$\mathbf{B}_z(0,0,z) = \frac{\epsilon}{z^2} - \frac{3z}{(1+z^2)^{3/2}} = 0, \tag{3.7}$$

which can be rearranged to give

$$z = \pm \frac{1}{\left(\left(\frac{3}{\epsilon}\right)^{2/3} - 1\right)^{1/2}}. \tag{3.8}$$

This has the property that $z \longrightarrow \infty$ as $\epsilon \longrightarrow 3$ from below. So as the sum of the sources tends to zero the null point out of the $z = 0$ plane tends to infinity. As ϵ passes

through 3 some of the field lines beginning at the positive source change from being closed to open field lines.

3.4.3 Bifurcation behaviour

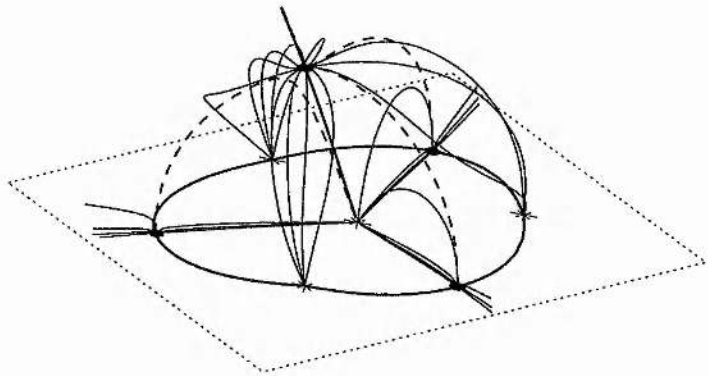

Figure 3.21: Three-dimensional field line plot showing an asymmetric topological state generated by sources at $(0,0)$, $(0,1)$, $(-0.7,-0.6)$ and $(0.9,-0.4)$ with respective strengths 1.5, -0.9, -0.8 and -1.1 and a null out of the $z=0$ plane. The solid lines show the fan field lines, the thick lines show the spine field lines, the dashed lines represent separators, the asterisks are sources and the dots are null points.

It is possible to calculate these null points analytically due to the high symmetry of the system outlined. The problem with symmetric systems is that many such examples can represent topologically unstable non-generic behaviour, which is why symmetric configurations have largely been overlooked in this thesis. However, the topology of this configuration, with its null out of the plane, does continue when the system is perturbed and the symmetry is broken. An example of this is given in figure 3.21.

Figure 3.22 shows where the topological state with a null out of the plane (henceforth referred to as the Coronal-Null state or CN state) exists in parameter space. The configuration of sources in figure 3.21 is used with the position of the positive source being varied. The coronal-null state can only bifurcate into the double-intersecting-detached state which has been discussed in section 3.3.4.

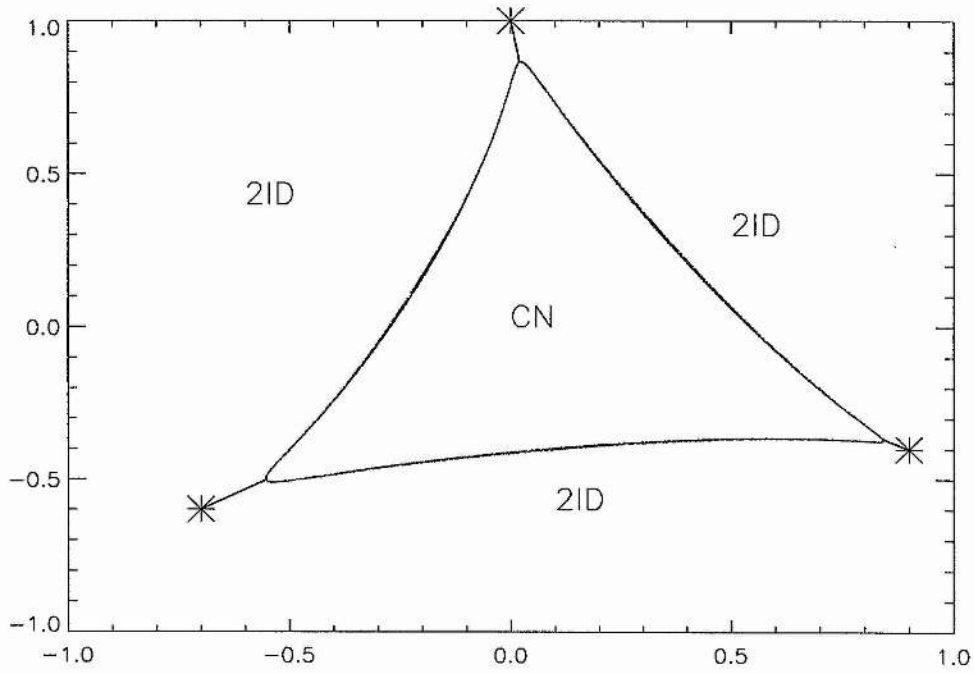

Figure 3.22: Bifurcation diagram showing the region in parameter space where there is a null point out of the plane. The fixed sources are located at $(0, 1)$, $(-0.7, -0.6)$ and $(0.9, -0.4)$ with strengths -0.9, -0.8 and -1.1, the varying source has strength 1.5. The topological states are (CN) coronal-null state, (2ID) double-intersecting-detached state.

To understand how this bifurcation occurs, the behaviour of the null points must be analysed. The paths of the null points as the positive source is moved is shown in figure 3.23. The initial configuration is that in figure 3.21 and, as the positive source is moved along the dashed line, the nulls move along the solid lines.

The null which is out of the $z = 0$ plane can be seen to approach the plane and merge with one of the null points already in the plane. This behaviour does not make sense at first, but it must be remembered that although the region below the $z = 0$ plane is being ignored for physical reasons, it still exists mathematically. The behaviour below the $z = 0$ plane is the mirror of the behaviour above the plane, so there is also a null

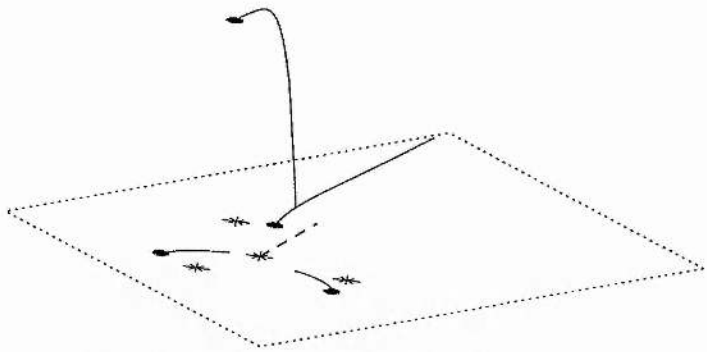

Figure 3.23: Plot showing the evolution of the null points as the topology bifurcates between the coronal-null state and the double-intersecting-detached state. The large dots indicate the initial position of the nulls. The path of the varying source is indicated by a dashed line.

point below the plane which approaches the plane and merges with the same null in the plane.

So the three nulls merge to form a third-order null point at the moment of bifurcation. Two of the solutions then become complex, in the same way as when a second-order null is annihilated, and the null becomes a first-order null (part of the double-intersecting-detached state). This is a three-dimensional version of a pitchfork bifurcation and is called a *local double-separator bifurcation.*

Thus, pitchfork type bifurcation can happen between stable four-source states, where it, previously, only occurred between unstable three-source states (Priest et al., 1997).

3.4.4 Analytical model for local double-separator bifurcation

An analytical model for the magnetic field of this process is described by the equation

$$\mathbf{B}(\mathbf{r}) = \begin{pmatrix} -x\left(3z^2 + \lambda + a\right) \\ (2\lambda + a)y \\ z\left(z^2 - \lambda\right) \end{pmatrix}, \tag{3.9}$$

where λ is the parameter to be varied and a is a constant which is fixed so that $\lambda+a > 0$ and $2\lambda + a > 0$ near the bifurcation point.

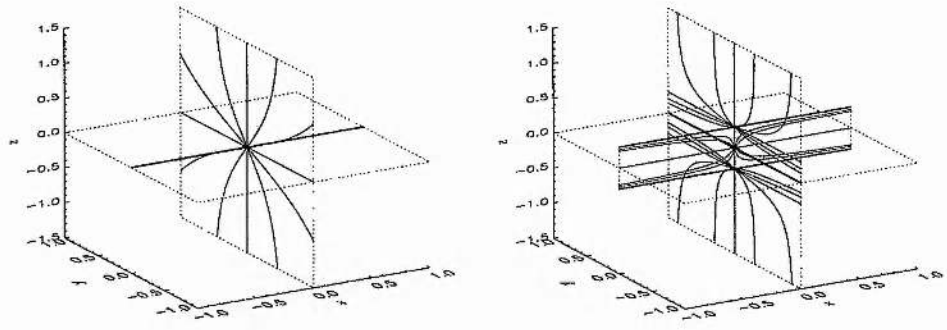

Figure 3.24: Plots illustrating a pitchfork bifurcation. The field initially has one null point with a separatrix surface. At bifurcation this null becomes a third-order null and splits into three first-order nulls. This generates three separatrix surfaces.

Equation 3.9 has null points where $x = y = 0$ and $z = 0$ or $z = \pm\sqrt{\lambda}$. When $\lambda < 0$ the system has two complex roots and the only physical null point is at $(0, 0, 0)$. When $\lambda = 0$ the system has a triple root at $(0, 0, 0)$ which is a third-order null point. As λ increases, the third-order null splits into three first-order nulls. This can be seen in figure 3.24.

Before bifurcation the single null point has an associated separatrix surface. At bifurcation, this actually becomes two surfaces which meet along the line $x = z = 0$. As the nulls split, a new separatrix surface is formed between the spines of the two nulls that leave the $z = 0$ plane (figure 3.24). This surface is perpendicular to the other two separatrix surfaces.

3.4.5 Summary of nulls out of the plane

This section has demonstrated a source configuration which leads to a null point arising in the corona. It has also demonstrated how they can initially bifurcate out of or back into the $z = 0$ plane and how varying the flux can cause the null point to extend to

infinity.

This flux emergence is a possible mechanism for solar flares and the idea of topological triggers for eruptions has been previously suggested by Bungey (1995); Lau (1993); Gorbachev et al. (1988). The flux configuration of a magnetic fragment being surrounded by fragments of opposite polarity has been observed by Antiochos (1998); Aulanier et al. (1998) in photospheric magnetograms. The three separators in the topological configuration are good sites for excess heating (section 3.3.5).

3.5 Conclusions and discussion

This chapter has discussed several four-source cases, identifying new topological states and their location in parameter space, as well as the bifurcations that occur when topological states change.

Much of this has underlined the versatility of the three-source behaviour, and how it generalises to higher-order cases. However, new behaviour which is not seen in the three-source case, such as the interaction between two separators, now manifests itself in the four-source case. This behaviour will, in turn, be present in higher order cases.

Separators are important magnetic features as they are the intersection between two separatrix surfaces. This means that they will often play an important role when two magnetic structures interact. Also, their role in magnetic reconnection could be more important than has previously been thought (Longcope and Cowley, 1996). One reason for this is simply that instead of just one null point through which its associated fan surface and spine field lines can reconnect, there are now two whose behaviour is interlinked.

Topological behaviour can also be used to explain coronal phenomena. A preliminary model for solar flares and eruptions due to flux emergence has been suggested. There are other possibilities. Polar plumes are good candidates for topological modeling and the magnetic topology of a coronal brightening will be discussed in chapter 4.

To be able to understand coronal phenomena, an understanding of the magnetic topology in the corona is important. As the solar magnetic field is extremely complex, it is vital to study the small-scale fields that have been encountered in this chapter and the previous one, in order to be able to comprehend the global field and events that occur in it.

Chapter 4

The Magnetic Structure of a Solar Coronal Bright Point

4.1 Introduction

X-ray bright points were first described as "small concentrated point-like features" by Vaiana et al. (1970) during a study of x-ray images of the quiescent solar corona taken during an Aerobee rocket flight in 1969.

Golub et al. (1974) determined the properties of x-ray bright points from a study of Skylab x-ray images. The lifetime of bright points is, on average, about 8 hours long and their area is typically of the order $2 \times 10^8 km^2$. The maximum area of a bright point is proportional to its lifetime. The bright point starts out as an diffuse cloud which is followed by the growth of a bright core, with an area of the order $10^7 km^2$.

It is estimated that as many as 1500 bright points can emerge each day. They are not concentrated in active region belts, but are spread over the surface of the Sun. A second class of longer-lived bright points are thought to exist nearer the equator (Golub et al., 1976a), with an average lifetime of about 36 hours.

The average temperature of a bright point falls into the range $1.3 - 1.7 \times 10^6 K$ and the

density is typically $2-4$ times higher than the coronal average, which is of the order $5 \times 10^{14} m^{-3}$ (Golub et al., 1974). 5-10% of bright points also show rapid brightening which is consistent with small flares. Yohkoh observations suggest that bright points fluctuate in intensity by 30-200% over time-scales of a few minutes to hours (Priest et al., 1994).

Skylab observations suggested that bright points have a size of about $20Mm$, but in the 1990's NIXT (which had a higher resolution and lower scatter than Skylab) observed complex loop structure in bright points with a size of the order $9Mm$ (Parnell et al., 1994; Parnell, 1994).

A bright point is associated with small bi-polar magnetic features in the photosphere which have a typical total flux of $10^{19} - 10^{20} Mx$ (Golub et al., 1976b). One third of bright points lie over ephemeral regions, which are newly emerging regions of magnetic flux, whereas the remaining two thirds lie above *cancelling magnetic features*, which consist of opposing polarity fragments that approach one another and disappear. This led Priest et al. (1994) to propose a converging flux model where the approaching flux regions of a bi-pole cause a null point to rise out of the photosphere. The bright point is then powered by energy from reconnection at this null point.

More recently, bright points have been observed by the EIT instrument on SOHO and then, in 1998, TRACE enabled both high temporal and spatial observations of bright points to be made. Traditionally, the name x-ray bright point has been used, but, both EIT and TRACE image the corona in extreme ultraviolet light. For this reason, this thesis will use the term *coronal bright points* for this phenomena.

4.2 Bright Point Observations from TRACE

From 13th-17th June 1998, TRACE and SOHO/MDI simultaneously observed the same quiet region of the Sun. From these observations the fascinating and complex structure of coronal bright points, intense small-scale brightenings that occur through-

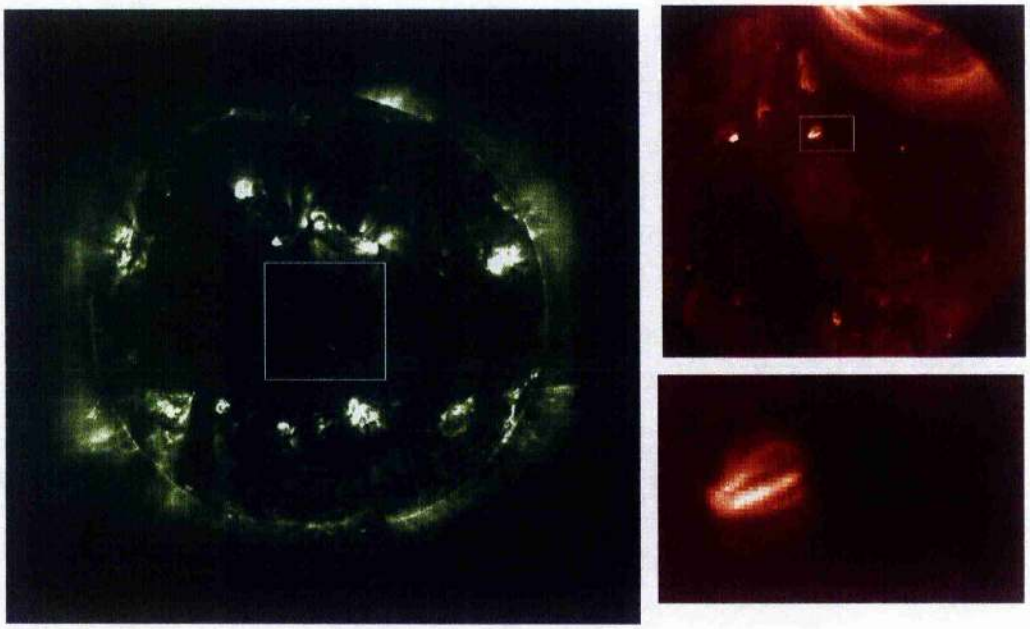

Figure 4.1: EIT image (left) of the Sun at 07:15 on 14th June 1998 showing the region which TRACE was observing (right top) which in turn shows the clipping region of the bright point (right bottom).

out the solar corona, can be seen in great detail (Brown et al., 1999).

For the first time, it has been possible to study bright points for their entire lifetime with a cadence of less than 2 minutes and a temporal resolution of up to 0.5 arcseconds. One particular bright point, which lasted for about a day, exhibited dynamic structural behaviour which became increasingly complex and led to its sudden eruptive demise.

The bright point studied in this chapter was extracted from this quiet Sun TRACE observation sequence and is completely contained within the MDI high-resolution field of view, passing approximately 60 arcseconds above disk centre. The region extracted is 75 arcseconds by 50 arcseconds and runs over a period of about 24 hours. Figure 4.1 shows an EIT image which indicates the region of the Sun which TRACE was observing and a TRACE image from which the bright point region was clipped. Due to rotation of the Sun, the bright point actually moves across the image from left to right, so the clipping region is moved accordingly.

Image cubes from the Fe IX (figure 4.2) and Fe XII (figure 4.3) lines of TRACE and

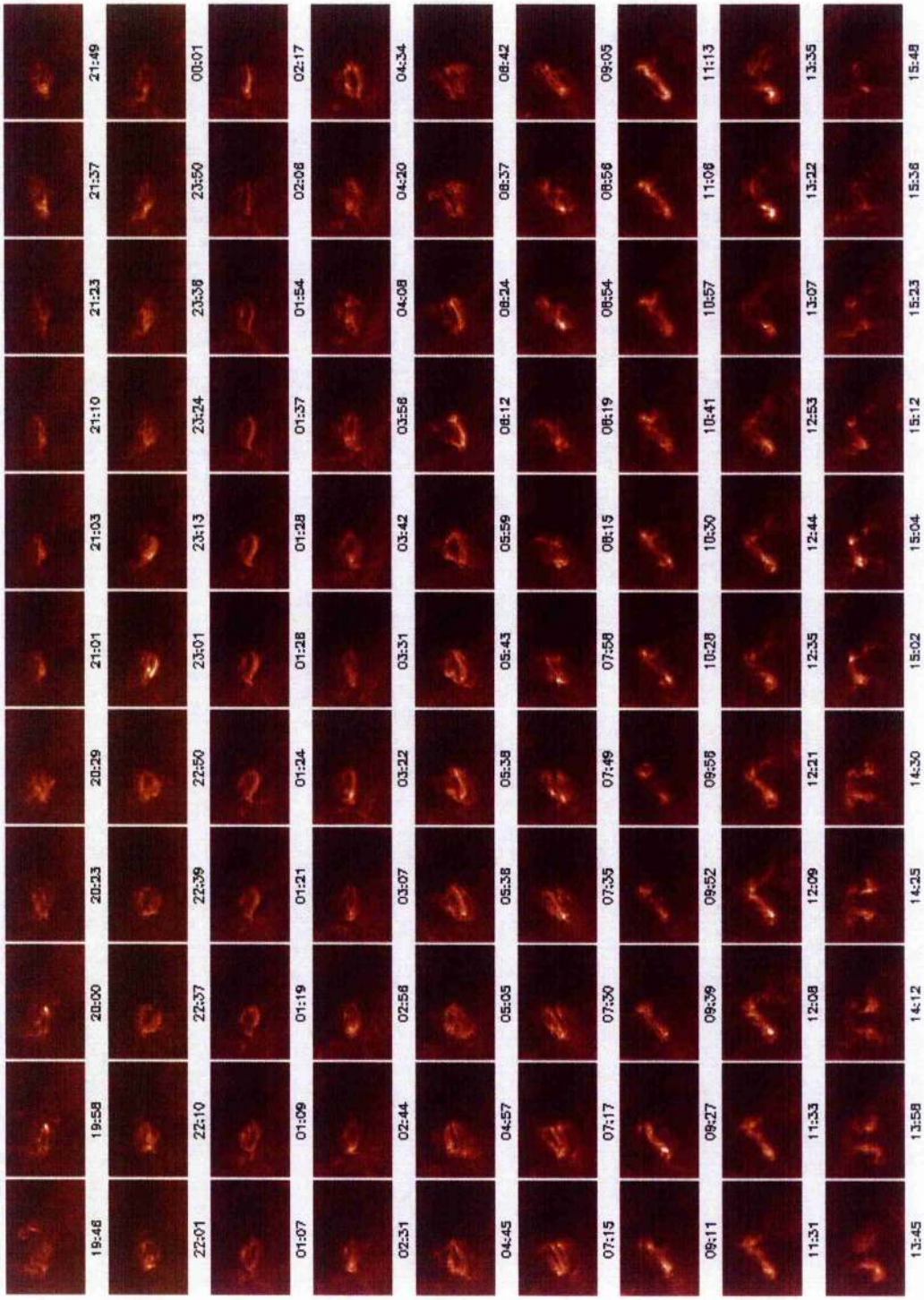

Figure 4.2: Evolution of a coronal bright point observed in Fe IX by TRACE on the 13th and 14th June 1998. Each frame is 75×50 arcseconds^2.

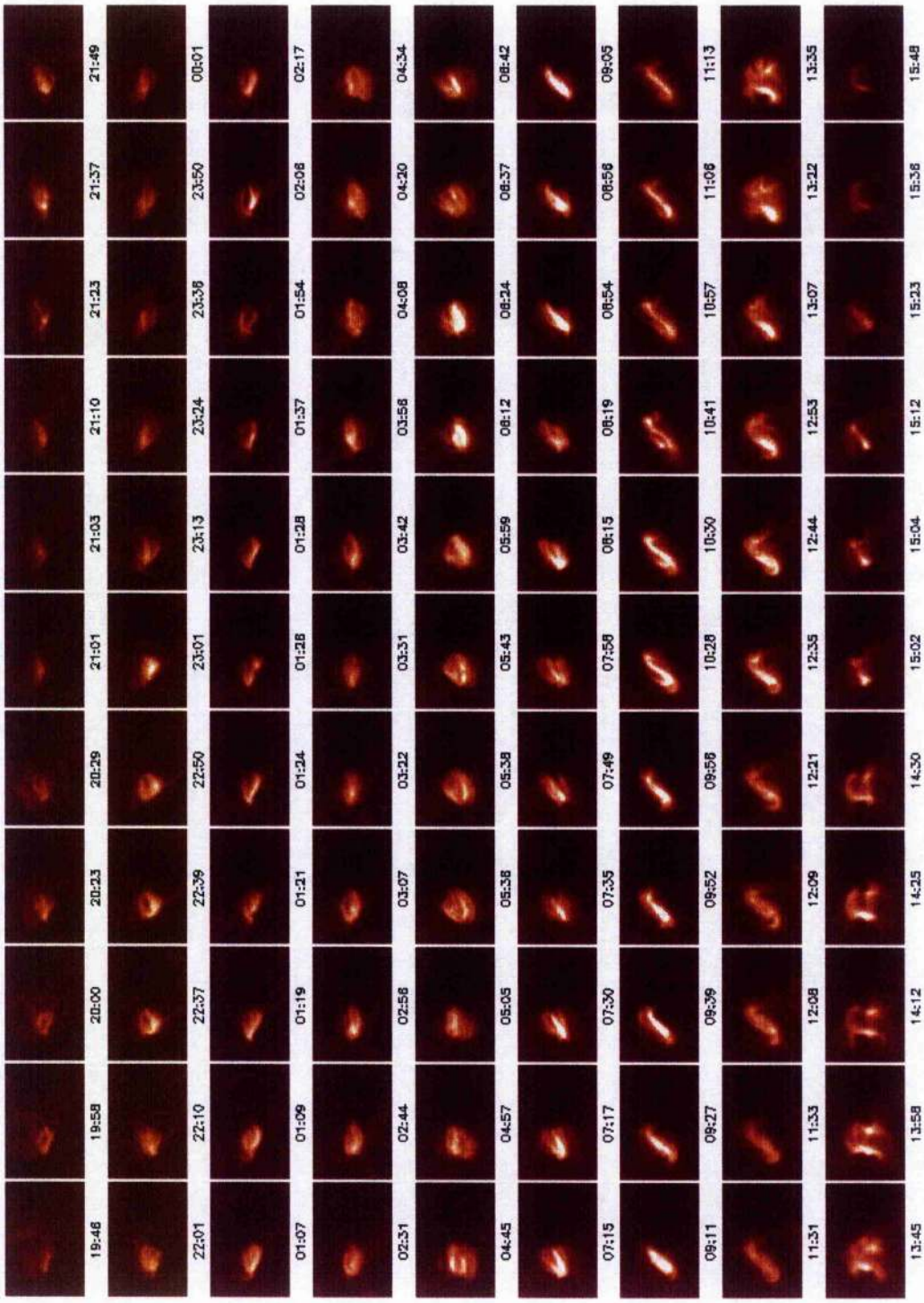

Figure 4.3: Evolution of a coronal bright point observed in Fe XII by TRACE on the 13th and 14th June 1998. Each frame is 75×50 arcseconds^2.

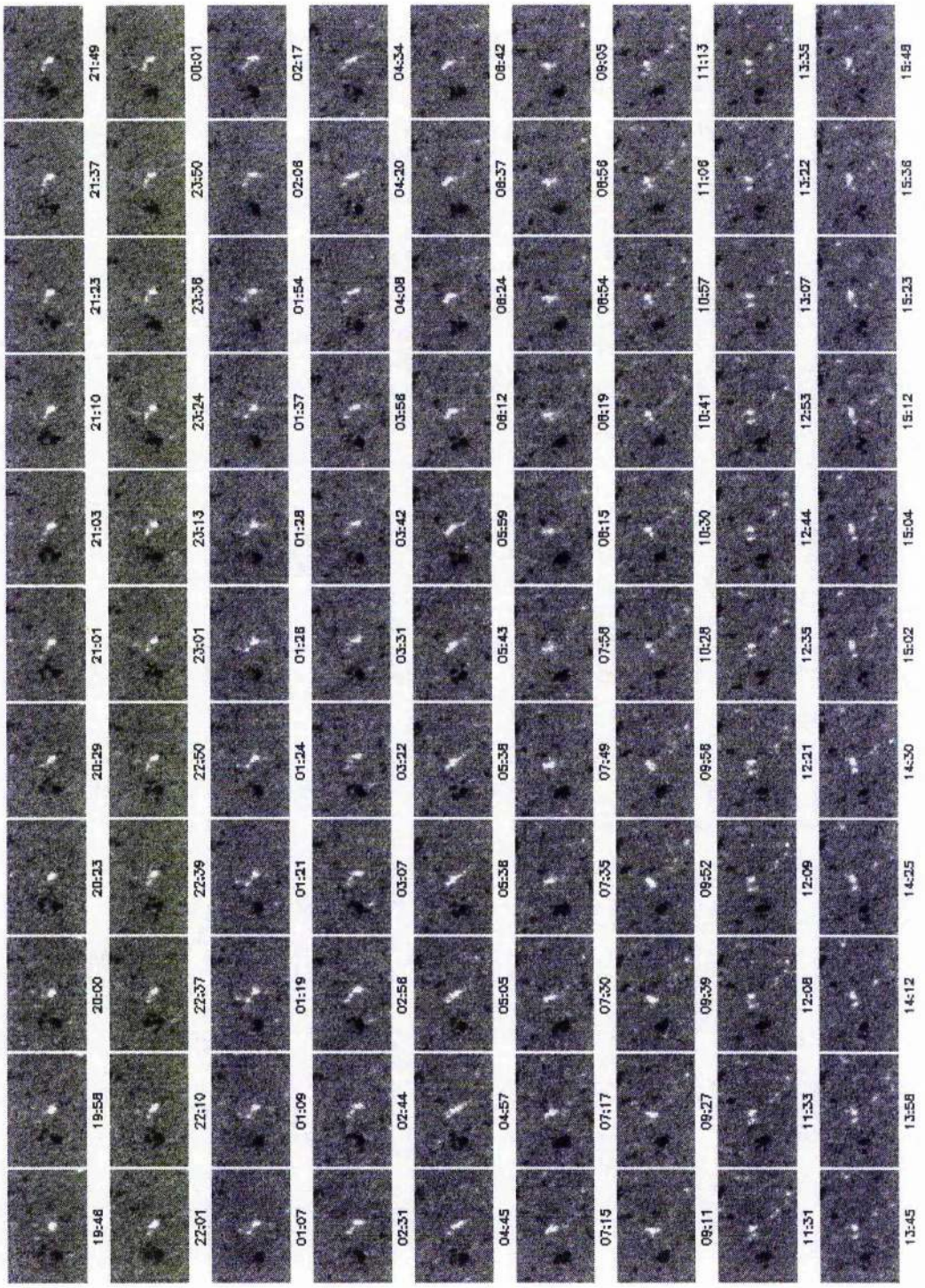

Figure 4.4: Evolution of the magnetic fragments responsible for the coronal bright point in figure 1, in magnetograms observed by SOHO/MDI. Each frame is 75×50 arcseconds^2.

from MDI high-resolution magnetograms (figure 4.4) have been extracted and de-rotated to eliminate lateral movement, allowing a morphological study to be carried out. The TRACE data has also been de-spiked (i.e., has had cosmic rays removed) and the dark current across the CCD has been subtracted. The Fe IX observations were taken at a spatial resolution of 0.5 arcseconds per pixel, while the Fe XII observations were taken at 1 arcsecond per pixel. So the Fe IX data cubes have had to be re-binned in order to make the resolution equal in each set.

By comparing two of TRACE's Fe lines (FeIX and FeXII) the spatial and temporal temperature and emission measure structure of the bright point has been investigated. This analysis indicates that this bright point is made up of a complex system of dense loops.

With the use of MDI magnetograms, it is possible to extrapolate the magnetic structure using an analytical constant-α force-free approximation. This extrapolation allows investigation of the topological properties of the magnetic field of the bright point and links topological bifurcations with dynamic changes in the behaviour of the bright point.

Extrapolated field lines can also be combined with temperature and emission measure maps which are calculated from the Fe IX and Fe XII observations from TRACE. The profile of these diagnostics can be calculated along the loop structures throughout the lifetime of the bright point and heating mechanisms of the loop structure can be analysed.

4.3 Behaviour of the Bright Point

The bright point (figures 4.2 and 4.3) appears at around 20.00 on 13th June and continues to grow and brighten over the next 12 hours. The bright point then begins to twist forming a sigmoid shape which lasts for the next 4 hours. This twist phase is followed by another 2.5 hour period in which the bright point is seen to have dramatically

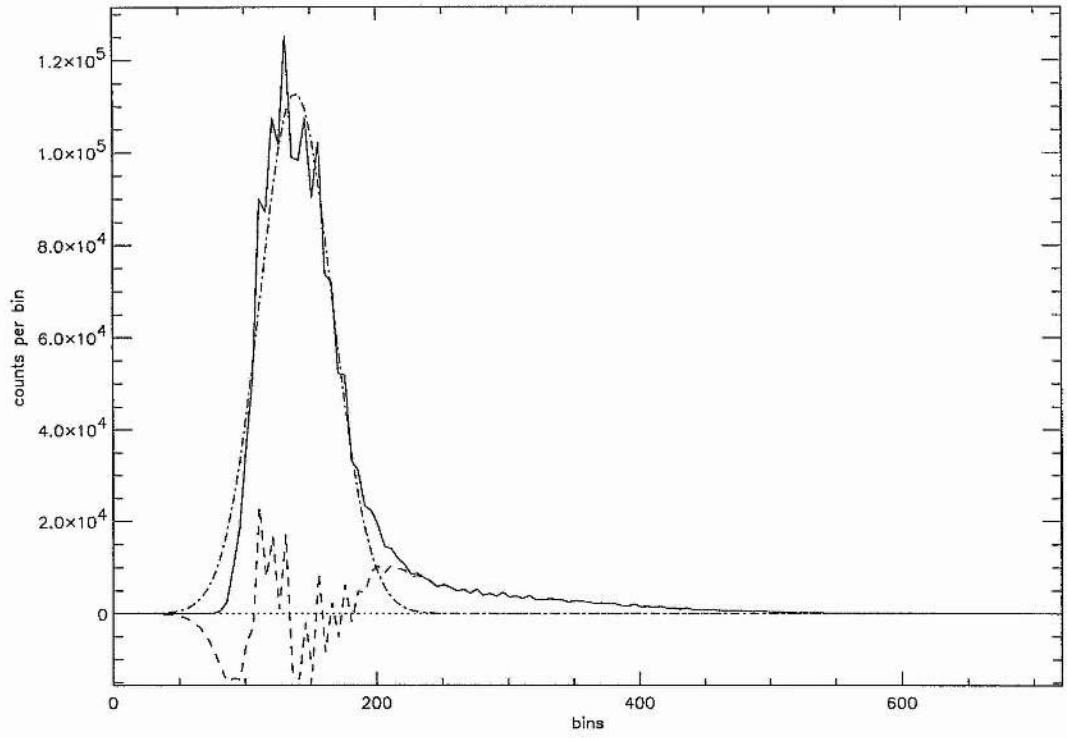

Figure 4.5: Plot showing the spread in pixel intensity values of the bright point observations in the Fe XII line (solid). A Gaussian curve (dot-dash), which represents the background intensity, is fitted to this and subtracted, the resulting curve (dashed) shows the 'tail' of the intensity curve, which is defined as being due to bright point pixels alone.

changed its structure to that of a π shape, before it disappears.

The bright point can be defined as being made up of pixels which, statistically speaking, are higher than background intensity. The intensity range covered by the background intensity is well fitted by a Gaussian curve, with the bright point producing a skewed tail at the high end of the distribution (figure 4.5).

Using this definition, several characteristics of the bright point are calculated. Figure 4.6 shows how the area of the bright point evolves over time. The bright point slowly grows over the course of about 20 hours to a peak associated with the π phase, after which it dramatically shrinks and fades.

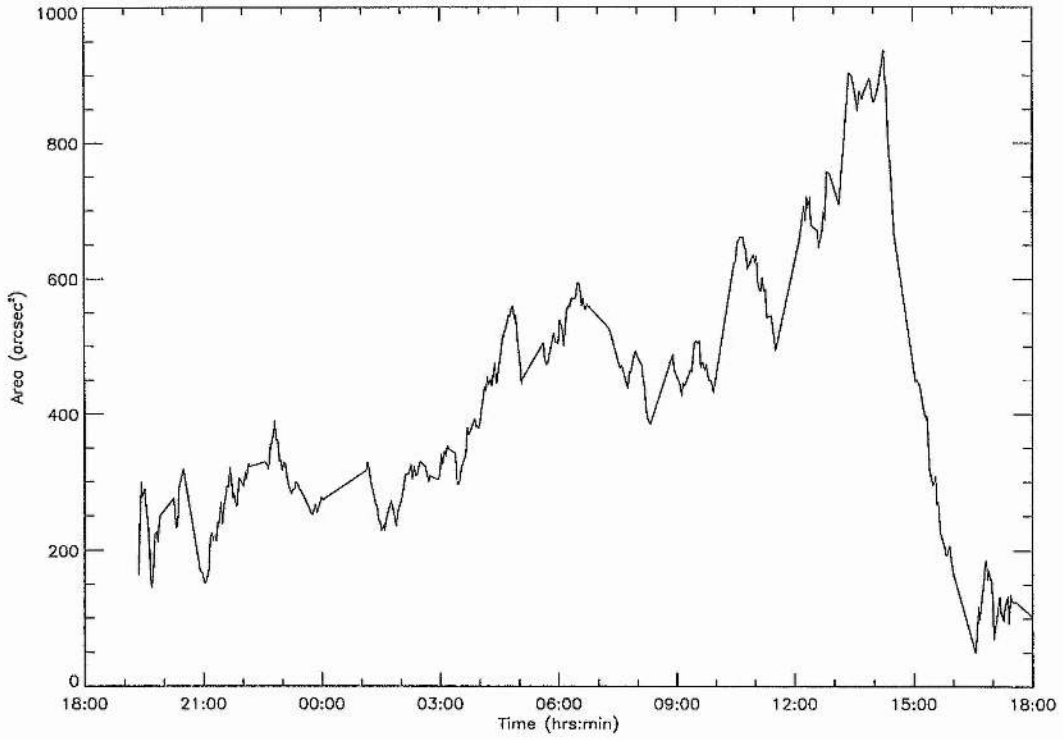

Figure 4.6: Plot showing the change in area of the bright point over the course of its lifetime.

Golub et al. (1974) suggest that the maximum area is proportional to the lifetime of the bright point (section 4.1) according to the relation

$$A_{max} = 2.5 \times 10^7 \tau, \tag{4.1}$$

where τ is measured in hours and A_{max} in km^2.

The lifetime of the bright point is about 23 hours and the maximum size it reaches is about 950arcsecond^2, which is approximately 5×10^8km^2. This is in reasonable agreement with equation 4.1 which predicts a maximum area of about 5.7×10^8km^2.

Key to the behaviour of the bright point is the behaviour of the magnetic fragments in the photosphere, where the bright loops have their foot-points. There are two large fragments, one positive (white patch in figure 4.4) and one negative (black patch in figure 4.4), that remain throughout the life of the bright point. The positive fragment migrates north as the bright point progresses.

Time	Bright point behaviour	Magnetic fragment behaviour
19:30	The bright point emerges becoming larger and brighter.	The single positive fragment dominates the negative fragments which form a 'paw print.'
23:00	The bright point deforms from a blurred blob into distinct loops.	The negative fragments coalesce and become as strong as the positive fragment which splits into two separate fragments.
03:00	The distinct loops begin to merge into a bright indistinguishable blur.	The negative fragment splits into a 'paw print' once more.
05:30		The two positive fragments coalesce into a single fragment.
06:40	The blur begins to resolve itself into distinguishable loops once more, which begin to twist.	The negative fragments coalesce and begin to dominate the positive fragments.
10:00	The bright point becomes even more twisted into its sigmoid phase	Small positive fragments start to approach the bright point from below.

Table 4.1: Summary of the behaviour of the bright point and the magnetic fragments in the photosphere.

There are some smaller negative fragments near the main one, forming a "paw print" shape (from 19:26 onwards). As the bright point evolves, these fragments approach the main one, forming a larger negative fragment (at about 23:30). These fragments (or new ones) later split from the main fragment (at about 03:20) to reform the "paw print" shape. The fragments coalesce once more (at about 07:00) to form a single fragment. A second smaller fragment starts to emerge (at about 11:00) and remains for the rest of the bright point's life.

At the beginning of the life of the bright point there is only the main positive frag-

Time	Bright point behaviour	Magnetic fragment behaviour
11:00		A new negative fragment begins to emerge near the existing negative fragment.
13:00	The twist becomes too much and the structure breaks into a π-shape.	The positive fragments have become closer to the bright point and the number of significant fragments has dramatically increased.
15:00	A large portion of the bright point has dispersed leaving some smaller loops which quickly fade.	Many of the fragments disappear as the bright point is dispersed leaving smaller more balanced fragments

Table 4.2: Summary of the behaviour of the bright point and the magnetic fragments in the photosphere.

ment. This fragment splits into two smaller fragments (at about 23:00), one of which splits again (at about 02:30). These fragments then coalesce (at about 05:00). This single fragment is joined by several smaller fragments (at about 10:00) which appear below the main fragment and migrate north. At this point the main positive fragment separates into two smaller fragments. This is summarised in tables 4.1 and 4.2 .

It is also important to look at the flux passing through the photosphere due to these key fragments. Figure 4.7 shows the total positive flux and the total negative flux from the significant fragments. Note that there is no evidence of flux cancellation (except when the bright point fades) and the MDI observations (figure 4.4) do not show the two main fragments approaching one another. This suggests that the bright point is not above a canceling magnetic feature (section 4.1).

Figure 4.8 shows the total positive and negative flux from the significant fragments for an extended period of time which includes the bright point. This could indicate that the two main fragments are emerging and that the bright point lies above an ephemeral

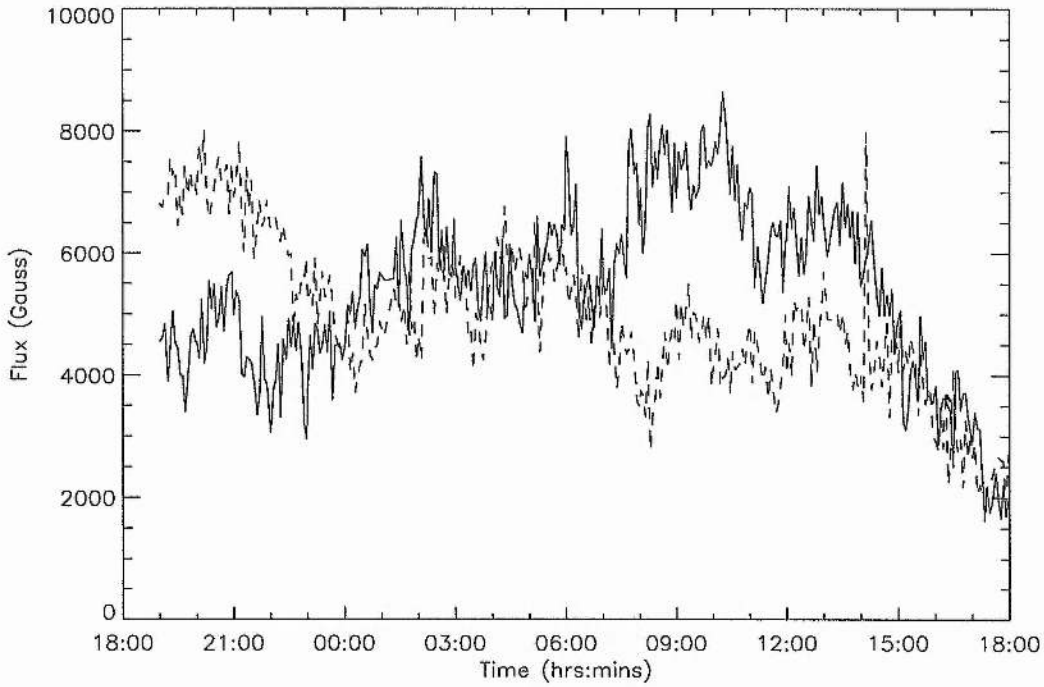

Figure 4.7: Plot showing the variation of flux passing through the magnetogram during the lifetime of the bright point. The dashed line shows the total flux from significant positive fragments, the solid line shows the total flux from significant negative fragments.

region. However, a close study of the magnetograms, before the bright point emerges, suggests a different explanation.

Both the main positive and negative fragments exist at least seven hours before the bright point emerges. At this time they are not strong, but they lie at the intersections of supergranule cells where strong down-flow occurs. This means that other small fragments, that exist or emerge nearby, approach the main ones causing them to grow in size and strength (figure 4.9).

When the expanding fragments reach a certain strength (the total flux of the fragments becomes about $8-10\times10^3$ Gauss), the bright point begins to form (at around 18:00 on the 13th). When the total flux falls below this threshold the bright point dies (around

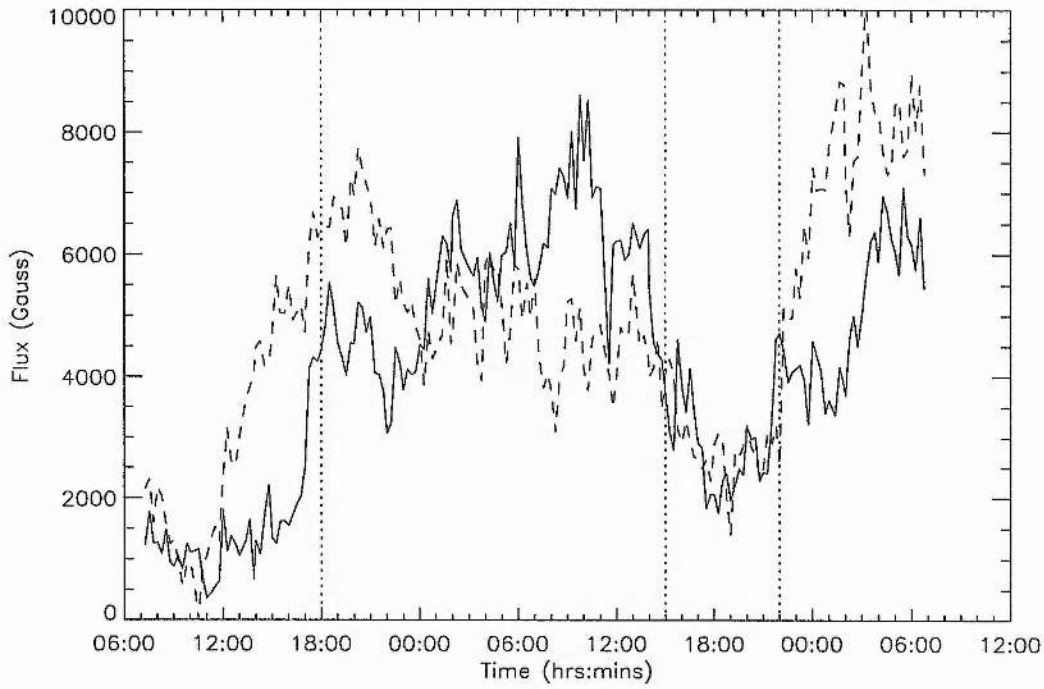

Figure 4.8: Plot showing the variation of flux passing through the magnetogram from 7 hours before the bright point emerges to 15 hours after it dies. The dashed line shows the total flux from significant positive fragments, the solid line shows the total flux from significant negative fragments. The lifespan of the bright point is indicated by the dotted lines at 18:00 and 15:00. There is a third line at 22:00 which indicates the appearance of another bright point in the region.

15:00 on the 14th). A new bright point emerges close by several hours later, involving some of the fragments from the previous bright point.

This suggests that the mechanisms that produce bright points are not as straightforward as has previously been believed (cf section 4.1) but involve complex interactions between small magnetic fragments.

The phrase "significant fragments" is used to denote fragments that are made up of pixels which have a strength of 50 Gauss or higher and are contained within the bounding box shown in figure 4.10. These limits were decided upon after testing other choices.

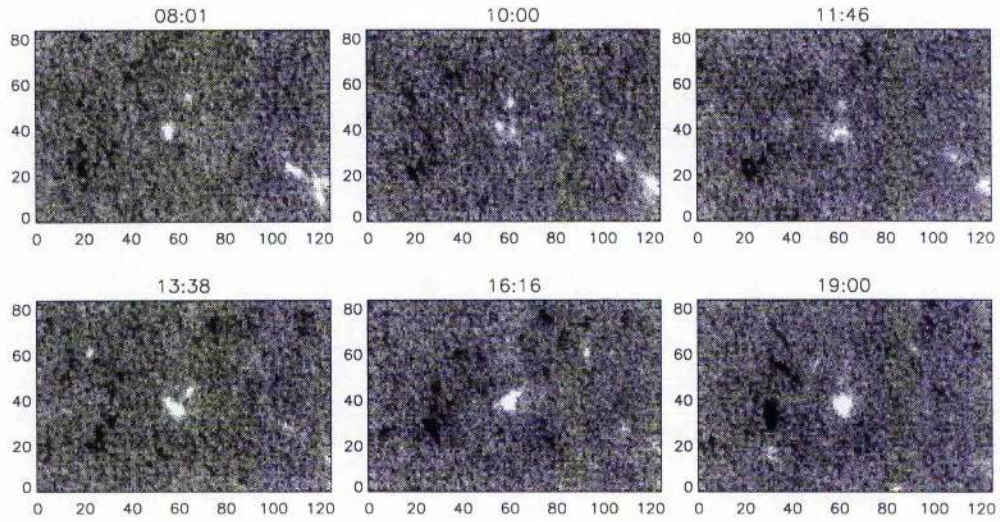

Figure 4.9: Magnetograms showing the bright point region before its emergence. The main positive and negative fragments grow as other fragments merge with them.

The value of 50 Gauss is good for isolating the key fragments without losing much precision, it also eliminates most of the unwanted background noise. Small perturbations in the bounding box size have little effect on the amount of significant flux. If a fragment is going to migrate into the region of interest it will still enter a slightly smaller or larger box, it will just do it a couple of frames earlier or later. It is noted that fragments outside the box may still have an effect on the bright point, however, their effect is not as significant as those inside the box.

Figure 4.7 indicates four key phases. First, the positive flux is stronger than the negative flux, but at about 00:00 the two flux strengths approach the same level. They remain approximately equal until about 07:30 when the negative flux increases and dominates over the decreasing positive flux. Finally, at about 15:00 the negative flux decreases to the level of the positive flux and they both tail off equally as the bright point dies.

These changes in behaviour of the magnetic fragments are prime candidates for changes in the behaviour of the bright point. The first major change occurs between 23:00 and 00:00 and is reflected in the behaviour of the positive and negative fragments and their relative strengths. The only noticeable change in the behaviour of the bright point at

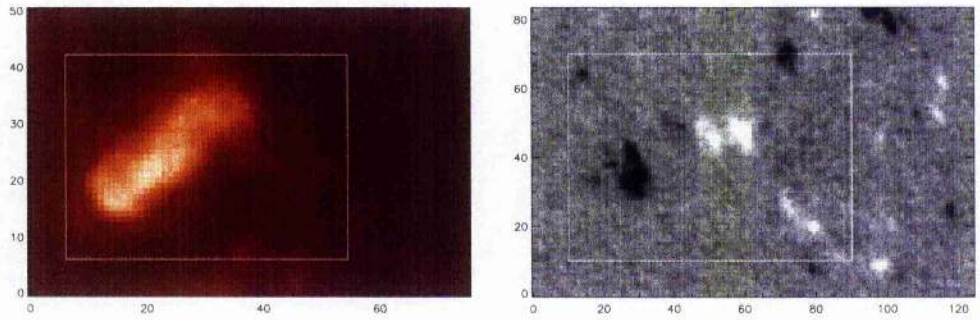

Figure 4.10: Plot showing the region where significant fragments for the bright point are assumed to be located. The image used is for the bright point at 11:33 on 14th June.

this time is that the brighter 'blobs' in figures 4.2 and 4.3 begin to resolve themselves into more definite loop structures.

The next significant change occurs at about 07:00, when the negative fragments coalesce and the total negative flux becomes greater than the positive negative flux. It is at this point that the bright point loops begin to twist into the sigmoid shape.

The splitting of the main fragments and the introduction of the new positive fragments that occurs from 10:00 onwards could cause the excess twist which breaks into the π-phase at about 12:00, the late occurrence of the π-phase being due to the new positive fragments approaching the bright point region.

4.4 Calculating Temperature and Emission Measure

The temperature of the region may be calculated using images taken at very similar times in the Fe IX and Fe XII lines of TRACE. By taking the ratio of a pair of Fe XII and Fe IX images normalised to the same exposure time and applying a temperature scaling (figure 4.11), a temperature map may be constructed.

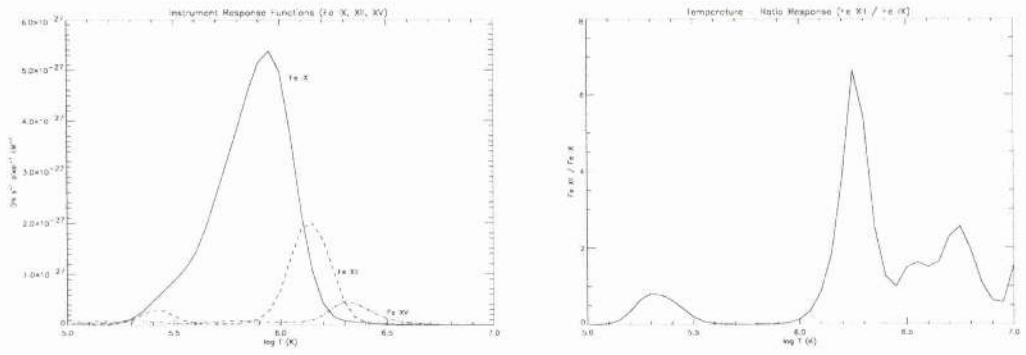

Figure 4.11: The scaling (right) for creating temperature maps can be obtained by finding the ratio of the Fe XII and Fe IX instrument response functions (left).

Emission measure maps can then be found by using the formulae

$$EM = l{n_e}^2 = \frac{d_n}{t_{ex}S(T)},$$

where n_e is the particle density, l is the line of sight depth, d_n is the counts per pixel from the the observed image, t_{ex} is the exposure length and $S(T)$ is the temperature map passed through the instrument response function (sensitivity function, see figure 4.11) of the observed image being used.

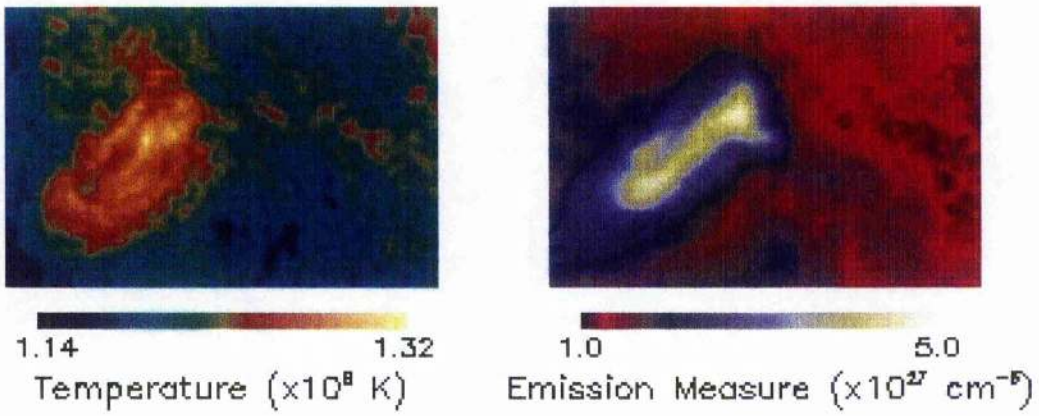

Figure 4.12: Temperature and emission measure maps of the bright point at 11.00 on 14th June 1998.

The emission measure maps of the bright point seem to be much more structurally well defined than the temperature maps (figure 4.12 for example). The bright point does not

appear much hotter than the background.

Figure 4.13 shows temperature maps of the bright point at various stages of its lifetime, with contours of the emission measure overlaid. As the emission measure is proportional to the density squared, this gives some idea of where the plasma is located.

In general it is clear that the regions of peak emission measure of the bright point do not correspond to the regions of peak temperature. This means that the densest plasma is not the hottest.

It is difficult to interpret this because, when the ratio of two filter lines is taken, only the plasma at a temperature common to both filters is registered. Effectively, the temperature range that can be 'seen' is between 1.0 and 1.5 million Kelvin. It is entirely possible that there are hotter loops of plasma which are not picked up in this process (cf Lenz et al., 1999).

4.5 Variation of the Temperature and Emission Measure of the Bright Point

By averaging the regions of the temperature and emission measure maps corresponding to the bright point (cf figure 4.6), the changes in these quantities over the lifetime of the bright point can be studied.

Again, only plasma in the temperature range allowed by the filters (see section 4.4) can be studied, but the behaviour of this plasma still provides some insight of the general behaviour.

The temperature variation (figure 4.14) is fairly small throughout the lifetime of the bright point and the average temperature of the bright point is generally just a little higher than the background temperature. The slight rise in temperature as the bright point begins is mirrored in the background temperature. This may be because as the bright point forms, flux tubes are heated before being filled with plasma. As these flux

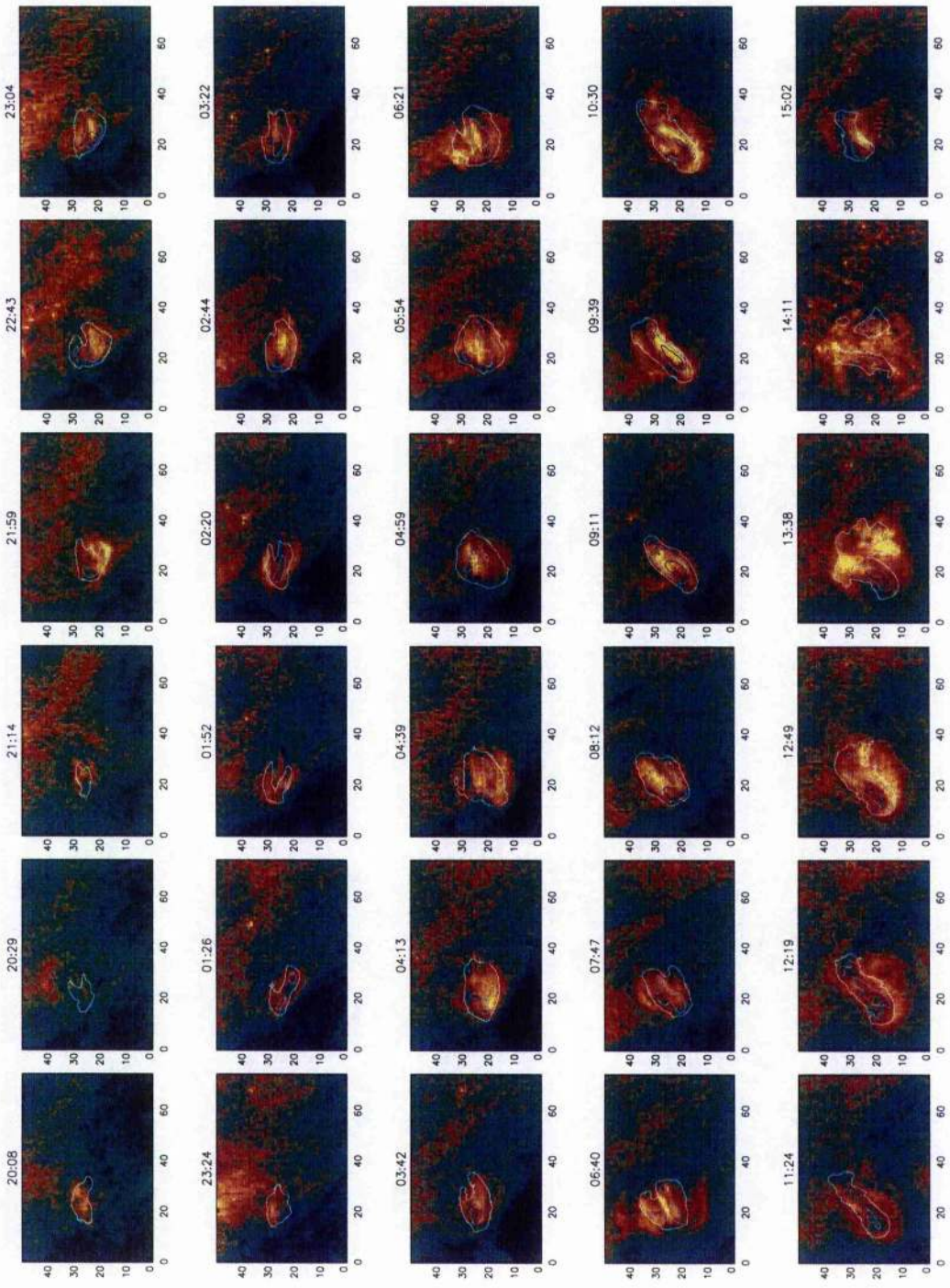

Figure 4.13: Temperature maps with emission measure contours at $3 \times 10^{27}\mathrm{cm}^{-5}$ (light blue), $4 \times 10^{27}\mathrm{cm}^{-5}$ and $5 \times 10^{27}\mathrm{cm}^{-5}$ (dark blue) of the bright point.

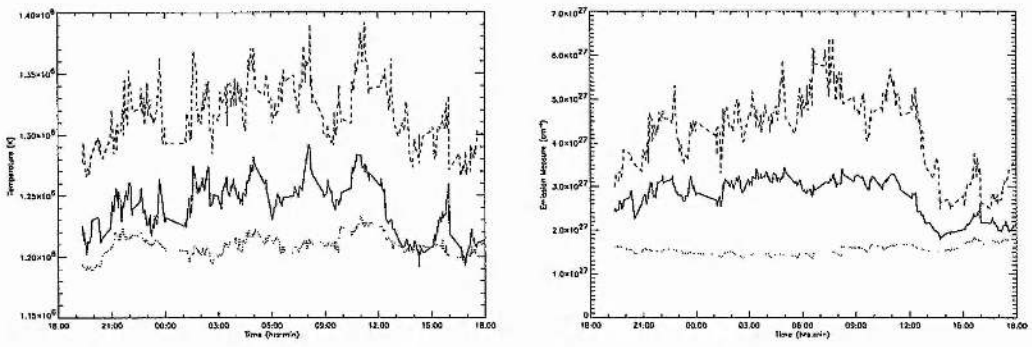

Figure 4.14: Variation of the temperature (left) and emission measure (right) of the bright point. Solid lines indicate the average temperature/emission measure of the bright point, dotted lines indicate the background temperature/emission measure and dashed lines indicate the peak temperature/emission measure.

tubes fill they brighten, causing the bright point to expand.

The variation of emission measure is much more pronounced. This suggests that the loops in the bright point are visible mainly due to being denser than their surroundings rather than hotter. Note that as the emission measure in the bright point increases, the background emission measure decreases. This may be because flux tubes in the background are heated and injected with plasma which causes them to become visible in the Fe lines. They are then counted as part of the bright point, which leaves only the lower emission measure loops in the background.

The rise in background emission measure as the bright point emission measure decreases implies that loops in the bright point cool faster than their plasma is dissipated.

Golub et al. (1974) suggested that density variations are between 2 and 4 times higher than the coronal average (section 4.1). Figure 4.14 falls slightly below this, with the emission measure being a factor 2 to 4 higher. Thus the density (which is proportional to $\sqrt{EM}$) is about 1.4 to 2 times higher than the background density.

One feature to note with the temperature and emission measure plots (figure 4.14) is that the average and peak temperature/emission measure drops off rapidly between 12.00 and 13.00, where the area of the bright point (figure 4.6) increases towards its

peak value. This corresponds to the end of the sigmoid shape and the beginning of the π phase. So what is happening is that the bright point rapidly expands and the plasma, which was previously contained in tight loops, is spread throughout the larger area. This allows the plasma to cool quickly.

Most of the plasma in the π shape disperses over the next 3 hours leaving a smaller loop structure, which corresponds to the small peak between 15.00 and 16.00 in figure 4.14 that fades away signalling the end of the lifespan of the bright point.

4.6 Extrapolating the Magnetic Field

Taking the MDI magnetograms as boundary conditions, magnetic field lines can be extrapolated using a constant-α force-free field method (Chiu and Hilton,1977; Lothian and Browning, 1995). For each Fe XII image in figure 4.15, the magnetic field has been extrapolated for the value of α, to within an accuracy of ± 0.1, which visually gives the best field line fit.

These extrapolations are vital to explain the evolution of the bright point. They show the structure of the magnetic field of the bright point, and how the field is twisted. The value of α is a measure of the twist of the magnetic field. The variation of α can be seen in figure 4.16. The field starts to twist in one direction ($\alpha < 0$ between about 23.00 and 04.00) before it untwists (at about 02.00) and twists in the other direction, reaching a peak of about 3.5, before falling off when the bright point disappears.

Section 4.3 suggested several times where changes in the behaviour of the magnetic fragments resulted in changes in the behaviour of the bright point. There is some coincidence with these times and the behaviour of the value of α. There were large behavioural changes at about 23:00 of the fragment behaviour and it is at about this time that α first changes from positive to negative.

From around 21:00 to 02:00 the negative fragments coalesce into a single fragment which shrinks in size, whereas the positive fragment spreads itself out and fragments.

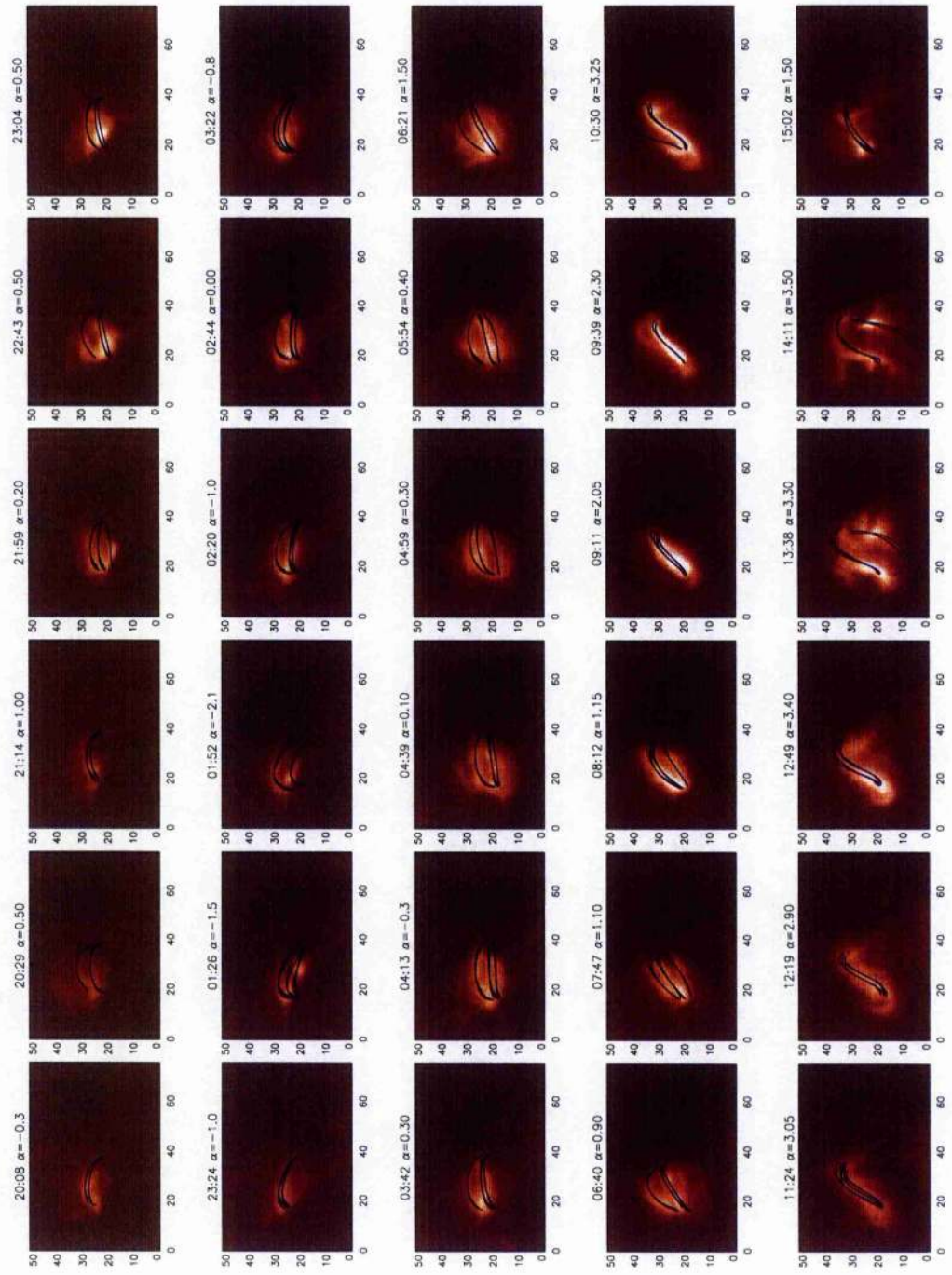

Figure 4.15: Extrapolated field line for the bright point, using MDI magnetograms and TRACE Fe XII images. The field lines (blue) are projected onto the TRACE images for comparison. The observation time and the value of α used for extrapolation are displayed. Note, α is a spatial constant, not a temporal one.

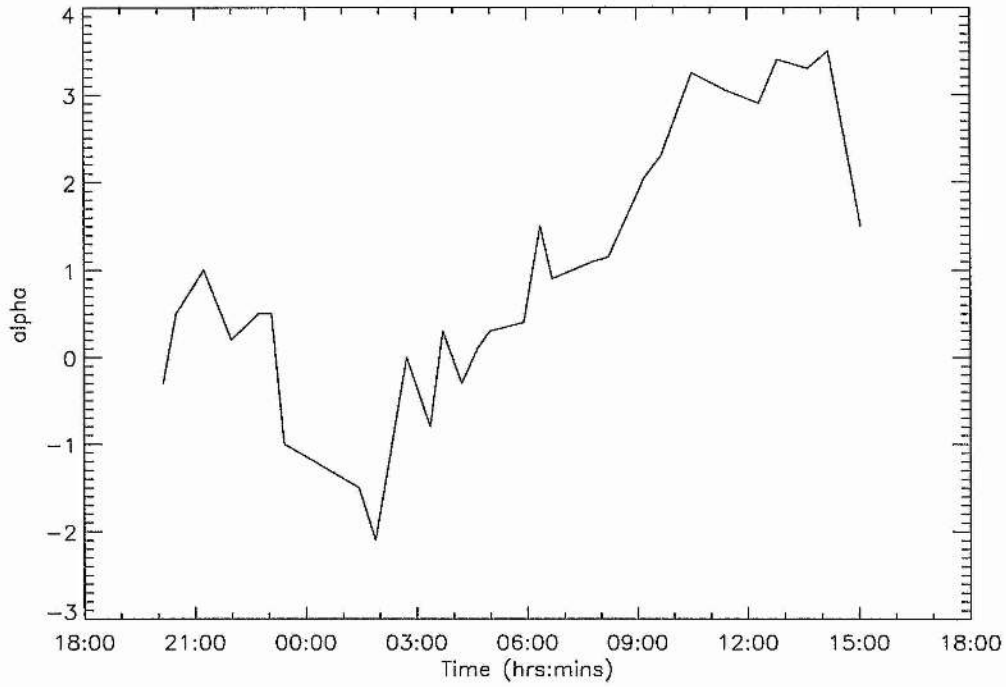

Figure 4.16: Variation of the constant-α of the extrapolated field during the lifetime of the bright point.

This is responsible for the decrease in the value of α to its minimum of $\alpha = -2$.

During this time the main positive and negative fragments remain level, but after 02:00, the positive fragment begins to migrate north and the negative fragment migrates south, so the fragments no longer remain level. This causes the value of α to increase, becoming positive between 03:00 and 05:00.

At 10:00 smaller positive fragments appear below the main fragments. This event coincides with the value of α reaching its peak. The peak twist corresponds to the sigmoid-phase and the π-phase of the bright point. In the observations for these phases, the bright point loops are visibly twisted.

The extrapolated field lines in figure 4.15 show how the structure of the bright point changes. During the earlier stages of the bright point, when the main fragments break up or coalesce, there is more than one loop structure in the bright point. However,

when the sigmoid phase begins the plasma forms only one distinct loop. The twisting action causes the field lines to bunch together, bringing the separate loop structures close enough together to form a single loop of plasma.

It must be noted at this point that, although the extrapolated field lines for the π-phase are not unreasonable, this is the most dynamic phase during the lifetime of the bright point. Therefore, it is during this phase that a magneto-hydro-static approximation, such as the constant-α force-free method, may not be as valid as during other phases of the bright point.

4.7 Temperature and Emission Measure along Loops

By comparing these extrapolated magnetic field lines of the loop structures with the temperature and emission measure maps, the temperature and emission measure profiles along loops can be deduced.

It is tempting merely to match points along the loop with points in the temperature or emission measure maps. This has an obvious drawback, as the extrapolated field line is an approximation, it may not necessarily lie directly along the 'middle' of the loop structure. As there will be variation of the diagnostic across the loop, it would be preferable to incorporate some form of averaging across the loop.

4.7.1 Calculating the diagnostic along the loop

From the extrapolated field lines, a sequence of equally spaced points along the loop can be deduced. At each point along the loop, a line of fixed length which is perpendicular to the loop and centred on the loop can be calculated. Equally spaced points along this line and their associated temperature or emission measure can then be found, and these diagnostic values can be averaged (figure 4.17).

For the bright point maps in this chapter, the extrapolated field lines are divided accord-

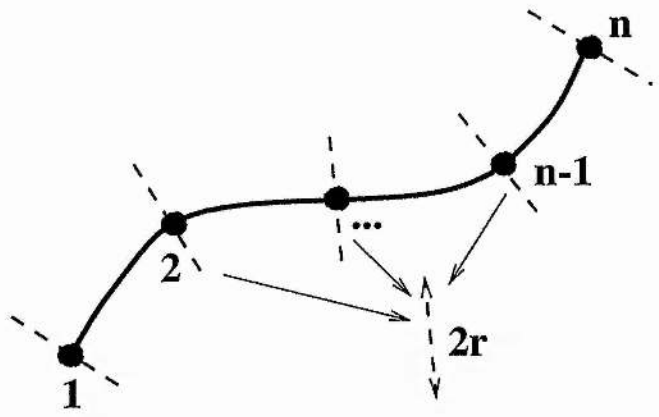

Figure 4.17: The extrapolated loop is divided into n equally spaced points, at each point a perpendicular line of length $2r$ is calculated and the average value of the temperature or emission measure along this line is calculated.

ing to their length and the resolution of the images. All of the images have a resolution of 1 pixel width (1 arcsecond). If the line has an arc-length of 35 arcseconds (pixel widths), say, then it is divided into 36 points (i.e., 35 gaps of 1 arcsecond in length).

The perpendicular lines have a length of 10 arcseconds and is split at arcsecond intervals. This gives 11 points for the temperature/emission measure to be averaged over (1 point on the extrapolated field line and 5 points on either side). This length has been chosen as it best reflects the width of the bright loops in the Fe XII images.

4.7.2 Calculating diagnostic errors along the loop

The temperature and emission measure results are subject to both random and systematic errors. Random errors are mainly due to effects like photon statistics and data compression and decompression. Systematic errors are largely due to the calibration of the instrument.

It is difficult to be able to estimate systematic errors, but, as they are filter dependent,

they will be proportionally constant for all measurements, i.e.,

$$\frac{\Delta I}{I} = constant, \tag{4.2}$$

for all intensity measurements, I. As this has not been calculated for the TRACE filters yet, this work will just concentrate on these random errors, which will be calculated in the same way that Klimchuck and Gary (1995) calculate errors for soft x-ray lines.

Consider a pair of observations of an isothermal plasma from two different filters which have intensities I_1 and I_2. The intensities are assumed to have a Poisson distribution, so the respective standard deviations of the intensities are $\sigma_{I_1} = \sqrt{I_1}$ and $\sigma_{I_2} = \sqrt{I_2}$ (Grimmett and Welsh, 1986; Feynman et al., 1977). The ratio of the two intensities is given by

$$R = \frac{I_1}{I_2}. \tag{4.3}$$

The temperature is then a function of R, so $T = T(R)$.

The standard deviation of the temperature is given by

$$\sigma_T = T\frac{d\log T}{d\log R}\left[\left(\frac{\sigma_{I_1}}{I_1}\right)^2 + \left(\frac{\sigma_{I_2}}{I_2}\right)^2\right]^{\frac{1}{2}},$$

and the standard deviation of the emission measure is given by

$$\sigma_{EM} = EM\left[(1+c)^2\left(\frac{\sigma_{I_1}}{I_1}\right)^2 + c\left(\frac{\sigma_{I_2}}{I_2}\right)^2\right]^{\frac{1}{2}}, \tag{4.4}$$

where c is given by

$$c = \frac{d\log S}{d\log T}\frac{d\log T}{d\log R}, \tag{4.5}$$

where S is the instrument response function which was used to calculate the emission measure (see figure 4.11).

There is a further error calculation to be made when the pixel temperatures are averaged (section 4.7.1). The standard deviation must reflect this, so consider a set of pixels with diagnostic values $d_1, \ldots, d_n$, which are considered as being independent. These

have standard deviations $\sigma_1, \ldots, \sigma_n$ accordingly. The average value of the diagnostic is given by

$$\bar{d} = \frac{1}{n}\left(d_1 + \cdots + d_n\right), \tag{4.6}$$

and the associated standard deviation is

$$\sigma_{\bar{d}} = \frac{1}{n}\left(\sigma_1^2 + \cdots + \sigma_n^2\right)^{\frac{1}{2}}. \tag{4.7}$$

This is given in Topping (1962).

When calculated, these errors turn out to be small (cf figure 4.18), so the temperature and emission measure calculated is accurate within the confines of the model and its assumptions.

4.7.3 Temperature and emission measure along the extrapolated loops

It is difficult, as noted in section 4.5, to conclude much from the temperature variation along the loop. The temperature range which is being studied is small, so the temperature along the loops only varies between about 1.2 and 1.3 million Kelvin. In general, the temperature profiles resemble the classic profile (Rosner et al., 1978; Serio et al., 1981) where the loop centre is the hottest and the temperature tails off as the foot-points are approached. This is especially true between 05:00 and 13:00 where the extrapolations 'look' to be better fits than for earlier times.

The emission measure is, in general, skewed so that it is larger nearer the negative fragment. This would suggest that there is more plasma above the negative fragment which is either denser or in flux tubes that approach the fragment at a steeper angle than at the positive fragment so that the line-of-sight depth is longer. The extrapolations suggest that the latter case does not hold (if anything, the reverse is true), so that the plasma is denser over the negative fragment.

The reason for this higher emission measure could be due to there being more field line

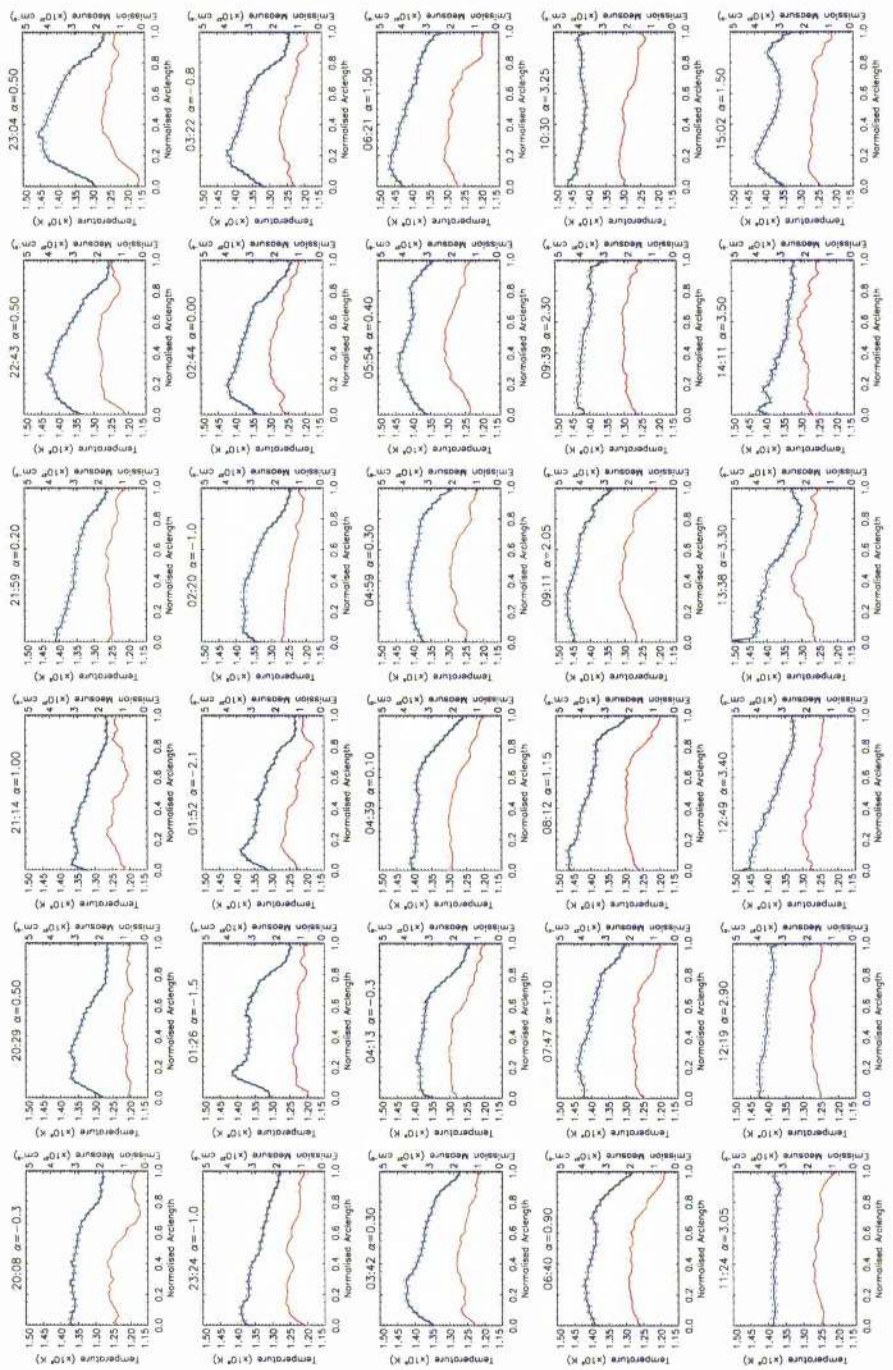

Figure 4.18: Temperature (red) and emission measure (blue) profiles with associated errors (two standard deviations) along the loop structures of the bright point, using the best extrapolated field line from the previous section as the path of the loop. The field line lengths are all normalised to 1.

activity near the negative fragment than the positive fragment. This would be characterised topologically by more null points, which is evident during the fragmented paw-print stages of the negative fragments, and more separatrices near the fragment.

It could also be due to the dynamical nature of the system. The topological analysis regards each case as being a relaxed snapshot. This may be a reasonable assumption for the configuration of the magnetic field, but it does not provide information on the plasma flow along field lines. For example, if a siphon flow were present then a density imbalance would be expected.

4.8 Topological behaviour of the bright point

4.8.1 The behaviour of magnetic fragments

Topologies are best calculated using a point-source representation of magnetic fragments, so the magnetograms must be converted accordingly. Each fragment is assumed to be made up of pixels with a strength of 50 Gauss or higher, so the total flux passing through each fragment is summed and the centre of the fragment is calculated. So each fragment is then represented by a point source located at the centre of the fragment with a strength proportional to the total flux passing through the fragment.

Combining these point-source representations and the values of α calculated in section 4.6, the topologies of the bright point can be calculated using the constant-α force-free technique. These topologies can be seen in figure 4.19.

The first feature that is clear is that the topological behaviour becomes more complex as the bright point progresses, this is due to the splitting of fragments and the emergence of new fragments. This is because the extra flux sources result in more topological regions, and hence extra separatrix surfaces to divide the topological regions.

Figure 4.20 shows the number of positive and negative fragments during the life-time

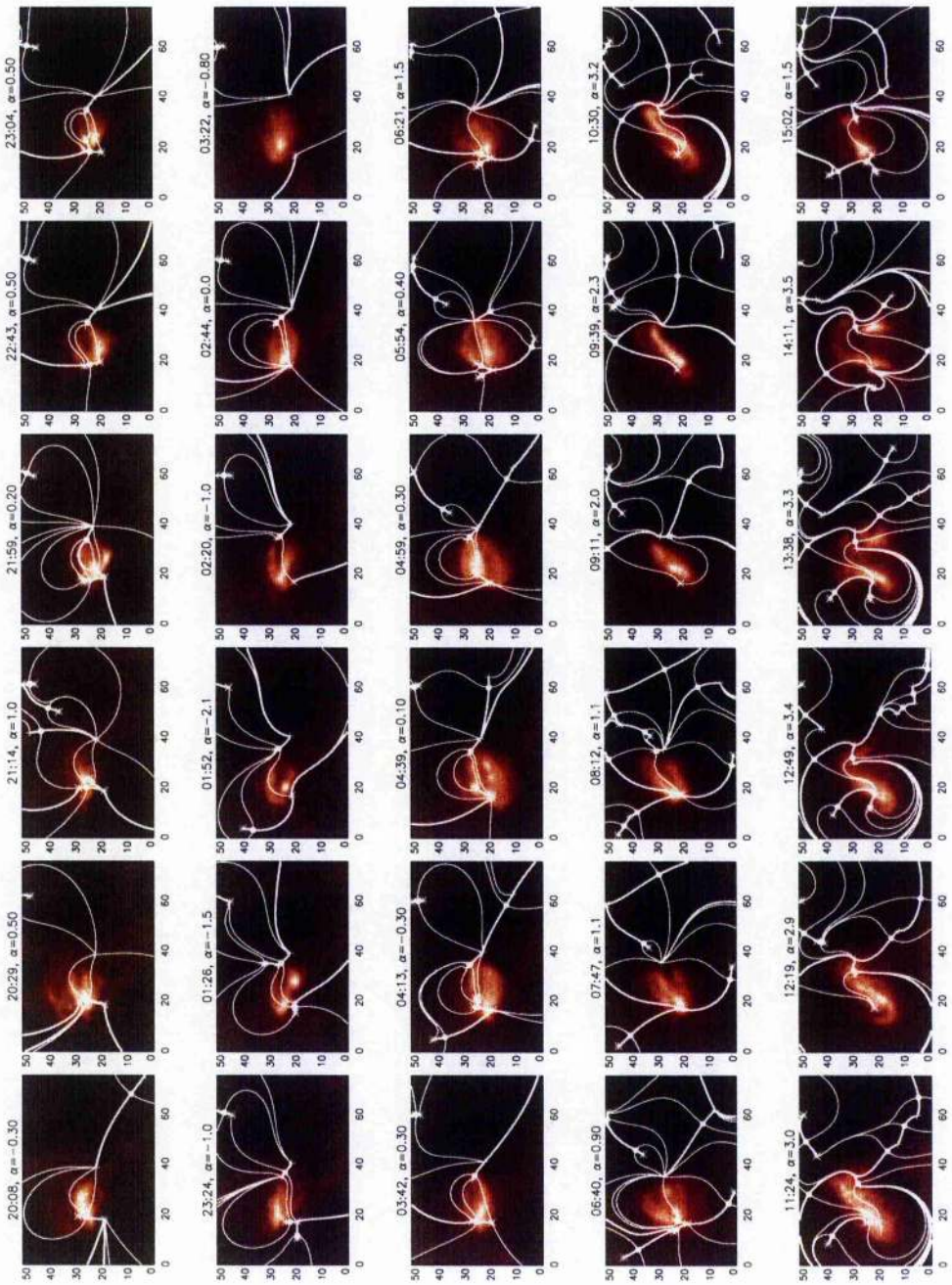

Figure 4.19: Diagrams indicating the magnetic topology of the bright point. The fan and spine field lines in the $z = 0$ plane are plotted to show the topological regions. These lines overlay the corresponding Fe XII observations. The asterisks represent negative fragments and the pluses represent positive fragments.

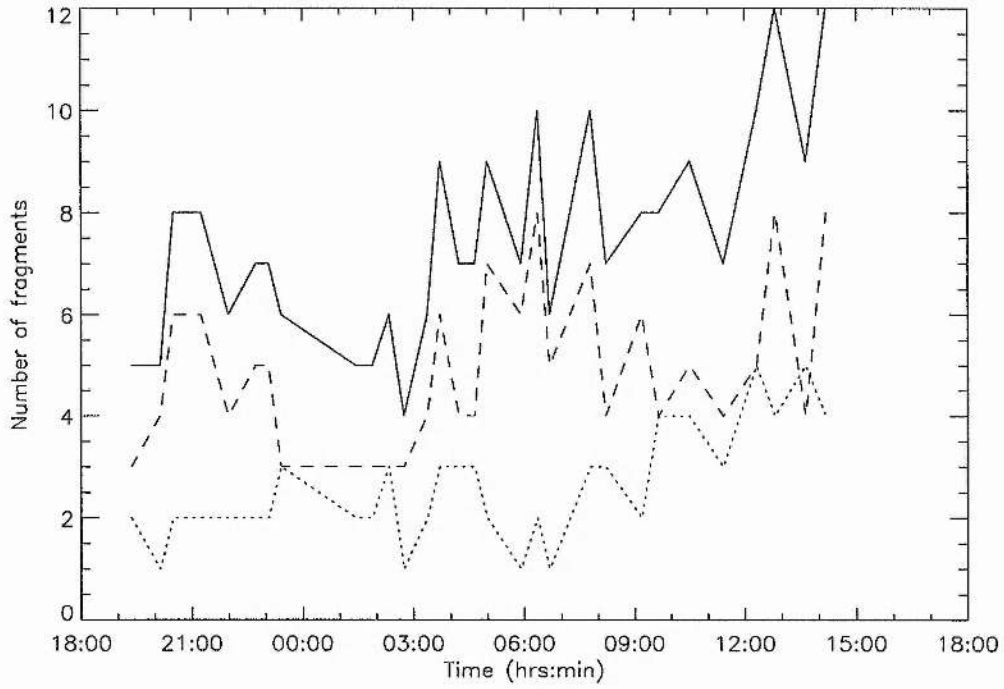

Figure 4.20: Variation in the number of significant fragments during the life of the bright point. The solid line is the total number of fragments, the dashed line is the number of negative fragments and the dotted line is the number of positive fragments.

of the bright point. The total number of fragments falls to four significant fragments at about 03:00, when the main fragments begin to split and new fragments appear. This generally increases for the remainder of the bright point.

The decrease in fragments at the beginning of the bright point is largely due to the coalescence of the negative fragments, which reach an early peak of six fragments before decreasing to a minimum of three fragments at about 23:00. These fragments split and new fragments appear at about 03:00 and coalesce again at about 09:00. Finally, the number of negative fragments increases from about 11:00.

The behaviour of the positive fragments almost mirrors this. The number of positive fragments increases until about 23:00. It levels off until about 05:00 before dipping for a couple of hours. It then starts to increase at about 08:00 and rises to almost the

level of the number of negative fragments.

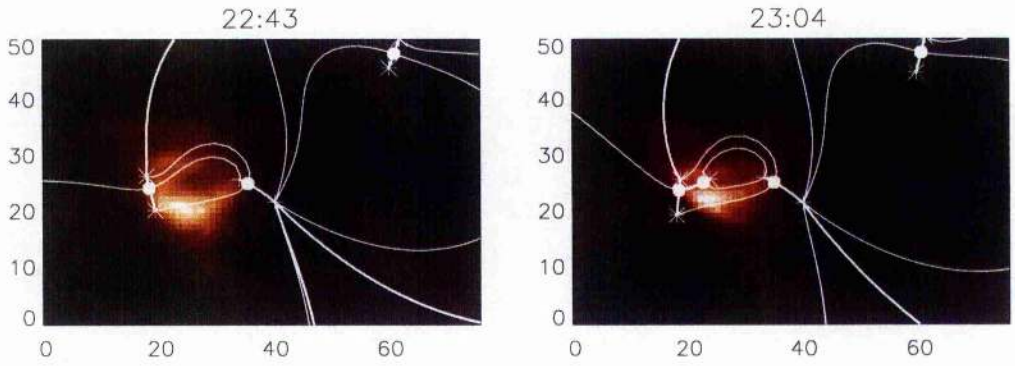

Figure 4.21: The topology at 23:04 is almost the same as that at 22:43 except a new negative fragment has emerged near the centre of the bright point causing a new small separatrix dome to appear. The asterisks represent negative fragments and the pluses represent positive fragments.

It is this variation in the number of fragments that makes it difficult to tell where important topological changes take place. Every time a new fragment appears or one disappears, a dramatic effect on the topology is apparent. Sometimes this can be easily identified, such as the change between the topology at 22:43 and 23:04 (figure 4.21). The two topologies are almost identical, the only difference is that a new fragment has appeared near the centre of the bright point. This fragment accepts flux only from the nearby positive fragment and so a separatrix dome is formed enclosing the new fragment. The new fragment that appears at 23:04 probably exists at 22:43, except it is smaller and not considered to be significant.

4.8.2 Small-scale topological behaviour

The majority of fragment appearance and disappearance happens close to the bright point causing small-scale local topological change between almost every topological state.

Relative changes in positions between fragments also cause bifurcations between states.

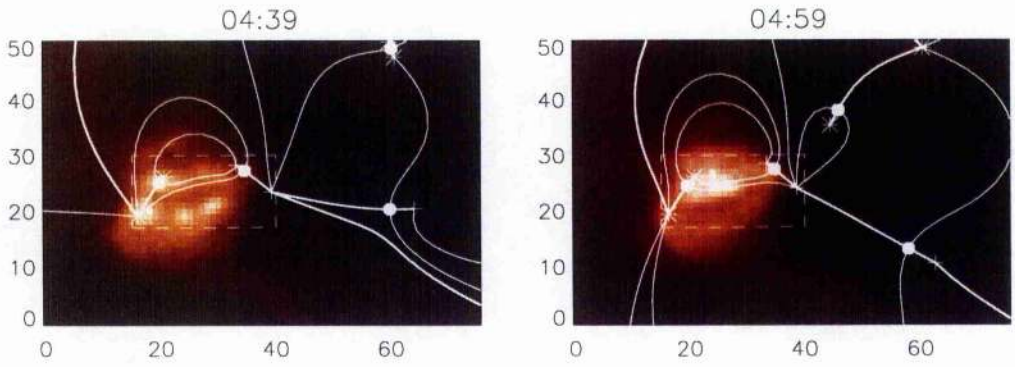

Figure 4.22: Changing topology of the bright point between 04:39 and 04:59. The motion of the fragments in the dashed box causes the magnetic field to undergo a global-separator bifurcation.

For example, the motion of the fragments between 04:39 and 04:59 causes the magnetic field to undergo a global-separator bifurcation, where a stable separator is created. This can be seen in figure 4.22.

In fact stable separators play an important role during the evolution of the bright point. Structures resembling the three-source intersecting state can be seen at various times in the bright point. Examples of this are in figure 4.19 at 21:59, 22:43, 23:04, 03:42, 04:13 and 04:59.

This bifurcation behaviour local to the bright point is reflected in the changing loop structures and the shape of the bright point in the TRACE observations (figures 4.2 and 4.3).

This rapid local change in topology settles down at 06:21 when some of the structure persists for a while. Figure 4.23 highlights two key null points. The magnetic structure from these nulls persists for about two hours, even though locally there is some flux emergence and disappearance. Furthermore, the magnetic structure of the top null persists for longer (perhaps another five hours). This structure corresponds to the sigmoid phase of the bright point, so the local topological behaviour which corresponds to the sigmoid phase is fairly stable compared to the topological activity at the beginning of the bright point.

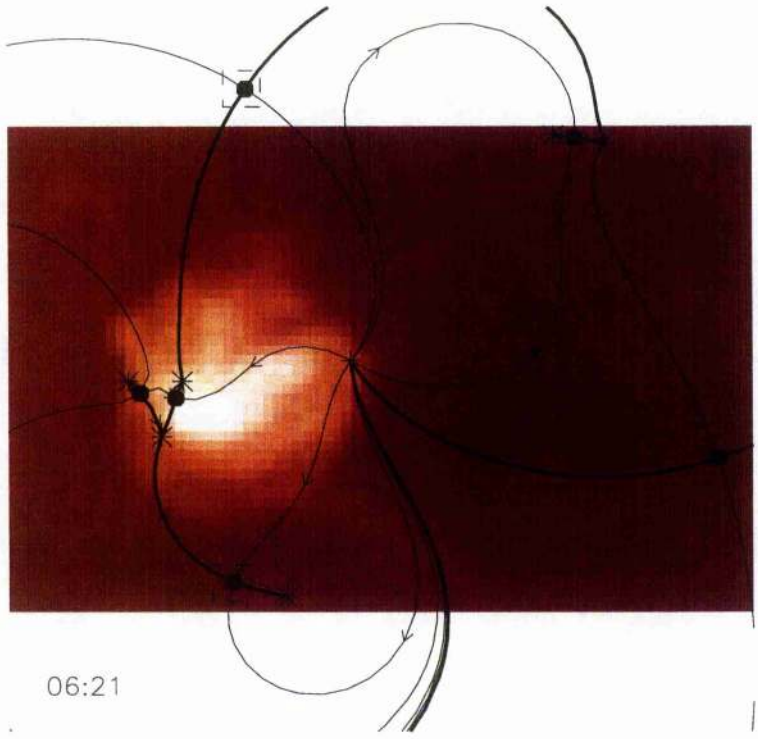

Figure 4.23: The topology at 06:21 has two null points, which are highlighted by the dashed boxes, whos structure persists for a many hours.

The twisting motion is caused by the rotation of the positive fragments indicated in figure 4.24. As the bright point twists and enters the π-phase, the topology to the right of the bright point changes significantly, while the topology to the left is largely unaffected. This is due to the approach of extra positive and negative fragments from the right, which probably cause the sigmoid structure to break and the π shape to form.

At 14:11 the null indicated in figure 4.25 at 12:49, 13:38 and 15:02 suddenly moves to the left. The problem with this frame is that one of the fragments (in the top left corner of figure 4.25 at 12:49, 13:38 and 15:02) has fallen below the threshold of being counted as significant and no longer has any influence on the model. The surrounding frames suggest that it may be more significant than previously assumed, and so other fragments may also be like this.

The final frame at 15:02 (figure 4.25) has a topology which is almost completely dif-

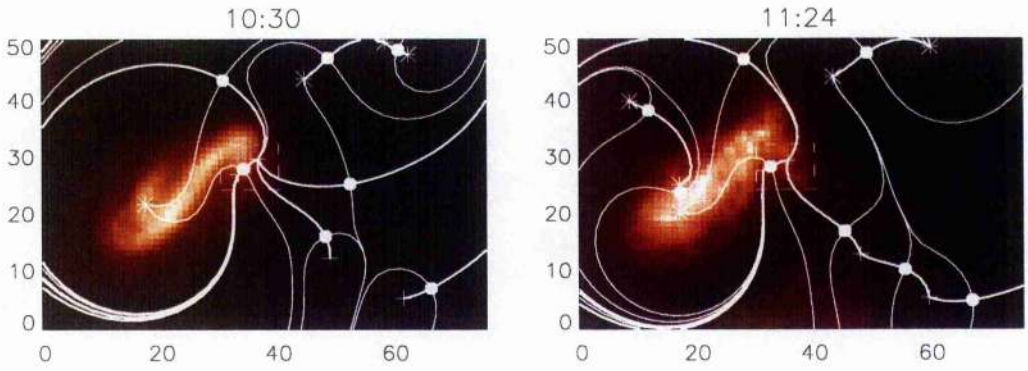

Figure 4.24: The topologies at 10:30 and 11:24. The dashed box indicates the two positive fragments (pluses) and the null points which rotate causing the twist of the bright point.

ferent to the previous frames. This is to be expected as the π phase has disappeared and only smaller fading loops remain, and so the topology will be very different. It is returning to a 'standard' quiet Sun magnetic field and losing a lot of its complexity.

4.9 Summary of Bright Points

Due to the high spatial and temporal resolution of TRACE, the structure and evolution of the coronal bright point can be seen in great detail. The bright point is obviously not a point, but bundles of loops that brighten and fade and gradually twist up over time and then completely reorder themselves. From the MDI data it is clear that the twisting is associated with shearing of the foot points and the π-configuration is due to reconnection between the original flux and a fairly small newly emerged flux region.

Magnetic field lines have been extrapolated using a constant-α force-free technique and matched with the loops in the TRACE observations. Comparison with the temperature and emission measure maps then provides temperature and emission measure profiles along the loops. A heuristic comparison with classical loop models shows consistency between the theory and the observations.

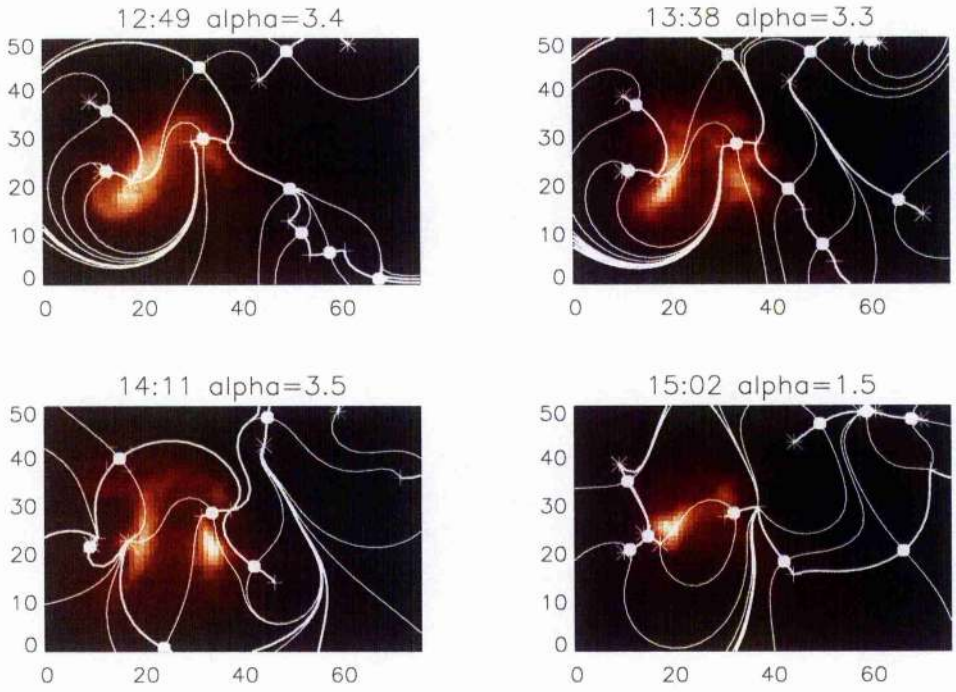

Figure 4.25: The topologies at 12:49, 13:38, 14:11 and 15:02. The dashed box in the first three images indicates a null point which moves as the bright point changes.

From the temperature and emission measure evolution plots, it is believed that the heating mechanism in the pre-sigmoid, sigmoid and π phases are the same since the temperature of the region does not vary markedly through its entire life. However, this does not mean that the bright point is heated continuously; the temperature plot is not a straight line and variations along it are considerably larger than can be explained by errors. Impulsive heating is therefore likely. The impulses are neither evenly spread nor of the same intensity. Indeed, from careful study of the Fe IX and Fe XII images, it is clear that different regions of the bright point brighten at different times.

Furthermore, the temperature remains fairly low during the lifetime of the bright point where the emission measure is much higher than its surroundings. This suggests that the bright loops are due to dense rather than hot plasma. The temperature and emission measure drop significantly before the bright point ends. This is due to the rapid

expansion of the bright point when it enters its π-phase.

Being able to identify and track individual magnetic fragments indicates which changes in the magnetic carpet cause the changes in the magnetic topology of the bright point. Specific changes have been identified as being important to the evolution of the bright point into the sigmoid and π phases and its final disappearance.

Separators occur during the first half of the life of the bright point. These regions are strong candidates for the area where field line reconnection can occur. This will be important for the early evolution of the bright point before the bright point enters its sigmoid phase. During the sigmoid phase, reconnection cannot play a big role as it would prevent twist from building up. When the π phase is entered and the bright point fades away, reconnection and bifurcation must play a role in dispersing the twist in the field.

Chapter 5

Summary and Future Work

5.1 Summary

This thesis has examined the three-dimensional topological behaviour exhibited by potential magnetic fields due to discrete flux sources in the photosphere. Particular attention was directed at the three-source and four-source cases.

In the three-source case (chapter 2), all of the possible stable topological states have been classified and the regions they occupy in parameter space has been deduced. The boundary between any two regions is a bifurcation line. On the bifurcation line an intermediate state between the two stable states, corresponding to the two regions, exists. This state is topologically unstable and small perturbations to the parameters of the magnetic field will push this state into one of the two stable states.

This bifurcation between two states can take a variety of forms, and four different types of three-dimensional bifurcation are described. These are the *local separator bifurcation*, the *global spine-fan bifurcation*, the *global separator bifurcation* and the *saddle-node-Hopf bifurcation*. The first three types of bifurcation are very general, and occur between many types of topological state from the three-source, four-source and higher-order cases. The saddle-node-Hopf bifurcation occurs along a bifurcation line between unstable states in the three-source case, one of which contains a null ring. It

is unclear if these states can be made stable in higher-order cases.

Analysis of the four-source case (chapter 3) is more specific in its focus due to the large number of parameters in the equation that describes the magnetic field. The behaviour of the separator, which previously occurred in the three-source case, has been studied in detail. Some topological states are introduced, and are subdivided into two categories, namely, composed states which describe topological states which are composed of elements of three-source states, and new states which exhibit behaviour not seen in the three-source case.

Topological behaviour is investigated by fixing the positions and strengths of three of the sources and perturbing the position of the fourth source. This is done for various strengths of the fourth source and bifurcation maps for subspaces of parameter space are found. From this, three types of bifurcation involving separators are described. These are the *global separator bifurcation*, the *local separator-coalescence bifurcation* and the *local double-separator bifurcation*. The first two bifurcations examine the ways in which two separators may interact and merge to form one separator (or, in the reverse case, how one separator can split into two separators). The local double-separator bifurcation is a variation of a pitchfork bifurcation and is instrumental in making null points lift off the $z = 0$ plane and into the upper half-plane.

Chapter 4 has looked at a sequence of observations of a coronal bright point made by the TRACE satellite and the MDI instrument on the SOHO satellite. The bright point behaviour has been subdivided into several phases and the behaviour of the magnetic fragments during each phase has been cataloged. Temporal variations in the area, temperature and emission measure of the bright point and the corresponding flux which is significant to the bright point have been analysed. This behaviour also corresponds to the different phases of the bright point, although the variation of flux fragments is the most important.

Spatial variations of temperature and density have also been calculated. From these, profiles along extrapolated field lines have been derived and analysed. The temperature does not vary a great deal due to the range which the TRACE filters can view. Emission

measure variations are more significant and are skewed towards the negative fragment.

The topology of the bright point has been extrapolated, using a constant-α force-free technique, at thirty different time-frames. Important topological features are highlighted and behaviour illustrated in the potential models (chapters 2 and 3) has been indicated.

5.2 Future Work

5.2.1 Magnetic Topology

This thesis has only just begun to explore the wealth of topological behaviour exhibited by source distributions. The four-source case has only been touched upon and higher order cases will become even more complex.

Most higher-order topologies can be constructed from the three- and four-source elements already encountered. However, there will still be new behaviour that requires study and new bifurcations to be deduced.

Hudson and Wheatland (1999) have suggested that force-free topology is qualitatively different to potential topology. Despite the flaw in their analysis (chapter 1.4), it is to be expected that new topological behaviour will be possible, in addition to the potential behaviour, due to the added complexity of twisting the field. If this is the case then the new behaviour must be identified and the degree to which it asserts itself on the magnetic field must be ascertained.

5.2.2 Bright Points

This work has not really deduced the way that the bright point is heated. Possible mechanisms are reconnection and topological change. This aspect will be investigated further.

Chapter 4 has only examined a single bright point. All that can be said from this is how this single object behaves. In order to formulate a comprehensive theory of how bright points behave in general, if indeed they have general behaviour, the study of more bright points must be undertaken.

This is particularly necessary to determine the mechanisms which lead to the formation of bright points. Chapter 4 indicates that the bright point studied here does not appear above either a converging magnetic feature or an ephemeral region, but instead appears above a bipole whose fragments are enhanced by other smaller fragments which merge with it. This suggests that the formation of bright points is more complex than has previously been thought. Further study would be needed to confirm and investigate this.

There are many more bright points in the existing TRACE and MDI data. Several can be seen in figure 4.1. Several of these bright points will be extracted and studied in order to understand the behaviour and properties of bright points. It may be possible to use TRACE and MDI to run another sequence of observations to study a set of bright points in a different period of time.

5.2.3 Polar Plumes

Polar plumes are an ideal phenomenon to be modelled by potential fields due to their slow evolution and minimal twist. Hood et al. (1999) have suggested that plumes brighten due to interaction between the positive fragments at their bases in the photosphere, and small negative fragments which pass close by.

A useful test for this would be to model the system using discrete sources, and vary the position of a small negative source to produce bifurcation diagrams like those in chapter 3. From this the level of bifurcation activity would be known and the appropriate topologies could be calculated. This would show the number of topological states that involve separators, as these would provide suitable reconnection sites to transfer the energy necessary to maintain the plume (Wang, 1998).

5.2.4 Reconnection

This thesis has paid particular attention to the separator (chapter 3). It is believed that the separator has particular importance to reconnection (Longcope and Cowley, 1996; Longcope, 1996; Birn et al., 1997). It would be instructive to use some of the field structures containing separators which were deduced in chapters 2 and 3 as initial conditions for three-dimensional numerical MHD experiments.

Appendix A

Analytical Constant-α Force-Free Fields

For the force-free approximation, assume that the magnetic field is the dominant force, and take $\nabla p = 0$ and $\rho \nabla \psi = 0$, so that equation 1.4 becomes

$$\mathbf{j} \times \mathbf{B} = 0. \tag{A.1}$$

This implies that

$$\mu_0 \mathbf{j} = \alpha \mathbf{B}, \tag{A.2}$$

which, when combined with equation 1.2, gives

$$\nabla \times \mathbf{B} = \alpha \mathbf{B} \tag{A.3}$$

Taking the divergence of both sides implies that

$$\nabla . (\alpha \mathbf{B}) = \mathbf{B} . \nabla \alpha = 0, \tag{A.4}$$

and so α is constant along fieldlines. In fact, equation A.4 is automatically fulfilled if $\alpha =$ constant.

So the problem is to solve the two equations

$$\nabla \times \mathbf{B} = \alpha \mathbf{B} \tag{A.5}$$

$$\nabla . \mathbf{B} = 0 \tag{A.6}$$

in the upper half-space $\{x, y, z | z \geq 0\}$, subject to the boundary conditions

$$\mathbf{B}_z(x, y, 0) = B_0(x, y) \tag{A.7}$$

$$\lim_{z \to \infty} \mathbf{B}(x, y, z) = 0 \tag{A.8}$$

where B_0 is the z-component of the magnetic field prescribed on the plane $z = 0$.

Now, the magnetic field can be written in the form

$$\mathbf{B} = \nabla \times \nabla \times (P\hat{\mathbf{z}}) + \alpha \nabla \times (T\hat{\mathbf{z}}), \tag{A.9}$$

which can be substituted into equation A.5 to give

$$\nabla \times (\nabla (\nabla . (P\hat{\mathbf{z}})) - \hat{\mathbf{z}} \Delta P) + \nabla \times \nabla \times (T\hat{\mathbf{z}}) = \alpha \nabla \times \nabla \times (P\hat{\mathbf{z}}) + \alpha \nabla \times (T\hat{\mathbf{z}}) \tag{A.10}$$

Rearranging gives

$$\nabla \times \nabla \times ((T - \alpha P)\hat{\mathbf{z}}) - \nabla \times ((\alpha T + \Delta P)\hat{\mathbf{z}}) = 0, \tag{A.11}$$

which is satisfied when

$$T - \alpha P = 0 \tag{A.12}$$

$$\alpha T + \Delta P = 0, \tag{A.13}$$

so that

$$\Delta P + \alpha^2 P = 0 \tag{A.14}$$

The most general solution to this equation, written in cylindrical polar co-ordinates, is

$$\begin{aligned} P(r, \theta, z) = \sum_{m=-\infty}^{\infty} e^{im\theta} \Bigg(& \int_{\alpha}^{\infty} A_m(k) \exp\left[-\left(k^2 - \alpha^2\right)^{1/2} z \right] dk \\ & + \int_{0}^{\alpha} B_m(k) \cos\left[\left(\alpha^2 - k^2\right)^{1/2} z \right] dk \\ & + \int_{0}^{\alpha} C_m(k) \sin\left[\left(\alpha^2 - k^2\right)^{1/2} z \right] dk \Bigg) J_m(kr), \end{aligned} \tag{A.15}$$

where $A_m(k)$, $B_m(k)$ and $C_m(k)$ are to be determined and J_m is the Bessel function of order m.

Now the magnetic field is prescribed by

$$\mathbf{B} = \nabla \times \nabla \times (P\hat{\mathbf{z}}) + \alpha \nabla \times (P\hat{\mathbf{z}}), \tag{A.16}$$

which gives the z-component of the magnetic field as

$$\mathbf{B}_z = -\frac{\partial^2 P}{\partial x^2} - \frac{\partial^2 P}{\partial y^2} = \frac{\partial^2 P}{\partial z^2} + \alpha^2 P. \tag{A.17}$$

This can be evaluated on the $z = 0$ plane to give

$$\mathbf{b}_z(r, \theta, 0) = \sum_{m=-\infty}^{\infty} \mathrm{e}^{im\theta} \left(\int_{\alpha}^{\infty} A_m(k) k^2 J_m(kr) dk + \int_0^{\alpha} B_m(k) k^2 J_m(kr) dk \right) \tag{A.18}$$

Note that, as the C_m terms disappear due to the evaluation of $\sin\left[(\alpha^2 - k^2)^{1/2} z\right]$ when $z = 0$, this boundary condition cannot be used to evaluate $C_m(k)$.

Now, to invert equation A.18, use the completeness relation for Bessel functions

$$\int_0^{\infty} x J_m(\lambda x) J_m(\lambda' x) dx = \frac{\delta(\lambda' - \lambda)}{\lambda'} \tag{A.19}$$

and for $\mathrm{e}^{im\theta}$

$$\int_0^{2\pi} \mathrm{e}^{im\theta} \mathrm{e}^{in\theta} d\theta = 2\pi \delta_{nm} \tag{A.20}$$

where $\delta(x)$ is the Dirac delta function.

Multiplying equation A.18 by $\mathrm{e}^{-in\theta} J_n(k'r)$ and integrating over r and θ gives

$$\int_0^{\infty} \int_0^{2\pi} \mathrm{e}^{-in\theta} J_n(k'r) \mathbf{B}_z(r, \theta, 0) r d\theta dr = 2\pi k' \left[A_n(k') H(k' - \alpha) + B_n(k') H(\alpha - k') \right], \tag{A.21}$$

where $H(x)$ is the step function. This separates to

$$A_m(k) = \frac{1}{2\pi k} = \int_0^{\infty} \int_0^{2\pi} \mathrm{e}^{-im\theta} J_m(kr) \mathbf{B}_z(r, \theta, 0) r d\theta dr \qquad \text{for } k > \alpha \tag{A.22}$$

$$B_m(k) = \frac{1}{2\pi k} = \int_0^{\infty} \int_0^{2\pi} \mathrm{e}^{-im\theta} J_m(kr) \mathbf{B}_z(r, \theta, 0) r d\theta dr \qquad \text{for } k < \alpha \tag{A.23}$$

Substituting equation A.22 and equation A.23 into equation A.15 and ignoring the term containing $C_m(k)$ gives

$$\begin{aligned} P(r,\theta,z) = \sum_{m=-\infty}^{\infty} \Bigg(& \int_{\alpha}^{\infty} \frac{1}{2\pi k} \int_0^{\infty} \int_0^{2\pi} r' \mathrm{e}^{im(\theta-\theta')} J_m(kr) J_m(kr') \\ & \times \exp\left[-\left(k^2-\alpha^2\right)^{1/2} z \right] \mathbf{B}_z(r',\theta',0) d\theta' dr' dk \\ & + \int_{\alpha}^{\infty} \frac{1}{2\pi k} \int_0^{\infty} \int_0^{2\pi} r' \mathrm{e}^{im(\theta-\theta')} J_m(kr) J_m(kr') \\ & \times \cos\left[\left(\alpha^2-k^2\right)^{1/2} z \right] \mathbf{B}_z(r',\theta',0) d\theta' dr' dk \Bigg) \end{aligned} \tag{A.24}$$

Now, by substituting the identity

$$\sum_{m=-\infty}^{\infty} \mathrm{e}^{im(\theta-\theta')} J_m(kr) J_m(kr') = J_0(kR), \tag{A.25}$$

where $R^2 = (x-x')^2 + (y-y')^2$, into equation A.24, the the structure of the $P(r,\theta,z)$ becomes

$$P(r,\theta,z) = \frac{1}{2\pi} \int_0^{\infty} \int_0^{2\pi} G_1(r,\theta,z,r',\theta') \mathbf{B}_z(r',\theta',0) r' d\theta' dr' \tag{A.26}$$

where

$$\begin{aligned} G_1(r,\theta,z,r',\theta') = & \int_{\alpha}^{\infty} \frac{1}{k} J_0(kR) \exp\left[-\left(k^2-\alpha^2\right)^{1/2} z \right] dk \\ & + \int_{\alpha}^{\infty} \frac{1}{k} J_0(kR) \cos\left[\left(\alpha^2-k^2\right)^{1/2} z \right] dk \end{aligned} \tag{A.27}$$

Equation A.16 gives the components of the magnetic field in terms of P, these are

$$\mathbf{B}_x = \frac{\partial^2 P}{\partial x \partial z} + \alpha \frac{\partial P}{\partial y} \tag{A.28}$$

$$\mathbf{B}_y = \frac{\partial^2 P}{\partial y \partial z} - \alpha \frac{\partial P}{\partial x} \tag{A.29}$$

$$\mathbf{B}_z = -\frac{\partial^2 P}{\partial x^2} - \frac{\partial^2 P}{\partial y^2} \quad = \quad \frac{\partial^2 P}{\partial z^2} + \alpha^2 P \tag{A.30}$$

Taking derivatives of P is equivalent of taking derivatives of G_1, so

$$\frac{\partial G_1}{\partial x} = \frac{x-x'}{R} \Gamma \tag{A.31}$$

$$\frac{\partial G_1}{\partial y} = \frac{y-y'}{R} \Gamma \tag{A.32}$$

where

$$\Gamma = -\int_{\alpha}^{\infty} J_1(kR)\exp\left[-\left(k^2-\alpha^2\right)^{1/2}z\right]dk \\ -\int_{\alpha}^{\infty} J_1(kR)\cos\left[\left(\alpha^2-k^2\right)^{1/2}z\right]dk. \quad \text{(A.33)}$$

This implies that the magnetic field can be written in the form

$$\mathbf{B}(x,y,z) = \frac{1}{2\pi}\int_{-\infty}^{\infty}\int_{-\infty}^{\infty}\mathbf{G}(x,y,z,x',y')\mathbf{B}_z(x',y',0)dx'dy' \quad \text{(A.34)}$$

with

$$G_x = \frac{x-x'}{R}\frac{\partial\Gamma}{\partial z} + \alpha\Gamma\frac{y-y'}{R} \quad \text{(A.35)}$$

$$G_y = \frac{y-y'}{R}\frac{\partial\Gamma}{\partial z} - \alpha\Gamma\frac{x-x'}{R} \quad \text{(A.36)}$$

$$G_z = -\frac{\partial\Gamma}{\partial R} - \frac{\Gamma}{R}. \quad \text{(A.37)}$$

Now Γ can be simplified by substituting the identity

$$\frac{1}{R}\frac{dJ_0}{dk}(kR) = -J_1(kR) \quad \text{(A.38)}$$

into equation A.33 and integrating by parts to obtain

$$\Gamma = \frac{1}{R}\left(-\cos(\alpha z) + z\int_{\alpha}^{\infty}\frac{k}{\left(k^2+\alpha^2\right)^{1/2}}\exp\left[-\left(k^2-\alpha^2\right)^{1/2}z\right]J_0(kR)dk \right. \\ \left. -z\int_{0}^{\alpha}\frac{k}{\left(k^2+\alpha^2\right)^{1/2}}\sin\left[\left(\alpha^2-k^2\right)^{1/2}z\right]J_0(kR)dk\right) \quad \text{(A.39)}$$

This can be evaluated using the identity

$$\frac{\cos(\alpha\rho)}{\rho} = \int_{\alpha}^{\infty}\frac{k}{\left(k^2+\alpha^2\right)^{1/2}}\exp\left[-\left(k^2-\alpha^2\right)^{1/2}z\right]J_0(kR)dk \\ -\int_{0}^{\alpha}\frac{k}{\left(k^2+\alpha^2\right)^{1/2}}\sin\left[\left(\alpha^2-k^2\right)^{1/2}z\right]J_0(kR)dk, \quad \text{(A.40)}$$

where $\rho^2 = R^2 + z^2$, to give

$$\Gamma = \frac{z\cos(\alpha\rho)}{R\rho} - \frac{\cos(\alpha z)}{R} \quad \text{(A.41)}$$

The trouble with this method is that it is an ill-posed problem, since an extra condition is required to fix the value of $C_m(k)$ in equation A.15. Unfortunately, there is no obvious candidate for such a condition. Prescribing the $\mathbf{B}_x(z = 0)$ and $\mathbf{B}_y(z = 0)$ components of the magnetic field over-specifies the problem. Chiu and Hilton (1977) suggest using the condition $\tan\psi(x, y, 0) = \mathbf{B}_y(x, y, 0)/\mathbf{B}_x(x, y, 0)$ to complete the solution, while Barbosa (1978) suggests imposing the condition $\mathbf{B}_z(z = L) = 0$ where L represents some plane above the $z = 0$ plane. These conditions are not particularly satisfactory since the $\mathbf{B}_x(z = 0)$ and $\mathbf{B}_y(z = 0)$ components of the magnetic field are not always available (such as magnetograms from MDI on SOHO for example), and the choice of height L of a second plane is arbitrary.

In general, the contribution from $C_m(k)$ is neglected, which is equivalent to setting $\partial\mathbf{B}_z/\partial z = 0$ on the $z = 0$ plane. It is this assumption that is made for this thesis.

Appendix B

Some Useful Quantities

This appendix details some typical values related to the Sun. These are split into three tables, general quantities of the Sun, different layers of the Sun and typical phenomena of the Sun.

The Sun			
Age		=	4.5×10^9 years
Mass	$M_\odot$	=	$1.99 \times 10^{30}\ kg$
Radius	$R_\odot$	=	$696\ Mm$
Surface gravity	$g_\odot$	=	$274\ m\ s^{-2}$
Luminosity	$L_\odot$	=	$3.86 \times 10^{26}\ W$
Equatorial rotation period		=	26 days
Polar rotation period		=	35 days
Mass loss rate		=	$10^9\ kg\ s^{-1}$
Speed of the fast solar wind		=	$800\ km\ s^{-1}$
Speed of the slow solar wind		=	$400\ km\ s^{-1}$
Surface distances	1 arcsec	=	$726\ km$
Distance from Earth	$1\ AU$	=	$1.5 \times 10^{11}\ m$
Permeability of free space	μ_0	=	$4\pi \times 10^{-7}$ henry m^{-1}

Layers of the Sun

Region	**Thickness** (m)	**Temperature** (K)	**Density** $(kg\ m^{-3})$
Core	1.7×10^8	$1.6 \times 10^7 - 8 \times 10^6$	$1.5 \times 10^5 - 2 \times 10^4$
Radiative zone	3.2×10^8	$8 \times 10^6 - 2 \times 10^6$	$2 \times 10^4 - 2 \times 10^2$
Convection zone	2×10^8	$2 \times 10^6 - 6400$	$2 \times 10^2 - 2.5 \times 10^{-4}$
Photosphere	5×10^5	$6400 - 4300$	$2.5 \times 10^{-4} - 4.3 \times 10^{-4}$
Chromosphere	2.5×10^6	$4300 - 3 \times 10^4$	$4.3 \times 10^{-4} - 1.4 \times 10^{-10}$
Transition Region	3×10^4	$3 \times 10^4 - 2 \times 10^6$	$1.4 \times 10^{-10} - 4 \times 10^{-12}$
Corona	–	$2 \times 10^6 - 9 \times 10^6$	$4 \times 10^{-12} - 2 \times 10^{-13}$

Typical Phenomena

Region	**Size** (m)	**Lifetime**	**Temperature** (K)
Granule	width $\sim 7 \times 10^5$ -1.5×10^6	$8 - 18$ mins	–
Supergranule	width $\sim 2 - 5.4 \times 10^7$	$1 - 2$ days	–
Sunspot	width $\sim 3 \times 10^7$	days - months	$2000 - 4000$
Spicule	height $\sim 9 - 11 \times 10^6$	$5 - 15$ days	$1 - 2 \times 10^4$
X-ray bright point	diameter $\sim 5 - 30 \times 10^6$	$2 - 48$ hours	$2 - 3 \times 10^6$
Active region	diameter $\sim 2 - 10 \times 10^8$	days - months	$2 - 4 \times 10^6$
Prominence	height $\sim 10^5$, length $\sim 10^7$, width $\sim 10^4$	minutes - hours	7000+

Appendix C

The MHD Equations

Several of the MHD equations are used in this thesis, the complete set is listed here.

Mass continuity equation,

$$\frac{\partial \rho}{\partial t} + \nabla.(\rho \mathbf{v}) = 0. \tag{C.1}$$

Momentum conservation,

$$\rho \frac{\partial \mathbf{v}}{\partial t} + \rho(\mathbf{v}.\nabla)\mathbf{v} = -\nabla p + \mathbf{j} \times \mathbf{B} + \rho \mathbf{g}. \tag{C.2}$$

The energy equation,

$$\frac{\rho^{\gamma}}{\gamma - 1} \frac{D}{Dt}\left(\frac{p}{\rho^{\gamma}}\right) = -L. \tag{C.3}$$

The gas law,

$$p = \frac{\rho \mathrm{R} T}{\tilde{\mu}}. \tag{C.4}$$

Ampere's law,

$$\nabla \times \mathbf{B} = \mu_0 \mathbf{j}. \tag{C.5}$$

Gauss' law,

$$\nabla.\mathbf{B} = 0. \tag{C.6}$$

Faraday's law,

$$\frac{\partial \mathbf{B}}{\partial t} = -\nabla \times \mathbf{E}. \tag{C.7}$$

Ohm's law,

$$\frac{1}{\sigma}\mathbf{j} = \mathbf{E} + \mathbf{v} \times \mathbf{B}. \tag{C.8}$$

Where,

$\mathbf{B}$ is the magnetic field,

$\mathbf{E}$ is the electric field,

$\mathbf{g}$ is the gravity field,

$\mathbf{j}$ is the current density,

$\mathbf{v}$ is the plasma velocity field,

T is the plasma temperature,

L is an energy loss function,

ρ is the plasma density,

p is the plasma pressure,

t is time,

$\mathrm{R} = 8.3 \times 10^3\ j\ K^{-1}\ kg^{-1}$ is the gas constant,

γ is the ratio of specific heats, c_p/c_v, and is often taken as $5/3$.

$\mu_0 = 4\pi \times 10^{-7}$ henry m^{-1} is the magnetic permeability of free space,

$\tilde{\mu} = 0.6$ for solar plasma ($\tilde{\mu} = 0.5$ for hydrogen plasma),

σ is the electrical conductivity.

Bibliography

Amari, T., Aly, J. J., Luciani, J. F., Boulmezaoud, T. Z., and Mikic, Z. (1997). Reconstructing the solar coronal magnetic field as a force-free magnetic field. *Solar Physics*, 174:129–149.

Antiochos, S. K. (1998). The magnetic topology of solar eruptions. *Astrophys. J.*, 502:L181–184.

Aulanier, G., Demoulin, P., Schmeider, B., Fang, C., and Tang, Y. (1998). Magnetohydrostatic model of a bald patch flare. *Solar Physics*, 183:369–388.

Barbosa, D. D. (1978). Linear force-free fields in the lower corona. *Solar Physics*, 56:55–66.

Berger, M. A. (1989). Three-dimensional reconnection from a global viewpoint. In Guyenne, T. and Hunt, J., editors, *Reconnection in Space Plasma. Potsdam 1988*, pages 83–86. ESA Paris.

Birn, J., Hesse, M., and Schindler, K. (1997). Theory of magnetic reconnection in three dimensions. *Advances in Space Research*, 19:1763–1771.

Brown, D. S., Parnell, C., Deluca, E., McMullen, R., and Golub, L. (1999). Observed magnetic structure of x-ray bright points from trace and mdi. In *PASP Conference Series*, volume 184, pages 81–85.

Brown, D. S. and Priest, E. R. (1998). The topology of coronal magnetic fields in active regions. In *PASP Conference Series*, volume 155, pages 90–94.

Brown, D. S. and Priest, E. R. (1999a). The topological behaviour of stable magnetic separators. *Solar Physics*.

Brown, D. S. and Priest, E. R. (1999b). Topological bifurcations in three-dimensional magnetic fields. *Proc. Roy. Soc.*, 455:3931–3951.

Browning, P. K., Lothian, R. M., and Clegg, J. R. (1998). Force-free models of relaxed and partially relaxed coronal magnetic fields. In *PASP Conference Series*, volume 155, pages 95–99.

Bungey, T. N. (1995). *Topological configurations of coronal magnetic fields and current sheets*. PhD thesis, University of St Andrews.

Bungey, T. N., Titov, V. S., and Priest, E. R. (1996). Basic topological elements of coronal magnetic fields. *Astronomy and Astrophysics*, 308:233–247.

Chiu, Y. T. and Hilton, H. H. (1977). Exact Green's function method of solar force-free magnetic-field computations with constant α. *Astrophys. J.*, 212:873–885.

Cowley, S. W. H. (1973). A qualitative study of the reconnection between the Earth's magnetic field and interplanetary field of arbitrary orientation. *Radio Science*, 8:903–913.

Feynman, R. P., Leighton, R. B., and Sands, M. (1977). *The Feynman lectures on physics*. Addison-Wesley.

Gary, G. A. (1989). Linear force-free magnetic fields for solar extrapolation and interpretation. *Astrophys. J. Supplement series*, 69:323–348.

Glendinning, P. (1994). *Stability, Instability and Chaos*. Cambridge University Press.

Golub, L., Krieger, A. S., Silk, J., Timothy, A., and Vaiana, G. S. (1974). Solar x-ray bright points. *Astrophys. J.*, 198:L93–97.

Golub, L., Krieger, A. S., and Vaiana, G. S. (1976a). Distribution of lifetimes for coronal soft x-ray bright points. *Solar Physics*, 49:79–90.

Golub, L., Krieger, A. S., and Vaiana, G. S. (1976b). Observation of spatial and temporal variations in x-ray bright point emergence patterns. *Solar Physics*, 50:311–327.

Gorbachev, V. S., Kel'ner, S. R., Somov, B. V., and Shverts, A. S. (1988). A new topological approach to the question of the trigger for solar flares. *Soviet Astronomy*, 32(3):308–314.

Gorbachev, V. S. and Somov, B. V. (1988). Photospheric vortex flows as a cause for two-ribbon flares: A topological model. *Solar Physics*, 117(1):77–88.

Grimmett, G. and Welsh, D. (1986). *Probability, an introduction*. Oxford Science Publications.

Guckenheimer, J. and Holmes, P. (1986). *Nonlinear Oscillations, Dynamical Systems and Bifurcations of Vector Fields*. Springer-Verlag.

Hide, R. (1979). On the magnetic flux linkage of an electronically conducting fluid. *Geophys. Astrophys. Fluid Dyn*, 12:171–176.

Hood, A. W., Priest, E. R., and Deforest, C. (1999). Coronal plumes. *in preparation*.

Hornig, G. and Schindler, K. (1996). Magnetic topology and the problem of its invariant definition. *Phys. Plasmas*, 3(3):781–791.

Hudson, T. S. and Wheatland, M. S. (1999). Topological differences between force-free field models. *Solar Physics*, 186:301–310.

Inverarity, G. W. and Priest, E. R. (1999). Magnetic null points due to multiple sources of solar photospheric flux. *Solar Physics*, 186:99–121.

Keller, H. B. (1976). Numerical solutions of bifurcation and nonlinear eigenvalue problems. In Rabinowitz, P. H., editor, *Applications of Bifurcation Theory*. Academic Press INC.

Klimchuck, J. A. and Gary, D. E. (1995). A comparison of active region temperatures and emission measures observed in soft x-rays and microwaves and implications for coronal heating. *Astrophys. J.*, 448:925–937.

Lau, Y. T. (1993). Magnetic nulls and topology in a class of solar flare models. *Solar Physics*, 148:301–324.

Lau, Y. T. and Finn, J. M. (1990). 3D kinematic reconnection in the presence of field nulls and closed field lines. *Astrophys. J.*, 350:672–691.

Lenz, D. D., DeLuca, E. E., Golub, L., Rosner, R., and Bookbinder, J. A. (1999). Temperature and emission measure profiles along long-lived solar coronal loops observed with TRACE. *Astrophys. J.*, 517:L155–158.

Longcope, D. W. (1996). Topology and current ribbons: a model for current reconnection and flaring in a complex evolving corona. *Solar Physics*, 169:91–121.

Longcope, D. W. and Cowley, S. C. (1996). Current sheet formation along three-dimensional magnetic separators. *Physics of Plasmas*, 3(8):2885–2897.

Lothian, R. M. and Browning, P. K. (1995). Coronal magnetic field equilibrium with discrete flux sources. *Solar Physics*, 161:289–316.

Moffatt, H. K. (1985). Magnetostatic equillibria and analogous Euler flows of arbitrarily complex topology. Part 1 fundamentals. *J. Fluid Mech.*, 159:359–378.

Molodenskii, M. M. and Syrovatskii, S. I. (1977). Magnetic fields of active regions and their zero points. *Soviet Astronomy*, 21(6):734–741.

Parnell, C. E. (1994). Modelling of dymanic coronal heating. In *Proc of the Third SOHO Workshop - Solar Dynamic Phenomena and Solar Wind Consequences*, pages 149–158. ESA SP-373.

Parnell, C. E., Priest, E. R., and Golub, L. (1994). The 3-dimensional structures of x-ray bright points. *Solar Physics*, 151:57–74.

Parnell, C. E., Smith, J. M., Neukirch, T., and Priest, E. R. (1996). The structure of three-dimensional magnetic neutral points. *Phys. Plasmas*, 3(3):759–770.

Priest, E., Bungey, T. N., and Titov, V. S. (1997). The 3d topology and interaction of complex magnetic flux systems. *Geophysics, Astrophysics, Fluid Dynamics*, 84:127–163.

Priest, E. R. (1982). *Solar Magneto-hydrodynamics*. D. Reidel pub. co.

Priest, E. R., Parnell, C. E., and Martin, S. F. (1994). A converging flux model of an x-ray bright point and an associated cancelling magnetic feature. *Astrophys. J.*, 427:459–474.

Priest, E. R. and Titov, V. S. (1996). Magnetic reconnection at 3D null points. *Phil. Trans. Roy Soc*, 354:2951–2992.

Rheinboldt, W. C. (1986). *Numerical Analysis of Parametrised Nonlinear Equations*. John Wiley and Sons.

Rosner, R., Tucker, W. H., and Vaiana, G. S. (1978). Dynamics of the quiescent solar corona. *Astrophys. J.*, 220:643–665.

Ruelle, D. (1989). *Elements of Differentiable Dynamics and Bifurcation Theory*. Academic Press INC.

Sakurai, T. (1989). Computational modelling of magnetic fields in solar active regions. *Space Science Reviews*, 51:11–48.

Schrijver, C. J., Title, A. M., Hagenaar, H. J., and Shine, R. A. (1997). Modelling the distribution of magnetic fluxes in field concentrations in a solar active region. *Solar Physics*, 175:329–340.

Serio, S., Peres, G., Vaiana, G. S., Golub, L., and Rosner, R. (1981). Closed coronal structures. II. Generalized hydrostatic model. *Astrophys. J.*, 243:288–300.

Smith, J. M. (1997). *Ducted magnetoacoustic waves in the solar corona*. PhD thesis, University of St Andrews.

Thompson, J. M. T. and Stewart, H. B. (1986). *Nonlinear Dynamics and Chaos.* John Wiley and Sons.

Titov, V. S., Priest, E. R., and Demoulin, P. (1993). Conditions for the appearance of 'bald patches' at the solar surface. *Astron. Astrophys.*, 276:564–570.

Topping, J. (1962). *Errors of observation and their treatment.* Science Paperbacks.

Vaiana, G. S., Krieger, A. S., Speybroeck, L. P., and Zehnpfennig, T. (1970). The structure of the X-reay corona and its relation to photospheric and chromospheric features. *Bul. Am. Phys. Soc.*, 15:611.

Wang, Y. M. (1998). Network activity and the evaporative formation of polar plumes. *Astrophys. J.*, 501:L145–150.

Wentzel, D. G. (1989). *The restless Sun.* Smithsonian Institution Press.